TRAFFICKING AND EFFICACY OF CATIONIC POLYMERS AS DNA VACCINE CARRIERS AND ANTI-CANCER AGENTS

A DISSERTATION SUBMITTED TO THE FACULTY OF THE GRADUATE SCHOOL OF THE UNIVERSITY OF MINNESOTA

BY

David A. Panus

IN PARTIAL FULFILLMENT OF THE REQUIREMENTS FOR THE DEGREE OF DOCTOR OF PHILOSOPHY

Advisor: **Chun Wang, Ph.D.**

June 2013

Acknowledgements

This work was funded by the National Institutes of Health (grant number R01CA129189) as well as NIH Biotechnology Grant (T32 HM008347), and the Medtronic first-year Biomedical Engineering Department fellowship. I would first like to thank Dr. Chun Wang for all of his attention, support, and understanding, as well as giving me the opportunity to work in his lab. I would also like to give special thanks to Dr. Wei Shen, Dr. Ron Siegel, and Dr. Jonathan Sachs for their guidance and participation on my thesis committee.

I would also like to thank the University Imaging Center (UIC), especially John Oja for assistance and training in confocal microscopy and live animal imaging and quantification. Karen Grinn (Ohlfest/Reineke Lab) for assistance with *in-vivo* mouse study design. A very special thanks to all of my fellow lab mates both present and graduated, especially Weihang Ji, for his undivided attention when I asked random questions regarding polymer chemistry or experimental assay design. I would also like to thank Xiao Zhong for assisting me with experiments. A very special thank you to Wenqing Han, for being a second mother to James when I had to finish something in the lab, and help with *in-vivo* tumor model histology.

A very special thank you to my parents Maria, Arlo, and Mary Helen, as well as my brothers (Ed, Mike, Brian, Aric) and sisters (Brenda, Jenny, Amy, and Ramona) for supporting me through this journey. Finally, I would like to thank my wife, Sarah. You are my everything, and love is too small of a word to truly describe my feelings for you. To each and everyone – I thank you.

Dedication

"Around here, however, we don't look backwards for very long. We keep moving forward, opening up new doors and doing new things… and curiosity keeps leading us down new paths."

- Walt Disney

This thesis is dedicated to two men that have bookended my life, my father and my son. They have taught me to love, to live, and to look at life as if it was governed by the rules of magic.

Abstract

The potential of DNA vaccines for treatment of diseases such as HIV and cancer are overwhelming, due to the fact that DNA vaccines can activate both a cell-mediated (T-cell) and humoral (antibody) immune response. However, the most commonly occurring problem of DNA vaccines is limited transgene delivery and expression. Currently, much effort has focused on designing an optimal polymer system that is stable, can protect and deliver DNA, as well as offer high transgene expression. Unfortunately, the ability of polymer based systems to produce robust gene expression, have yet to show substantial improvement. The major obstacle hindering successful transgene expression can be attributed to the interactions of the polymer-DNA complex with the subcellular environment. Therefore, we focused on understanding the structure-functional relationship of a well-defined simple polymer based system and how they might lead to improved transgene expression. First, we investigated the effect of polymer molecular weight and backbone structure on transgene expression as it pertains to subcellular trafficking. Second, we focused on the relationship between polymer-DNA complexes and different dendritic cell-types as a function of maturation state. Lastly, we looked into how further modification of a cationic polymer can lead to elevated cytotoxicity and use as an anti-cancer agent. The results from this work can be used as a design template to improve the overall subcellular trafficking and efficacy of cationic polymer based DNA vaccines or anti-cancer agents.

Table of Contents

List of Figures

List of Tables

Chapter 1: Introduction

The advancements of science and technology have influenced the growth of modern medicine in our ability to diagnosis and treat illness. The discovery of vaccines has lead to the control, and in some cases, the elimination of diseases such as tuberculosis, hepatitis B, and meningitis among others[1]. However, despite these advancements, cancer and HIV/AIDS related deaths are still prominent worldwide[1].

1.1. Traditional Vaccines

Though traditional protein-based vaccines have been shown in the past to produce robust immunity against microbes and prevent infectious disease[2], they offer limited impact when dealing with diseases, such as cancer, which can alter their genome[3]. This is most likely due to the fact that traditional vaccines are only adequate at activating an incomplete immune response, as they are focused only on activation of the humoral or antibody branch of the immune system[4]. More importantly, the treatment of cancer or other viral based infections can only be cleared with a T-cell or cell-mediated immune response[5]. However, only live attenuated viruses and bacteria are able to produce a cell-mediated immune response, yet they may be dangerous to administer into patients with compromised immune systems[3,6]. Moreover, current vaccine technologies offer limited efficiency profiles, and they require multiple booster injections to maintain an effective antibody level[6].

1.2. DNA Vaccines

The main goal of a DNA vaccine is different than that of a traditional vaccine in that active DNA vaccines offer a therapeutic, as well as, a prophylactic approach by inducing an activation of immune effector pathways and immunological memory to prevent any recurrence of the disease[5]. Development of DNA vaccines has focused on activation of specific antigen presenting cells, which are able to induce an immune response upon presentation of a foreign antigen. It is well known that both a humoral and cell-mediated immune response can be induced following the administration of exogenous antigens[7] to antigen presenting cells, and induce tumor specific immunity and regression in cancer patients[8]. A number of different exogenous antigens strategies have been used in the past, such as: peptides, proteins, naked DNA and RNA plasmid, tumor antigens, and whole tumor cells[9]. DNA-based vaccines offer the most robust platform to activate an immune response since the target antigen is comprised of a protein, which is encoded within the DNA plasmid simulating a live infection. The degree of immune activation can be further enhanced with the use of adjuvants in conjugation with DNA vaccines. Adjuvants can improve an immune response in a number of ways: by increased cell recruitment, enhance DNA delivery, and improved the DNA expression[10]. DNA-based vaccines also offer a host of advantages including: the ability to simply modify the vaccine targeting by modification of the DNA sequencing and it offers cheap and rapid production[3].

1.3. Dendritic Cell Activation

Dendritic cells (DCs) are a subtype of antigen-presenting cells (APCs), which are viewed to many as the initiator and modulator of the immune system[11,12,18,25]. DCs are

the most potent APC and are unique in their capacity to initiate a primary T-cell immune response[13]. DCs are important in launching humoral immunity through their capacity to activate naïve and memory B-cells, and activate natural killer cells and natural killer T-cells[9,14,15]. DCs have the specific function of capturing, processing, and presenting antigens to B-cells and T-cells[16]. Immature DCs are present in peripheral tissues such as skin and mucous membranes, while in this state; DCs are unable to activate T-cells[17]. During their immature state, DCs are poised to capture antigens[14,15,18] in one of three ways: phagocytosis, macropinocytosis, or receptor-mediated uptake, such as Fc receptors, mannose receptor, or DC-SIGN[19,20]. DCs exhibit two mechanisms of stimulation: direct-presentation and cross-presentation. Direct presentation and cross-presentation routes have similar mechanisms for recognizing viral infection; however, during direct presentation, an immature DC is stimulated by direct binding of a virus to special receptors found on the DC surface known as Toll-Like receptors (TLR), which allow them to recognize microbial ligands[5,20-22]. The DCs then bind peptides derived from viral pathogens to their major histocompatibility complex (MHC) and present the complex on its surface. This causes the DC to temporarily increase their rate of antigen uptake[23,24]. The full antigen potential of DC is only apparent after receipt of maturation signals, which direct migration of DCs from the peripheral tissue to the draining lymph nodes where T-cells reside[14,15,20,23]. When DCs reach the lymph system, T-cells (CD4+ and CD8+) recognize the antigen-activated MHC complexes on the DCs surface by means of T-cell antigen receptor (TCRs)[15,20,24]. DCs present the peptides to naïve T-cells, thereby inducing a cellular immune response that involves both $CD4^+$ T helper 1 (T_H1) cells and cytolytic $CD8^+$ T cells[11,23,25]. Maturation of DCs causes an up-regulation of MHC I and

II, CD80, CD86, and CD40 as well as CD83, p55 and LAMP. DCs also increase production of cytokines IL-12, IL-15, and IL-18, which are needed for stimulation of CD4+ T-cells[19,20]. MHC class I response primes for a cytotoxic T-lymphocyte (CTL) mediated immune response and CD8+ T-cell activation. CD8+ T-cell activation is of extreme importance targeting and killing tumor cells[5]. A MHC class II response leads to an enhanced antibody production (induction of humoral response) and CD4+ T-cell activation[13]. DCs also induce either Th1, Th2, or regulatory immune response depending on their state of maturation and activation[25] (Figure 1.1). The Th1 response is responsible for clearance of viruses and some strains of bacteria, while the Th2 response induces antibodies to neutralize toxins, viruses and bacterial adhesion[20]. The cross-presentation stimulation of DCs is similar to that of direct presentation. During cross presentation, DCs are not stimulated by "direct" interaction with a virus (direct presentation); rather, they are stimulated by the exogenous viral protein released by an infected cell[22]. The exogenous proteins are then presented on the MHC-I or MHC-II complex[13]. Once stimulated, cross-presentation follows the same DC maturation cascade as direct presentation.

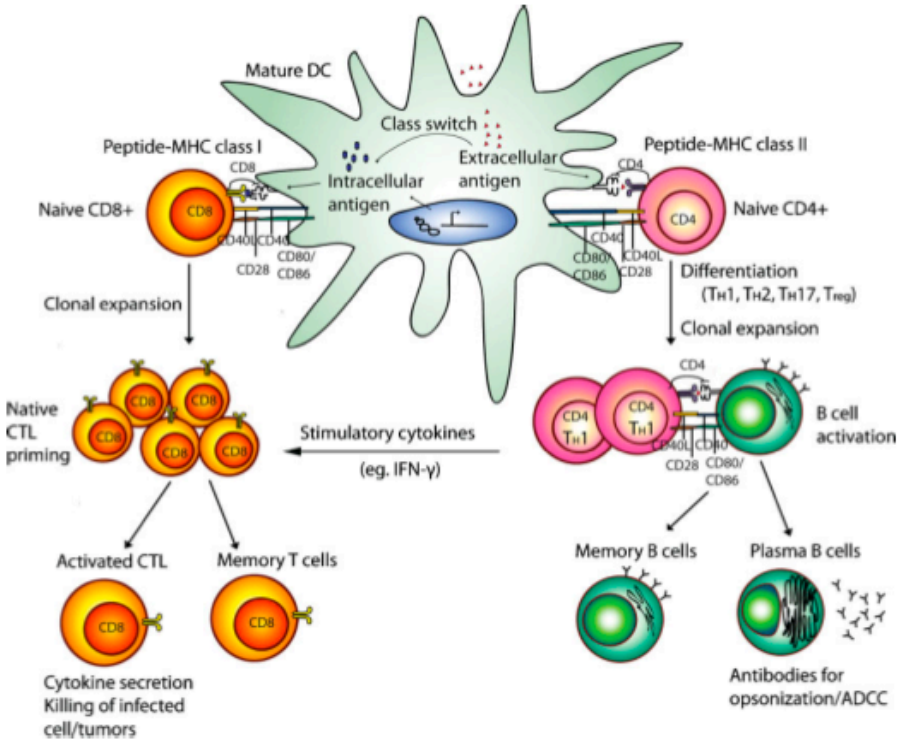

Figure 1.1. Immune system activation by dendritic cells. Simplified presentation of activated dendritic cell stimulating both the humoral and cell mediated immune responses. The dendritic cell is activating the CD8+ T-cell after transfection with an intracellular antigen; likewise an extracellular antigen is responsible for the activation of the CD4+ T-cell and in turn activation of B-cells. After activation of the T-cells, the CD8+ expands into activated cytotoxic T-cells (CTL) and memory T-cells. Activation of CD4+ leads to activation and expansion of memory and plasma B-cells. Figure copied from Nguyen et. al[3]. Figure reprinted with permission from John Wiley and Sons: [Advanced Materials] (v. **20**, p. 1), copyright (2008).

1.4. Viral Vectors for Gene Delivery and DNA Vaccines

It is now well known that both a humoral and cell-mediated immune response in CD4+ and CD8+ T-cells can be induced following the administration of plasmid DNA[26,27], as well as induce tumor-specific immunity and regression in cancer patients[8]. However, the use of naked plasmid DNA alone has limited delivery efficiency, which in turn limits the overall therapeutic effectiveness[8,28]. This deficiency is mostly a result of the plasmid DNA being easily degraded by DNAse enzymes *in-vivo* within minutes[29], making it prone to tissue clearance[30]. Also, cellular uptake confers the internalized DNA into closed vesicles (endosomes, lysosomes or phagosomes), where the pH is

progressively lowered to 5.0-6.5, denaturing the DNA[24]. In order to increase the effectiveness of DNA-based therapeutics, the plasmid DNA must be protected from degradation[31].

Viruses make an ideal candidate as nucleic acid vectors since they have evolved mechanisms, which allow them to avoid lysosomal trafficking by promoting the fusion of the viral envelope with the endosomal membrane, thus causing the release of the DNA into the cells cytoplasm[32]. Some of the most widely used viral vectors are: adeno-associated virus (AAV), adenovirus, alpha viruses, herpes simplex virus, lentivirus, and retrovirus. However, with all the benefits of viral vectors a number of limitations also exist such as: high immunogenicity, limited size of inserted DNA, and high potential of the virus reverting back to its wild-type phenotype[27,29]. Viruses' immunogenicity makes it difficult for repeat treatments and can cause a dangerous immune response in patients with compromised immune systems[29].

1.5. Non-viral Vectors for Gene Delivery and DNA Vaccines

The limitations of viral vectors have led to the development of non-viral vectors such as biodegradable and cationic polymers. Biodegradable polymers have been used for medical applications for over 40 years, most notability for sutures. However, the use of biodegradable polymers for use as nucleic acid delivery systems is still in its infancy. Yet, biodegradable vectors have a number of advantages, specifically in DNA-binding mechanisms and degradation rate. Biodegradable polymers form a protective shell around the nucleic acid, inhibiting plasmid degradation by enzymes or nucleases, and the degradation rate can be modified to target specific release rates[3,33]. One of the most

commonly used and researched biodegradable polymers is poly(DL-lactide-co-glyocide). Poly(DL-lactide-co-glycolide) also known as PLGA is a biocompatible and biodegradable polymer, documented as having excellent tissue compatibility, biodegradability, and safety profile in humans[34]. These characteristics have led to a number of products using PLGA, to be approved by the U.S. Food and Drug Administration[3]. However, PLGA is not an ideal material for use in drug delivery applications for a number of reasons. The first, is that the degradation of PLGA occurs by random hydrolysis or enzyme-catalyzed degradation of the ester bonds in the polymer backbone, producing lactic and glycolic acid[35,36]. In excess quantities these lactic and glycolic acid byproducts can produce highly acidic environments, with pH levels ranging from 1.5 to 6.4 within the PLGA microsphere[37]. A prolonged exposure to this acid environment can potentially cause damage or denaturing of the DNA plasmid cargo[33,38]. Another hindrance of PLGA is that the hydrophilic nature of PLGA makes entrapment of DNA difficult, by allowing diffusion of water into the polymer/DNA particle, causing the polymer to degrade from the inside out resulting in a premature burst of DNA[39,40,41]. Lastly, the overall degradation of PLGA is slow, ranging from days to weeks to months depending on the polymer's molecular weight. This slow degradation does not allow for delivery and expression of DNA encoding antigen within the life span of dendritic cells *in-vivo*[23,41]. A number of techniques have been designed to increase the efficacy of DNA-PLGA encapsulation and have been readily reviewed[43,44]. One of the most commonly used techniques is the double emulsion process. Double emulsion is a simple method of encapsulating DNA in hydrophilic molecules, by using a water-in-oil or solid-in-oil suspension. However, this process typically transforms supercoiled DNA to a

nicked or linear state, and only yields a 20% entrapment of DNA in PLGA[45]. The damaging effects of microparticle entrapment on DNA have led to alternate methods of plasmid DNA delivery.

Cationic polymers are another class of non-viral polymers, which carry a positive charge found on primary, secondary, tertiary, or quaternary amino groups, allowing cationic polymers to interact with the negatively charged phosphate group located in the DNA backbone[46]. Poly(L-lysine) (PLL) was one of the first and most popular non-viral cationic material used for nucleic acid delivery[47], since PLL efficiently condenses DNA, and protects it from hydrolytic enzymes and nucleases[48,49]. PLL also offers the advantages of high transfection levels *in-vitro* and biodegradablility[46]. However, PLL has produced poor results *in-vivo*, showing high levels of cytotoxicity at high molecular weights (25 kDa) and low transfection efficiency due to its inability to facilitate endosomal escape[3,49,50]. The use of endosomolytic agents like chloroquine in conjugation with PLL has been shown to improve the endosomal escape capability of PLL by neutralizing high endosomal pH levels; however, the cytotoxicity of chloroquine limits its ability to be used in-vivo.

Behr et al. first presented polyethyleneimine (PEI) as a means of drug delivery in 1995, primarily for its ability to induce high levels of gene transfer, through high stability and endosomal escape[51,52]. PEI structure is made up of branched polycations containing primary, secondary, and tertiary amines in a 1:2:1 ratio[52]. The high transfection of PEI is believed to be a result of the "proton-sponge" characteristic, which allows it to withstand highly acidic environments such as those found in endosomes and lysosomes[53]. The "proton sponge" is believed to occur because every third atom in the PEI structure is an

amino nitrogen, which enables PEI to be easily protonated and draw water into the acidic vesicle until it bursts[51]. PEI high transfection is seen at high molecular weight (25kDa), however, at this molecular weight, PEI has intolerable cytotoxicity and limited uses in clinical applications due to its non-biodegradability[53,54]. PEI high transfection, cytotoxicity, and poor biodegradation at high molecular weights lead to the modification of PEI by lowering PEI molecular weight[53]. Modification also led to an increase in the degradation rate of high molecular weight PEI[55-58], in order to decrease cytotoxicity while maintaining high transfection rate.

Poly(β-amino ester) (PBAE) are synthetic, biodegradable, cationic polymers, which are attractive as co-polymers and polymer end-groups since they offer the addition of pH-sensitivity, the ability to condense DNA, promote endosomal escape, and offer low cytotoxicity[59]. PBAE are synthesized by Michael addition of primary and secondary diamines with diacrylate-diols[60-63]. The ease of synthesis and large numbers of commercially available amines and diacrylates allows for synthesis of a large number of PBAE polymers[63]. PBAE are highly efficient *in-vitro* and the properties of PBAE can be custom tailored for specific application by modification or addition of different types of diamines or diols[3,60]. Lynn et al. constructed a library of 140 structurally unique PBAE in bulk, with only 6 diacrylate and 20 amine monomers. A large portion of these polymers (55%) had molecular weights ranging from 2000-50000 as determined by GPC. Half of the polymers were water-soluble, and were analyzed in a DNA-binding assay. Of the 70 polymers tested, 56 had significant DNA-binding interactions. The PBAE library created by Lynn et al. were only a small number of possible PBAE polymers. Anderson et al. later synthesized and characterized a secondary library of 486 PBAE polymers,

producing polymer C32 which is the most effective PBAE discovered to date. C32 has shown markedly higher transfection efficiency than that of PEI and Lipofectamine 2000. Anderson et al. improved C32 by modifying the polymer end groups by a two-step reaction, while end-capping of the PBAE was carried out by a Michael addition. DNA delivery efficiency measured by a high throughput assay showed that acrylate and amine terminated polymers caused a vast increase in transfection compared to unmodified C32. Polymers capped with hydrophilic amines showed the highest transfection overall. Cytotoxicity was measured at a polymer/DNA ratio of 100:1; these results showed high cell viability for the majority of end-modified C32 polymer (22 of 35 polymers), compared to PEI (3%) and unmodified C32 (90%) in COS-7 cells. DNA uptake measured by use of β-gal and RT-PCR, showed that amine-modified end chain polymers had higher DNA uptake compared to naked pDNA.

Non-viral vectors offer a number of advantages over viral vectors such as: high stability, low immunogenicity, low toxicity, and larger cargo capacity[65,66]. However, non-viral vectors are still less efficient than their viral counterpart[65,67,68], and current designs have yet to adequately induce substantial gene expression[67], primarily due to non-viral vectors inability to overcome specific subcellular barriers[29].

1.6. Extracellular and Subcellular Barriers

Successful cellular navigation is a critical hurdle that needs to be addressed to produce clinically relevant DNA vaccines. For this to occur *in-vitro,* the polymer vector needs to successfully complex the plasmid DNA, target a specific cell type surface, gain entrance into the cell, escape the endosome, and deliver the DNA to the nucleus, all while

protecting the DNA from degradation[3,29,69] (Figure 1.2). The difficulties of this process only increase when applied *in-vivo* with the addition of transport through the blood stream, blood vessel walls, and cell targeting[3]. The first step of the intracellular process involves binding the polyplex to the target cell surface by means of ionic interactions between the positively charged polymer vector and the negatively charged cell surface[50,69,70]. The binding of the polyplex to the cell surface initiates internalization of the polyplex into the cell by endocytosis.

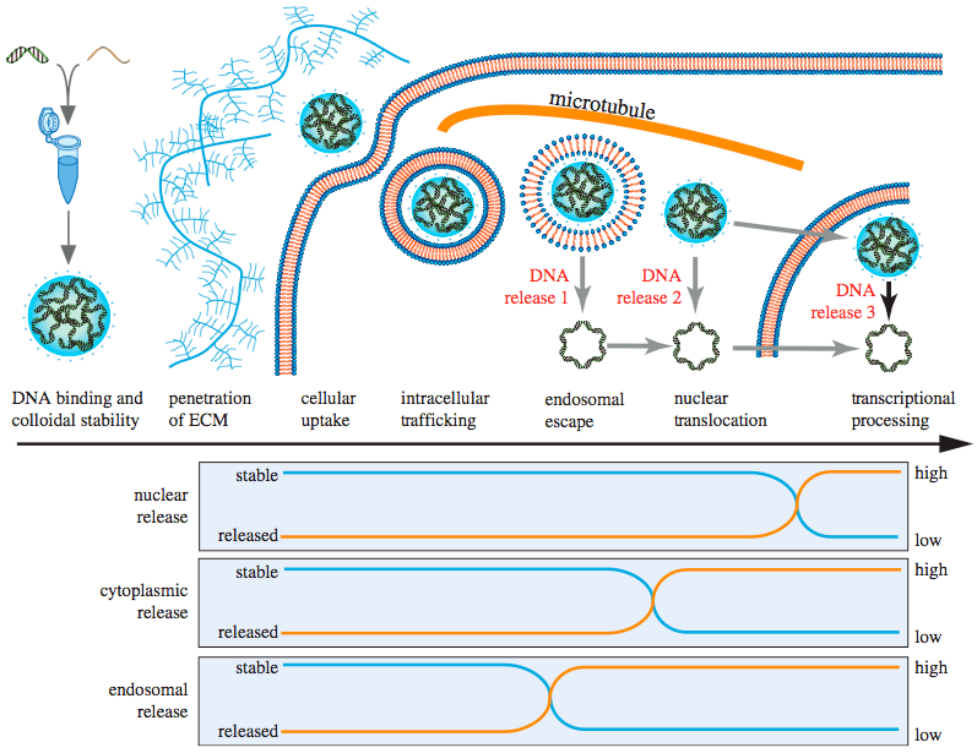

Figure 1.2. Representation of the different subcellular barriers needed to overcome by polymeric delivery systems for successful transfection efficiency. First, the DNA and polymer vector must bind DNA into a stable complex. The complex must then overcome the negatively charged extracellular matrix (ECM) and be taken up into the cell. Next, the complex must escape the endosome and traffic into the cell nucleus where the DNA must be released for transcription to occur. Figure copied from Grigsby et. al[71]. Figure reprinted with permission from Highwire Press: [Journal of the Royal Society Interface] (v. **7**, p. S67), copyright (2010).

The internalization of polyplexes into the cell is not a straightforward process since there are different modes of endocytosis including: clathrin-mediated pathway, caveolae-mediated pathway, pinocytosis, phagocytosis, and receptor-mediated endocytosis[70] (Figure 1.3). The pathway in which polyplexes are internalized is dependent on a number of particle characteristics such as: polyplex size, shape, hydrophobicity, and the manner of polyplex binding to the cell surface[70,72]. The most prominent endocytotic pathway accessed by polyplexes is the clathrin-mediated pathway (CMP), which internalizes particles with diameters in the range of approximately 100 to 150 nm, by surrounding the polyplex with the plasma membrane thus engulfing the polyplex[73]. The plasma membrane then pinches off forming a vesicle within the cytoplasm. These vesicles are then trafficked into the cytoplasm where they fuse with late endosomes or lysosomes[70,74]. Fusion with these organelles results in an acidic environment within the endosome, which can damage or degrade the polyplex[29,70]. Material trapped within the endosome is denied access to the cytoplasm and nucleus, and can either be degraded or removed from the cytoplasm by exocytosis[70]. A second internalization process known as caveolae-mediated endocytosis (CME) has also been identified, which readily take up particles that are between 50 to 60 nm and as large as 500nm in diameter[75]. The CME process is believed to be the ideal pathway to transfect cells since this pathway bypasses interactions with endosomes and lysosomes[74]. However, the size and quantity of caveolae located on the cell surface are dependent on the cell type, which limits its potential applications[76]. The remaining endocytosis pathways involve the uptake of particles that are extremely large in diameter (0.5 to 5μm)[76]. After endosomal escape the polyplexes migrate to the nucleus periphery through

the cytoplasm by a process, which is mediated by the microtubule network, this process is by no means a rate-limiting process, however, nuclear uptake can be[73].

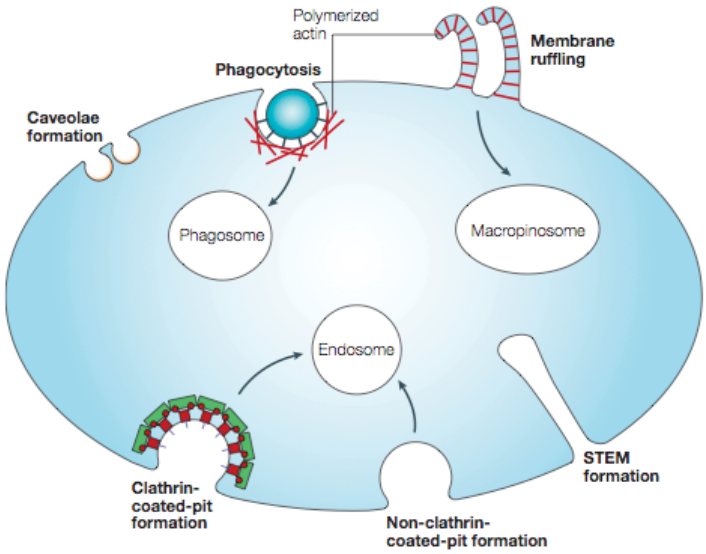

Figure 1.3. Cartoon of the multiple endocytotic routing pathways found on the surface of cells. Figure copied from Maxfield et. al[77]. Figure reprinted with permission from Nature Publishing Group: [Nature Reviews Molecular Cell Biology] (v. **5**, p. 21), copyright (2004).

The entry of polyplexes or DNA into the nucleus can pose a huge barrier to gene expression[73]. Gao and co-workers demonstrated that low gene expression was a result of low DNA uptake by injecting polyplexes directly into the cytoplasm. This suggests nuclear uptake can be a rate-limiting step, because transport of exogenous material into the nucleus must be facilitated by passive or active transport. Molecules which are smaller than 9 nm can passively transport across the nuclear pore complex (NPC) located in the nuclear envelope, yet molecules larger than this must be actively transported across the nuclear envelope[70,73]. Most DNA plasmids used to form polyplexes are much larger than the NPC, thus limiting passive transport into the nucleus. A potential way around this barrier is through timing of mitosis, which results in the temporary degradation of the nuclear envelope. Tseng et al. showed that cells going through the beginning phases of

mitosis displayed an elevated level of gene expression. A second process, which can be used to facilitate nuclear uptake is through the use of the nuclear localization signal (NLS), which are short cationic peptide sequences that are recognized by importins[29]. The NLS has the ability to usher in DNA by active transport across the nuclear envelope. A number of studies have shown that incorporation of a viral NLS can improve nuclear uptake[78-80]; however, this technique is limited based on toxicity and immunogenicity[50]. Despite these attempts, nuclear import of polyplex vectors is still one of the most poorly characterized steps in the gene-delivery process[29].

1.7. Subcellular Imaging *In-vitro*

Visualization of the subcellular trafficking mechanisms *in-vitro* is a pivotal first step necessary to produce high levels of gene expression *in-vivo*. A number of techniques can be used for imaging the subcellular trafficking of polyplexes, but the most commonly used method is confocal microscopy. By labeling specific components of the polyplex, such as the polymer or DNA, as well as cellular organelles with fluorescent fluorochromes, one can monitor the movement of the polyplex through the cell over time. Godbey et al. were among the first to observe the subcellular trafficking of high molecular weight PEI and PLL in E.A.hy 926 cells, by labeling the polymers with an Oregon Green 488 fluorescent tag. From this work, Godbey was able to visualize the polyplexes attachment to the cell surfaces and cellular uptake over a course of time. They revealed that PEI exhibited nuclear localization where PLL had limited to no nuclear localization. Godbey and co-workers also monitored lysosomal interaction by fluorescently labeling the lyosome with Lysotracker Red (Invitrogen, Eugene, O.R.)[81,82].

Since this method was first used, a number of methods have used confocal microscopy to visualize subcellular trafficking[83-89]. Despite visual conformation of trafficking, a major drawback to confocal microscopy is the inability to quantify the colocalization of polyplex within organelles, polyplex dissociation or cellular uptake. Recently, a method of quantification was developed by Akita et. al., which measured the total pixel area of specific components within the confocal image[90]. For example, the total number of pixels related to DNA uptake are counted, and compared to the total number of lysosomes; the overlap of pixels between the two components is determined as colocalization. Using this method, Akita and co-workers were able to quantify the amount of cellular uptake as well as endosomal escape of LipofectAMINE (Invitrogen). However, this method is still limited by its accuracy due to a number of imaging limitations such as thresholding error and objective resolution. These limitations have led to the use of new techniques to quantify subcellular interactions, such as Forster Resonance Energy Transfer (FRET).

FRET labeling exploits the spectral overlap of two fluorochromes to measure formation or dissociation of two components, which are within 10 nm of each other[91]. Only a handful of studies have used FRET to measure the dissociation of polyplex in-vitro. Itaka et al. used FRET to study the condensation of double labeled plasmid DNA in polyplexes. In a similar study, Kong et al. observed the dissociation of branched PEI in cells[92]. Unfortunately, these studies did not take into account spectral overlap error produced by the fluorochromes, thus eliminating the ability to report FRET efficiency[91]. A major drawback to FRET microscopy is the experimental setup, which requires a large number of control samples as well as filter settings to accurately calibrate and calculate

the FRET efficiency. Despite this drawback, the use of FRET techniques has great potential in allowing the user to monitor polyplex dissociation rates as well as cellular and nuclear uptake within one experiment.

1.8. Thesis Overview

Recently, much emphasis has been focused on improving transfection efficiency of cationic polymers through modification of polymer chemical structure. As a result, a vast quantity of polymers with suboptimal transfection efficiency have been established. Yet, the underlined understanding of the structure-functional relationship between the polymer and their subcellular interactions is lacking. Therefore, in this work we focus our attention to understanding said structure-function relationships in a number of different scenarios. Chapter 2 focuses on understanding the effect of polymer molecular weight on transfection efficiency as a result of subcellular interactions. A cationic polymer synthesized in our lab poly(2-aminoethyl methacrylate) (PAEM) using controlled polymerization yielded polymers with narrow molecular weight and degree of polydispersity. Applying a novel approach of quantification of polymer subcellular interactions we were able to deduce a correlation between polymer chain length and transfection efficiency in dendritic cells. In Chapter 3, a more in-depth analysis of the relationship between polymer backbone structure and endocytotic trafficking into dendritic cells was investigated. This was carried out by using two cationic polymers, PAEM and poly(L-lysine) (PLL), which have similar molecular weight but differ primarily in their backbone structure. From this work we were able to show that polymer characteristics such as hydrophobicity, particle size, and shape can dictate endocytotic

routing. Since our previous work focused on use of an immortalized dendritic cell line and do not represent the same dendritic cell type seen *in-vivo*, we turned our attention to understanding the polyplex/cell interaction in a primary bone marrow-derived dendritic cell line in Chapter 4. Understanding the polymer/cell interaction in bone marrow-derived dendritic cell is critical for producing robust *in-vivo* transfection; however, current *in-vitro* transfection of these primary dendritic cell lines is lacking. Therefore, we looked into the subcellular trafficking of PAEM in bone marrow-derived dendritic cells at different states of maturation to understand if increased gene transcription and translation can improve transfection efficiency in these cell lines. One of the potential side effects of polymers is the cytotoxicity due to high molecular weight or hydrophobicity. In Chapter 5 we investigate the potential use of a cytotoxic cationic polymers as a potential anti-cancer drug in 2-dimensional cell viability and 3-dimensional tumor spheroid models, and an *in-vivo* breast cancer tumor model.

Chapter 2: Poly(2-aminoethyl methacrylate) with Well-Defined Chain Length for DNA Vaccine Delivery to Dendritic Cells

2.1. Introduction

In recent years DNA vaccines have shown considerable promise for numerous medical interventions – from prophylactic vaccine strategies that target viral, bacterial or parasitic infections to potential therapeutics for treating infectious diseases, cancer, and autoimmune disorders[93]. DNA vaccination has advantages over conventional vaccines because of its simplicity, flexibility and safety. A plasmid DNA that encodes for a protein antigen of interest is the basic component of a DNA vaccine formulation. Ideally, antigen-presenting cells (APCs) transfected with the DNA vaccine should express the encoded antigen endogenously, process and present the antigenic peptide fragments through the Major Histocompatibility Complex (MHC) molecules, resulting in the generation of antigen-specific immune responses. The most important APCs, the dendritic cells (DCs)[94], are widely considered the ideal target cells of DNA vaccines. Sustained antigen presentation from DCs combined with DC maturation is expected to generate robust adaptive cellular immunity, which is particularly necessary for combating cancer and viral infection[95].

A large number of cationic polymers with diverse structures and properties have been developed for gene delivery[29,96,97], some of which have been evaluated for DNA vaccine delivery[3]. Despite much effort in the past, designing polymers as DNA vaccine carriers has been complicated due to vast possible combinations of physico-chemical variables and by the complex biological/immunological environment in which the carriers are used. For many years the molecular weight, or chain-length, of polymers has

been shown to have significant impact on DNA delivery. The relationship between polymer molecular weight and transfection efficiency has been studied in many polymers such as branched polyethylenimine (PEI)[81], poly(2-dimethylaminoethyl methacrylate) (PDMAEMA)[98], trehalose oligoethylenamine click polymers[99], and polyphosphoramidate (PPA)[100], to name a few. In general, increasing molecular weight will increase gene expression. However, some discrepancies exist[81,91,101] and fundamental understanding of the influence of linear polycation chain-length on the gene transfer process, especially in the context of DNA vaccine delivery to immune cells, remains elusive.

Controlled polymerization techniques such as atom transfer radical polymerization (ATRP)[27,102] make it possible to prepare cationic polymers with defined chain-length in a facile way. Recently we have synthesized polyethylene glycol-*block*-poly(2-aminoethyl methacrylate) (PEG-*b*-PAEM) diblock copolymers with narrow molecular weight distribution by ATRP and have shown that the length of the cationic block exerted significant influence on how the polymer carrier interacted with plasmid DNA and how the polyplexes interacted with DCs[104]. Although the PEG-*b*-PAEM diblock copolymers are useful model systems, they had low transgene expression efficiency in DCs, a significant drawback that limits their practical usage in DNA vaccination. In this study we focused on poly(2-aminoethyl methacrylate) (PAEM) homopolymers with defined chain-length and narrow molecular weight distribution. We investigated comprehensively the colloidal properties of the PAEM/plasmid polyplexes (including stability, particles size and charge), uptake and subcellular trafficking in DCs, and biological/immunological properties in vitro (including cytotoxicity, transfection efficiency, aiming to further elucidate the impact of polymer chain-length on DNA

delivery to DCs and to evaluate the practical value of PAEM as DNA vaccine carrier and immunostimulatory adjuvant.

2.2. Experimental Methods and Materials

2.2.1. Materials

Dulbecco modified low glucose Eagle medium, Penicillin/Streptomycin, 1M HEPES, dPBS and trypsin-EDTA were purchased from Invitrogen (Carlsbad, CA). All cell culture materials were sterile and biological grade. Bovine albumin was obtained from Sigma-Aldrich (St. Louis, MO). Quantification of transfection efficiency was determined by a LSR II flow cytometer (BD Bioscience, San Jose, CA). Oregon Green 488 carboxylic acid, succinimidyl ester was purchased from Invitrogen (Eugene, OR). Labeled polymer was dialyzed using 3,500 molecular weight dialysis tube (SpectraLabs, Milpitas, CA). DNA plasmid was labeled with a Cy5 MIRUS Label*IT* Kit obtained from Mirus Inc. (Madison, W.I.). 4-well LabTek II chamber slides were purchased from Fisher Scientific (Pittsburgh, PA). Cell organelle stains Hoechst 33342 and LysoTracker Green DND-26, as well as SoftFade Gold© mounting media and ascorbic acid were acquired from Invitrogen (Carlsbad, CA). BD-cytofix was purchased from BD Biscience (San Jose, CA). Confocal images were acquired using an Olympus FV-1000 confocal microscope and saved using Olympus FV-1000 imaging software (Center Valley, PA).

2.2.2. Gel retardation assay

Polyplexes of N:P ratios ranging from 1/8 to 16 were prepared by adding 25 μL of polymer solution in 20 mM HEPES (pH 7.4) to 25 μL of DNA plasmid solution (0.2 μg/μL in 20 mM HEPES, pH 7.4) vortexed for 10 s, incubated for 30 min at room

temperature, and analyzed by electrophoresis on a 1.0% agarose gel containing 0.5 $g/mL ethidium bromide.

2.2.3. Heparin competition assay

To determine the strength of DNA binding by polymers with varying chain-length, polyplexes at N:P ratio of 8 were incubated with increasing concentrations of heparin (0.1 to 0.9 IU per μg of DNA) for 20 min at room temperature and analyzed by agarose gel electrophoresis.

2.2.4. Ethidium bromide (EB) exclusion

Polymer solutions were added to pre-mixed EB and plasmid solution with varying N:P ratios from 1/8 to 32 and incubated for 30 min. The intensity of EB fluorescence was recorded by a Bio-Tek Synergy HT plate reader with excitation wavelength of 530/25 nm and emission wavelength of 590/35 nm. DNA/EB solution without any polymer was used as control.

2.2.5. Dynamic light scattering (DLS) and zeta potential measurement

The average hydrodynamic diameter and polydispersity index of polyplexes in HEPES buffer (20 mM) at 25°C were determined using a ZetaPlus Particle Analyzer (Brookhaven Instruments Corporation, Holtsville, NY; 27 mW laser; 658 nm incident beam, 90° scattering angle). Polyplexes with N:P ratios ranging from 1/4 to 32 were prepared as described above and diluted 20 times to a final volume of 2 mL in HEPES buffer before measurement. Simultaneously the zeta-potential of the polyplexes was determined using the ZetaPal module of the Particle Analyzer.

2.2.6. Cytotoxicity assay

The cytotoxicity of free polymers was evaluated by an MTT (3-(4,5-dimethyl-thiazol-2-yl)-2,5-diphenyl tetrazolium bromide) assay[18]. DC 2.4 cells were seeded into 96-well plates at 6000 cells/well and cultured with polymers of various concentrations for 24 h in DC 2.4 media (DMEM low glucose, 10% FBS, 10 mM HEPES, 100 U/mL penicillin/streptomycin) at 5% CO_2 and 37°C. MTT in PBS (5 mg/mL, 20 μL) was added to each well reaching a final concentration of 0.5 mg/mL. After 4 h, unreacted MTT was removed by aspiration. The formazan crystals were dissolved in 150 μL of DMSO and the absorbance was measured at 570 nm using a Bio-Tek Synergy HT plate reader. Cell viability was calculated by [Absorbance of cells exposed to polymers]/[Absorbance of cells cultured without polymers] in percentage.

2.2.7. Fluorescence labeling of polymer and plasmid

For subcellular trafficking studies, both the PAEM polymers and DNA plasmid were covalently labeled with fluorophores. PAEM was labeled with Oregon Green 488 carboxylic acid succinimidyl ester (Invitrogen) using a method previously described[81] followed by purification by dialysis (MWCO 3,500). The DNA plasmid was labeled with a Cy5 fluorophore using a MIRUS LabelIT Kit (Mirus, Madison, WI) according to manufacturer's protocol. After the labeling reaction, the DNA plasmid was purified from excess dye by means of ethanol precipitation according to the manufacturer's protocol. Both purified labeled PAEM polymer and DNA plasmid were stored at -20°C until use.

2.2.8. Cellular uptake and subcellular trafficking

DC 2.4 cells were seeded in 4-well LabTek II glass chamber slides (Fisher Scientific, Pittsburgh, PA) at a density of 100,000 cells per well in 1 mL of media. To

visualize cellular uptake and polyplex intracellular dissociation, polyplexes were formed using fluorescently labeled PAEM and luciferase plasmid. Prior to transfection, the DC 2.4 media was removed and the cells washed once with warm PBS and replaced with serum-free DC 2.4 cell media. Cells were incubated with polyplexes for 1, 4, or 24 h at 37°C, 99% humidity, and 5% CO_2. For the 24-h samples, the serum-free media was removed after 4 h and the cells were washed twice with warm PBS and replaced with complete DC 2.4 media containing 10% serum and incubated for an additional 20 h. Prior to confocal microscopy imaging, Hoechst 33342 (Invitrogen) was added to each chamber at a final concentration of 30 μM to stain the cell nuclei, and the samples were washed and fixed using BD cytofix fixation buffer (BD-Bioscience, San Jose, CA) according to the manufacturer's protocol. The cells were then mounted with SlowFade Gold© anti-fade reagent (Invitrogen), covered with a coverslip, and sealed with clear nail polish. Cell images were captured with an Olympus FV-1000 confocal microscope equipped with an Olympus 60x/1.42 NA oil-immersion lens (Center Valley, PA). The fluorescence intensity of each fluorophore was adjusted using individual single-fluorophore positive and cell-only negative controls. The Cy5 label was excited at 643 nm and detection of emission was set at 670 nm. Hoechst 33342 was excited at 405 nm and emission detected at 451 nm. Imaging limits (z- slices) were set to collect the top and bottom boarders of the cells at a step size of 0.4 μm and 800 pixel resolution. Images of at least three fields of view were collected for every sample.

To determine endosomal colocalization, DC 2.4 cells were transfected with polyplexes formed with non-labeled PAEM and Cy5-labeled luciferase plasmid. Thirty minutes prior to imaging, cells were stained with Hoechst 33342 for 20 min followed by

LysoTracker Green DND-26 (Invitrogen) at a final concentration of 100 nM according to manufacturer's protocol. The cells were then washed with PBS and mounted with ascorbic acid at a final concentration of 5 μM to minimize photo-bleaching. The LysoTracker Green fluorochrome was excited at 488 nm and emission detected at 520 nm. All samples were kept on ice until imaged.

2.2.9. Image analysis and quantification

The confocal fluorescence microscopy images of cellular uptake and subcellular trafficking were analyzed using ImageJ software and image quantification was carried out using a method developed by Akita et al. Imported confocal images were opened in individual color components and converted to 8-bit images. Individual cells used for the analysis were then randomly isolated from each image. Cellular uptake of Cy5-labeled plasmid was measured by individually thresholding the z-slices of each cell and calculating the total pixel area within a region of interest (ROI) drawn around the cell membrane. Polyplex intracellular dissociation was quantified by measuring the degree of colocalization between Oregon Green 488 labeled PAEM and Cy5 labeled plasmid. Each complex component was thresholded individually for each z-slice. The total pixel area of the Cy5-plasmid signal was calculated. Colocalization of the two fluorophores was measured as the spatial overlap between the two individual thresholded images in the unit of total pixel area, using the ImageJ colocalization plug-in. The percentage of polyplex dissociation was determined as one subtracting the ratio between the Oregon Green/Cy5 colocalized total pixel area and the total Cy5 pixel area. The same method was applied to determining the percentage of endosomal colocalization. Nuclear localization of plasmid was quantified by calculating the total pixel area of Cy5 plasmid within a ROI of the

nuclear membrane. The geometry of nuclei was determined by stacking the z-slices into 3-D images and orthogonal views to verify that the Cy5-plasmid signal was indeed within the boundary of the nucleus. A total of 30 cells were analyzed for each experimental group based on the coefficient of variance[90]. Note that fluorescence intensity of all the images was not adjusted in ImageJ prior to quantification.

2.2.10. Complex dissociation visualization by Förster resonance energy transfer (FRET) sensitized emission

Utilization of FRET sensitized emission was used to verify the dissociation of the polymer/DNA complexes at 24 hours in murine DC 2.4 cells. Prior to imaging, the PAEM polymers were labeled with Oregon Green-488 as described above, while the luciferase DNA plasmid were labeled with a Cy3 fluorophore using a MIRUS Label*IT* kit according to the manufacturers protocol. Transfection of DC 2.4 cells were carried out according to the same procedures as described previously for cellular uptake and complex dissociation. DC 2.4 cells were also transfected with FRET controls consisting of non-labeled PAEM complexed with Cy3-LUC DNA and Oregon Green-488 labeled PAEM complexed with non-labeled LUC DNA in separate individual wells. After 24 hours, cells were washed with dPBS and fixed with BD-Cytofix according to the manufacturers protocol, than mounted using SlowFade Gold anti-fade media. The FRET polymer/DNA complex samples and controls were imaged using an Olympus FV-1000 confocal microscope equipped with an Olympus 60x/1.42 NA oil-immersion lens. Three individual ROIs were imaged for each the FRET control and FRET polymer/DNA complex samples according to the Olympus sensitized emission FRET protocol. FRET control images and polymer/DNA complex FRET sample images were analyzed and quantified using by the FV-ASW 1.5 software precision FRET (pFRET) sensitized

emission function. The software analyzed the median z-slice of the cell and reported images of the Oregon Green-488 PAEM sample emission, Cy3 LUC-DNA sample emission, and the polymer/DNA pFRET.

2.2.11. Gene transfection in vitro

DC 2.4 cells were seeded into 12-well plates at 100,000 cells/well and cultured overnight. For transfection under serum-free condition, the cell media was removed and cells washed by PBS twice followed by adding DC 2.4 media without serum. Transfection with polyplexes of the GFP plasmid lasted for 4 h at 5% CO_2 and 37°C. The media was then discarded, cells washed by PBS twice, and cultured in serum-containing media for another 20 h before GFP level was recorded. For transfection in media containing 10% serum, DC 2.4 cells were incubated with polyplexes for 24 h at 5% CO_2 and 37°C. The cells were harvested by treating with trypsin-EDTA, dispersed in FACS buffer (PBS containing 1% bovine serum albumin), and analyzed using a BD LSR II flow cytometer. DC 2.4 cells were also transfected by polyplexes of the luciferase plasmid under the same conditions to exclude the autofluorescence of cells. Percentage of GFP^+ cells was determined using Flowjo. The GFP positive gate was drawn based on the luciferase control where false positive frequency was restricted to below 0.2%.

2.3. Results and Discussion

2.3.1. Longer PAEM chain-length enhances cellular uptake of polyplexes

Cy5-labeled luciferase plasmid complexed with non-labeled PAEM of different chain-length at the N:P ratio of 8 was used to visualize cellular uptake in DC 2.4 cells after 1, 4, and 24 h by confocal fluorescence microscopy (Figure 2.1.). The level of Cy5-

plasmid fluorescence inside cells was then quantified based on the confocal images using a method reported by Akita *et al* [90] (Figure 2.1.). The confocal images showed that cellular uptake of the plasmid began within the first hour of transfection, with all three PAEM chain- lengths resulting in similar quantities of Cy5-plasmid inside the cells. By 4 h and 24 h the amount of plasmid taken up by the cells continued to rise and there was clearly a dependence on chain-length. The quantity of cellular uptake of plasmid complexed to $PAEM_{150}$ was significantly ($p < 0.05$) higher than that of either $PAEM_{75}$ or $PAEM_{45}$ at 4 h. The uptake of plasmid complexed to $PAEM_{75}$ arrived at a level similar to that of $PAEM_{150}$ polyplexes by 24 h, yet both remained significantly higher than the shorter $PAEM_{45}$ polyplexes (Figure 2.1.). These results indicate that the uptake of polyplexes by dendritic cells was more efficient when relatively longer cationic polymers were used. It is possible that longer cationic PAEM chains may form more stable polyplexes (demonstrated by heparin exclusion), which might interact with the cell membrane more strongly than polyplexes formed from shorter polymer chains, thus facilitating internalization into the cells[105] .

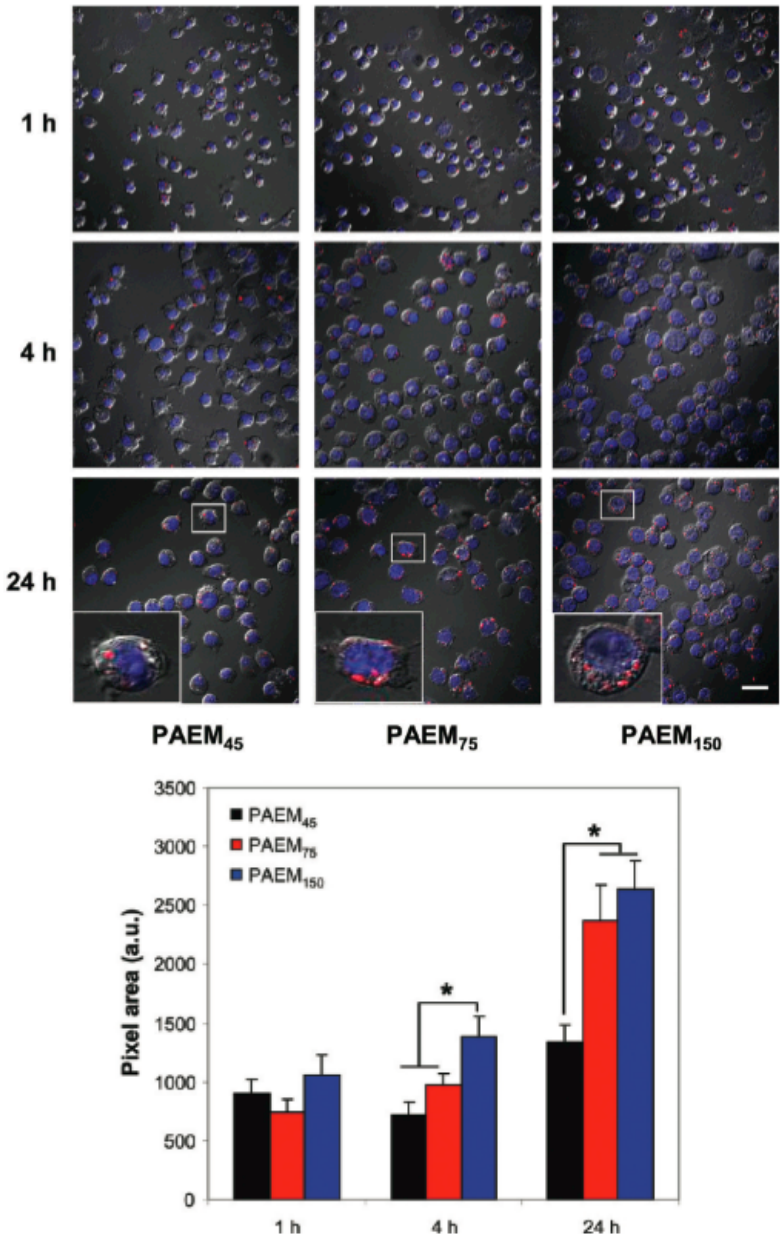

Figure 2.1. Cellular uptake of plasmid. (A) Representative confocal fluorescence microscopy images of DC 2.4 cells transfected by polyplexes (N:P ratio of 8) at various time points. Red: Cy5-labeled plasmid. Blue: Hoechst 33342 staining cell nuclei. Shown are fluorescence overlaid with white-light images. Scale bar: 25 μm. (B) Quantification of cellular uptake. Mean ± SE, 30 cells for each sample were counted, *$p < 0.05$.

2.3.2. Shorter PAEM chain-length facilitates intracellular dissociation of polyplexes

To achieve transgene expression, the DNA plasmid must dissociate from the polymer carrier at some point after being taken up by the cells. Here confocal fluorescence microscopy images were used to assess the effect of polymer chain-length on polyplex dissociation after internalization (Figure 2.2), which was then quantified by measuring the spatial colocalization of fluorescence signals from the Cy5-labeled DNA plasmid and Oregon Green 488-labeled PAEM at various time points (Figure 2.2). All three PAEM chain-lengths possessed similar levels of bound Cy5-plasmid (~75%) at 1 h. However, as time went by, the percentage of intact polyplexes decreased with the fastest rate of dissociation occurring with the shortest $PAEM_{45}$. Four hours post-transfection the percentage of intact polyplexes of $PAEM_{45}$ dropped to below 70%. At 24 h a clear chain-length dependence of polyplex dissociation was established with the shortest $PAEM_{45}$ having the lowest fraction (53%) of intact polyplexes. Interestingly, the difference in dissociation between $PAEM_{75}$ and $PAEM_{150}$ polyplexes was not statistically significant, in spite of $PAEM_{150}$ being twice as long as $PAEM_{75}$ (Figure 2.2). Overall, it appeared that within 24 h all three types of polyplexes experienced various degrees of dissociation inside cells.

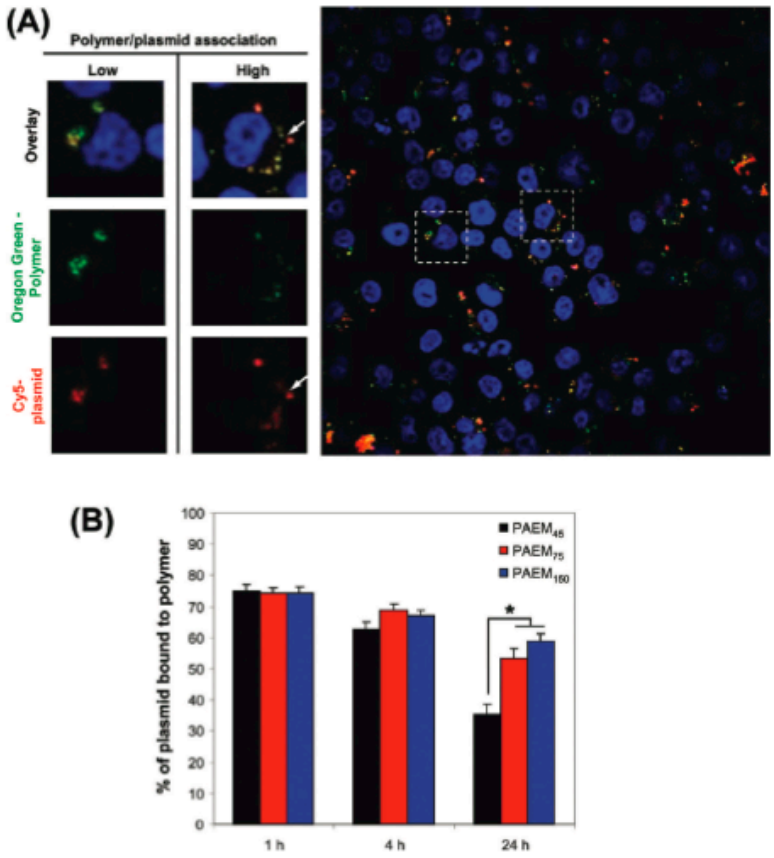

Figure 2.2. Intracellular dissociation of polyplexes. (A) Representative confocal fluorescence microscopy images of DC 2.4 cells transfected by polyplexes (N:P ratio of 8) at 24 h. Red: Cy5-labeled plasmid. Green: Oregon Green-labeled polymer. Blue: Hoechst 33342 staining cell nuclei. Arrows point to polyplexes that remained intact or dissociated (labeled "low" or "high", respectively). (B) Quantification of intracellular polyplex dissociation. Mean ± SE, 30 cells for each sample were counted, *$p < 0.05$.

Shorter polymer chain-length favored polyplex dissociation more than longer chains due to weaker binding between short polymer chains and DNA, which was corroborated by the heparin competition experiment. These results obtained by using a 3-D fluorescence colocation method can be confirmed by FRET measurement (Figure 2.3), showing lower pFRET in polyplexes with shorter PAEM chains. These findings demonstrated the possibility of using polymers of defined chain-length to modulate the time course of polyplex dissociation, and in turn, to control transgene expression.

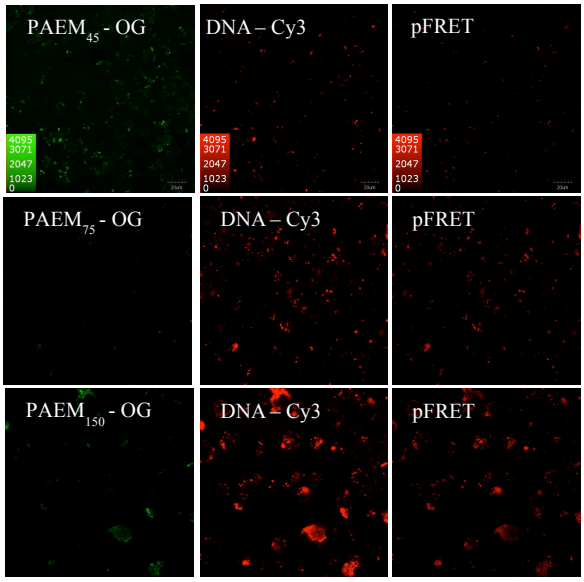

Figure 2.3. FRET analysis of Oregon Green-labeled PAEM and Cy3-labeled plasmid DNA polyplexes at 24 h of transfection. The intensity of pFRET is dependent on PAEM chain-length. Shorter PAEM chains show reduced pFRET, indicating more polyplex dissociation.

2.3.3. Endolysosomal localization is not clearly dependent on polymer chain-length

The colocalization of Cy5-labeled plasmid DNA and endolysosome was observed by confocal fluorescence microscopy (Figure 2.4A) and quantified by calculating the amount of overlap between the fluorescent signals of Cy5 and LysoTracker Green, a marker for endolysosome (Figure 2.4B). Unlike cellular uptake and polyplex dissociation, there was no overall chain-length dependence for endolysosomal localization of the polyplexes. All three polymers showed similar level of endolysosomal entrapment at 1 h (around 25 to 35%, no statistical significant difference), which increased to approximately 55% by 24 h. Interestingly, with the exception of PAEM150, endolysosomal entrapment of PAEM45 and PAEM75 polyplexes increased from 1 to 24 h. It could be that the polyplexes escaped endolysosomal as quickly as within the first hour of internalization, but they were recaptured by acidic subcellular vesicles (such as autophagosomes) at later times. Alternatively, rather than escaping from endolysosome,

the majority of the polyplexes bypassed the endocytic pathway and were internalized via other (such as caveolae-mediated) pathways. The elucidation of the internalization mechanisms of the PAEM/DNA polyplexes will require further studies.

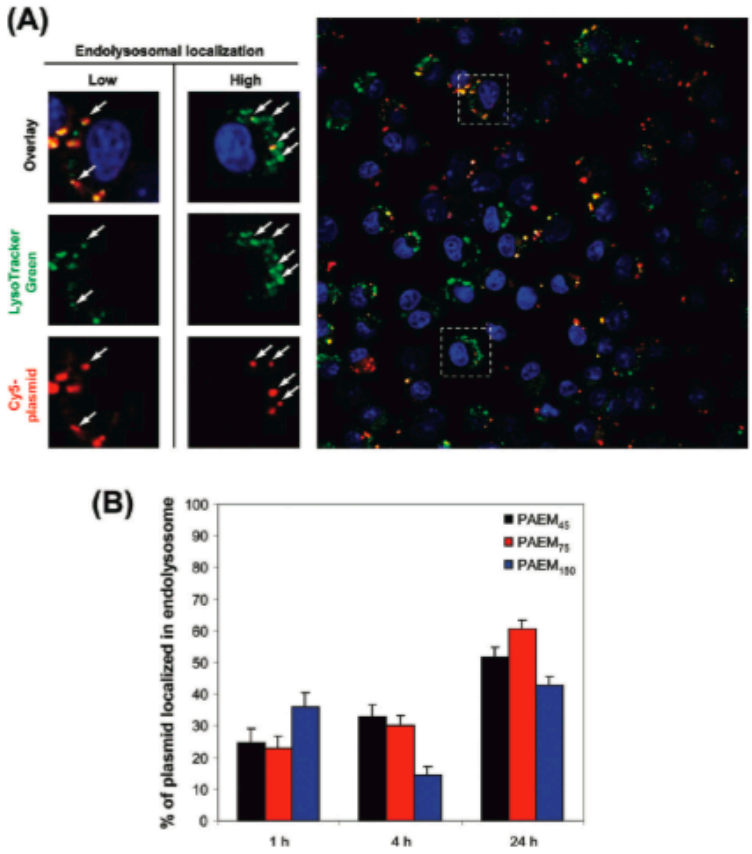

Figure 2.4. Endolysosomal localization of plasmid. (A) Representative confocal fluorescence microscopy images of DC 2.4 cells transfected by polyplexes (N:P ratio of 8) at 24 h. Red: Cy5-labeled plasmid. Green: LysoTracker Green. Blue: Hoechst 33342 staining cell nuclei. Arrows point to regions where plasmid was or was not localized in the endolysosome (labeled "high" or "low, respectively). Low degree of localization plasmid that remained intact (low) or dissociated (high). (B) Quantification of plasmid localized in the endolysosome. Mean ± SE, 30 cells for each sample were counted, *$p < 0.05$.

2.3.4. Longer PAEM chain-length promotes nuclear localization of polyplexes but does not favor the release of free plasmid

The efficiency of plasmid to be trafficked into the nucleus was observed by confocal fluorescence microscopy (Figure 2.5A) and quantified using the following three parameters: (1) the total fluorescence intensity of Cy5-plasmid (including the polyplexes

and free plasmid) inside the nucleus; (2) the fluorescence intensity of free plasmid inside the nucleus; and (3) the number of cells with detectable fluorescence signal of the Cy5-plasmid (as polyplex or free) in the nucleus (Figure 2.5B). Care was taken to ensure that only Cy5-plasmid signals within the boundary of the nuclei was counted. One hour after transfection, there was a minute amount of Cy5-plasmid found in the nuclei of 1 or 2 cells out of a total of 30 individual cells examined. Four hours later, slightly more Cy5 signal was found in the nuclei of less than 10 cells. By 24 h, similar to what was seen with cellular uptake (Figure 2.1), the total amount of Cy5-plasmid localized within the nucleus exhibited a dependence on polymer chain-length, with $PAEM_{75}$ and $PAEM_{150}$ showing significantly higher ($p < 0.05$) nuclear uptake than that of $PAEM_{45}$ (Figure 2.5B). More cells transfected using $PAEM_{75}$ and $PAEM_{150}$ were found with Cy5-plasmid in the nucleus (14 and 16 out of 30 cells, respectively) than $PAEM_{45}$ (10 out of 30 cells). More importantly, there was substantial amount of nuclear Cy5-plasmid that had apparently dissociated from the polymer carrier by 24 h (Figure 2.5B). Although the longest $PAEM_{150}$ delivered the highest amount of free Cy5-plasmid to the nucleus, the fraction of the free plasmid was below 0.5 – the smallest of the three polymers. Taken together, it appeared that longer PAEM chains promoted the overall cellular uptake and the subsequent nuclear uptake of plasmid, but if the polymer chain was too long, then the release of free plasmid from the polymer might be hindered. Because efficient transgene expression requires maximizing the amount of free plasmid in the nucleus, it may be more ideal to use a polymer with moderate chain-length (such as DP of 75) so as to facilitate both nuclear transport and dissociation of polyplexes inside the nucleus.

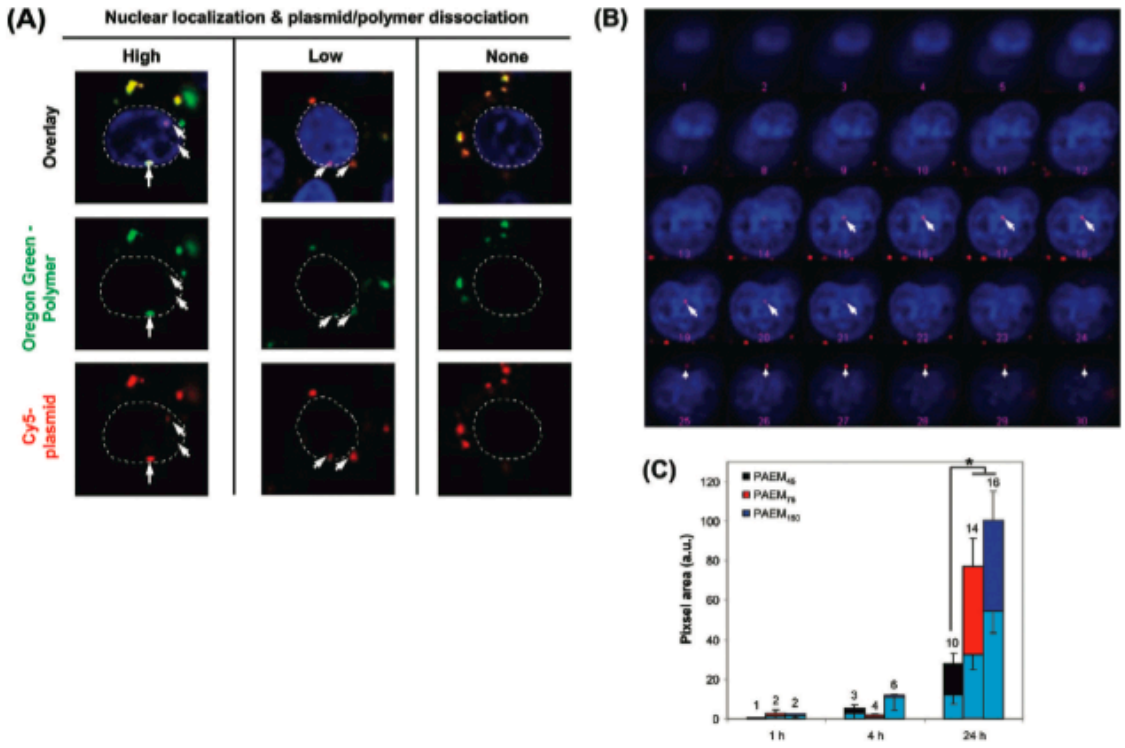

Figure 2.5. Nuclear localization of plasmid and dissociation of polyplexes. (A) Representative confocal fluorescence microscopy images of DC 2.4 cells transfected by polyplexes (N:P ratio of 8) at 24 h. Red: Cy5-labeled plasmid. Green: Oregon Green-labeled polymer. Blue: Hoechst 33342 staining cell nuclei outlined in dotted white lines. Arrows point to regions where plasmid signal was found in the nucleus. Shown are examples of cell nuclei containing free plasmid ("high"), polyplex-bound plasmid ("low"), or no plasmid ("none"). (B) A montage of z-slices of a cell nucleus. Arrows in frames 15−21 identify plasmid signal inside the nucleus. Arrows in frames 25−30 point to plasmid signal at the edge of nuclear membrane. (C) Quantification of amount of plasmid (free and polyplex-bound) localized in the cell nucleus. The top portion of the bars represents the amount of free plasmid. Mean ± SE, 30 cells for each sample were counted, *$p < 0.05$. The numbers are the frequency of cells within a 30-cell population that contained positive signal of the plasmid inside their nuclei.

2.4. Conclusions

Cationic PAEM polymers with precisely controlled chain length were synthesized and characterized for delivering plasmid DNA to antigen-presenting dendritic cells. Through a comprehensive study we revealed correlation between polymer chain length and colloidal properties of the polyplexes, transfection efficiency, uptake in dendritic cells and subcellular trafficking. Thus, the structurally simple and defined PAEM polymer is not only a useful model material for understanding structure-function relationship in nonviral gene delivery but also may be a practically effective, immunostimulatory DNA vaccine carrier.

Chapter 3: Structure Function Mechanisms of Well-defined Synthetic Gene Carriers for Delivery to Dendritic Cells

3.1. Introduction

DNA vaccines have recently become the focus of treatment for inherent genetic diseases as well as cancer, by activating and inducing a patient's own immune system[5]. Activation of the immune system is orchestrated by antigen-presenting cells, such as dendritic cells, which have been shown to induce activation of both the cell-mediated and humoral branches of the immune system, upon capture of foreign antigen[15]. In the case of DNA vaccines, an infection would be imitated by delivering an exogenous DNA plasmid encoding for the antigen into the patient, in order to activate an immune response. However, experiments have shown that despite being able to be taken up by dendritic cells[26,27], naked DNA plasmid offers limited delivery efficiency *in-vivo*, as a result of the DNA plasmid being easily degraded by DNAse enzymes within minutes[3,29], making it prone to tissue clearance[30]. Naked DNA must also overcome subcellular events such as cellular uptake, which confers the internalized DNA into closed vesicles (endosomes, lysosomes or phagosomes), where the pH is progressively lowered to 5.0-6.5, denaturing the DNA[24]. In order to increase the effectiveness of DNA-based therapeutics, the DNA plasmid must be protected by an appropriate delivery system that offers high stability, protection from nucleases, and promote cellular uptake of the DNA plasmid[106]. Over the years a number of nucleic acid transfer vectors have been designed to protect plasmid DNA from cellular degradation. Two of the most commonly used and researched vectors are viral and non-viral vectors. Viruses make an ideal candidate as nucleic acid vectors since they have evolved mechanisms, which allow them to avoid

lysosomal trafficking[32]. However, viral vectors exhibit high immunogenicity, limited size of inserted DNA, and high potential of the virus reverting back to its wild-type phenotype[29]. Viruses high immunogenicity makes it difficult for repeat treatments and can cause a dangerous immune response in patients with compromised immune systems[11]. The limitations of viral vectors have led to the development of non-viral vectors such as: cationic polymers and liposomes. Cationic polymers are an ideal candidate to use for DNA vaccines, since they offer a number of advantages over viral vectors such as: high stability, low toxicity, and larger cargo capacity[29].

Poly(l-lysine) (PLL) and polyethyleneimine (PEI) were two of the first polycationic polymers used due to their ability to form nanoparticles by condensing DNA via electrostatic interaction[3,96]. However, the limited transfection efficiency of PLL, primarily due to a lack of endosomal escape[3,96], and the intolerable cytotoxicity and limited degradability of PEI at a high molecular weight[53,54], have led to modifications to the chemical and structural properties of PEI and PLL. Modifications that include the addition of poly(ethylene glycol) (PEG)[3], histidine[96], and disulfide bonds[107] in an attempt to improve cytotoxicity, buffering capacity, and degradation. Despite these variations to PLL and PEI, both continue to have limited applications *in-vivo*[3]. Recently, focus has turned to the development of novel cationic polymers systems, which offer the potential of understanding the polymer structure-function relationship in order to improve transfection efficiency. The development of high throughput degradable polymer libraries, such as poly(β-amino ester) (PβAE), have been designed to offer a wide range of polymers for non-viral gene therapy with varying physiochemical characteristics[61]. However, despite the high volume of high throughput synthesized PBAE polymers, only

a small number of PβAE polymers proved sufficient for gene delivery[65]. The addition of amine end cap groups and the type of amine species have shown to be of vital importance to achieving successful transfection. For example, the transfection efficiency of PβAE in human primary cells was improved with the addition terminal primary amine end-cap to the polymer backbone structure[63]. Most recently, Anderson et al. have shown that the transfection efficiency of trehalose "click" polymers in HeLa cells in the presence of serum can be improved with the addition of an oligoethyleneamine end-cap[108].

In addition to amine functionality, it is well known that molecular weight of a polymer effects gene delivery[65], and in some cases, stability[96]. Recently, a study focusing on the effect of molecular weight of PβAE has shown that the transfection efficiency increases with higher molecular weights[109]. However, a caveat to these experiments is that the molecular weight has a high polydispersity, which introduces another variable into the structure-function equation. Controlled polymerization techniques such as atom transfer radical polymerization (ATRP) enable the synthesis of polymers with well-defined molecular weight and narrow weight distribution. Recently, we have synthesized, poly(2-aminoethyl methacrylate) (PAEM) a linear polycationic polymer with three defined molecular weights and narrow polydispersity. A study recently carried out in our lab, showed that longer chain PAEM have better transfection efficiency due to increased cellular and nuclear uptake, when compared to shorter chain polymers[110]. Despite the large inventories of polymer structures and physiochemical combinations, non-viral polymer vectors continue to have inadequate gene expression[23].

This is primarily due to the lack of understanding as to which basic polymer chemical structure(s) are necessary to overcome specific subcellular barriers. Recently, an effort has been made to understand the structure-function relationship of DNA complexes with a number of *in-vitro* subcellular events by using fluorescent microscopy such as cellular uptake[81,90,91,111-116], complex dissociation[81,88,90,111,112,117,118], endosomal escape[81,88,90,111-113,115,118], and nuclear[81,86,88,90,111,112,114,117]. Unfortunately, a majority of these studies only use microscopy images for qualitative analysis, with a handful of studies offering quantified data using either Forester resonance energy transfer (FRET)[91,112,114] or fluorescence colocation methods[90,111,117]. However, none of these studies look at the effect of polymer backbone structure or defined molecular weight.

In this study we investigated the structure-function relationship of two linear polycationic polymers ($PAEM_{150}$ and PLL_{150}) with similar chemical side chain structures, degree of polymerization, and molecular weight. We hypothesize that the variation in the transfection efficiency among different polymers is dependent on the polymers chemical backbone structure, which may dictate the polymer's ability to facilitate endosomal escape, timely complex dissociation, and nuclear uptake. Interaction of the polymer/DNA complexes was visualized and quantified with specific subcellular organelles via fluorescent confocal microscopy[88,90,118] over a course of time using a colocalization quantification technique designed and reported by Akita et al. Quantification of the polycationic polymers revealed similar amounts of cellular uptake for $PAEM_{150}$ and PLL_{150}. However, unlike $PAEM_{150}$, PLL_{150} was unable to overcome endosomal entrapment as well as complex dissociation, which limited nuclear translocation of the DNA plasmid. These results suggest that the difference in endosomal

escape between the polycationic polymers is the main subcellular barrier responsible to for the variation in transfection efficiency, by limiting complex dissociation and nuclear uptake.

3.2. Materials and Methods

3.2.1. Preparation of poly(2-aminoethyl methacrylate)/poly(L-lysine)/poly(2-aminoethyl metharylate amine)

Toluene (Aldrich) was dried by refluxing over sodium and distilled. The monomer (N-(tert-butoxycarbonyl)aminoethyl methacrylate) (tBAM) was synthesized as described before[119]. Ethyl α-bromoisobutyrate, copper (I) chloride (CuCl) and 2,2′-dipyridyl (bPy) were purchased from Sigma. Other chemicals and solvents were purchased from Sigma and used without further purification. The ATRP followed the procedures modified as described previously[104]. A glass two-neck flask was charged with tBAM, CuCl, bPy, and the system was degassed three times. Dried degassed toluene and ethyl α-bromoisobutyrate were added, and the mixture was heated at 80 °C for 8 h. The reaction was terminated by exposing the system to air. The reaction solution was then diluted by dichloromethane (DCM) and passed through a basic aluminum oxide column to remove the copper complex. The resulting product was precipitated in hexane twice and dried in vacuum at room temperature for 2 days. Three different monomer to initiator feed ratios were used in order to obtain PtBAM homopolymers with varying chain-length. To remove the Boc groups, 0.8 g of PtBAM was dissolved in 5 mL of trifluoroacetic acid (TFA) and stirred for 2 h at room temperature. TFA was then removed by evaporation, and the oil residue was rinsed three times with diethyl ether. The resultant precipitate was collected by filtration, washed twice by diethyl ether, and

dried overnight in a vacuum. Afterward, the polymers were washed with NaOH solution at pH 9.0, instantly put into dialysis tubing with MWCO 3.5k, and dialyzed against distilled water for 3 days. The final PAEM polymers were obtained by lyophilization. The ^{1}H and ^{13}C NMR spectra of the polymers were acquired on a Varian Unity spectrometer (300 MHz) using $CDCl_3$ (for PtBAM) and D_2O (for PAEM) as solvents. Chemical shifts were recorded in ppm and referenced against tetramethylsilane (TMS) and D_2O, respectively. The PtBAM Gel Permeation Chromatography (GPC) experiment was performed at 35 °C in $CHCl_3$ with a flow rate of 1 mL/min using a Hewlett-Packard 1100 series liquid chromatography equipped with three PL gel 5μm mixed columns (Jordi Gel columns of 500, 103, and 104 Å pore sizes) and a Hewlett-Packard 1047A refractive index detector. The GPC instrument was calibrated with polystyrene standards (Polymer Laboratories). All sample solutions were filtered through a 0.22 μm filter before analysis. Poly(L-lysine) was synthesized by open chain polymerization by Dr. J. Cheng and Dr. H. Lu at the University of Illinois at Urbana-Champaign.

RAFT polymerizations of AEM were conducted in a similar procedure of $PAEM_{Am}$[102]. Concretely, in a 10-mL flask, AEM (1 g, 6.0 mmol) was dissolved in doubly distilled water (2.4 mL) followed by the addition of 1 mL of 1,4-dioxane solution of CTP (16.8 mg, 0.06 mmol) and ACVA (8.4 mg, 0.03 mmol). After degassing via three freeze-thaw cycles, the flask was placed in an oil bath for polymerization at 70 °C for 9h. The crude polymer was obtained by precipitating the above solution in acetone. The white power was further dialyzed against distilled water in dialysis tubing with MWCO 3.5k for 3 days and freeze dried to get PAEM.

3.2.2. Polymer/DNA complex formation and characterization

Polyplexes were prepared at an N/P ratio of 8:1 by adding 25 μL of polymer solution (0.1 mg/mL polymer in 20 mM HEPES) to 25 μL of DNA plasmid solution (0.08 μg/μL in 20 mM HEPES). The DNA plasmid used was either encoded for firefly luciferase (pCMV-Luc) or plasmid green fluorescent protein (pEGFP-N1) (Elim Biopharm, Hayward, CA). The pEGFP-N1 DNA plasmid is used for transfection efficiency and pCMV-Luc DNA plasmid is primarily used for subcellular trafficking studies. The solution was vortex and allowed to incubate in the dark at room temperature for 30 minutes, prior to transfection.

The effective diameter of the complex was measured by dynamic light scattering using a 90plus dynamic light scattering particle analyzer (Brookhaven Instruments, Holtsville, NY). The polymer complexes zeta-potential was measured by using the 90plus particle analyzer. Complex binding was measured by an ethidium bromide (Invitrogen, Eugene, OR) assay, which quantifies the level of ethidium bromide exclusion from the plasmid DNA as a result of polymer binding at varying N/P ratios. The relative fluorescent intensity of ethidium bromide was measured by means of spectophotometry, using a Bio-Tech System (Winooski, VT) plate reader at an excitation wavelength of 530/25, and set to detect an emission wavelength of 590/35 nm. Cytotoxicity of the polyplexes in murine DC2.4 cells were evaluated by MTT assay using the method previously described elsewhere[104].

3.2.3. In-vitro cell preparation and transfection efficiency of murine DC2.4 dendritic cells.

Murine DC 2.4 cells were cultured in complete cell culture media (Dulbecco modified Eagle medium low glucose supplemented with 10% fetal bovine serum, 1%

penicillin/streptomycin, and 1% HEPES (1M) Invitrogen, Carlsbad, CA) and maintained at 37°C, 99% humidity, and 5% CO_2. For transfection efficiency studies, cells were plated in a 12-well cell culture plate (Corning, Corning, NY) at a cell density of 100,000 cells per well, 24 hours prior to transfection. Prior to transfection, the cell media was removed and the cells washed once with dPBS (Dulbecco phosphate buffer solution, pH 7.4; Invitrogen, Calsbad, CA), and replaced with complete serum-free DC 2.4 media (Dulbecco modified Eagle medium low glucose supplemented with 1% penicillin/streptomycin, and 1% HEPES (1M)). Cells were then transfected with prepared polymer/DNA complexes as previously described and incubated at 37°C, 99% humidity, and 5% CO_2 for 4 hours, after which the cell media was removed and the cells were washed 2x with dPBS and replaced with complete DC 2.4 media containing 10% serum and allowed to incubate for an additional 20 hours at 37°C, 99% humidity, and 5% CO2. After the 24 hour time point, the cell media was removed and the cells again washed with dPBS followed by 2-4 minutes incubation with trypsin-EDTA at room temperature. The wells were then washed with dPBS and placed into FACS tubes, and the cells were spun down to pellet. The cell supernatant was removed and the cells were re-suspended in 300μL FACS buffer (1% Bovine serum albumin (Sigma-Aldrich, St. Louis, MO), 1% sodium azide (Sigma) in dPBS (Gibco)). The percentage of EGFP and mean fluorescent intensity (MFI) were characterized by a LSR II flow cytometer (Bioscience, San Jose, CA). Polymer/luciferase-DNA plasmid controls were also included for each polymer to calibrate for the polymer autofluorescence.

3.2.4. Cellular/nuclear uptake and dissociation of polymer/DNA complexes

Confocal microscopy subcellular trafficking images of polymer/DNA complexes were carried by fluorescently labeling both the polymer and DNA prior to complex formation. Labeling of the polymer vectors were carried out by a method previously described elsewhere[81] using Oregon Green 488 carboxylic acid, succinimidyl ester (Invitrogen, Eugene, OR). The Oregon Green label was diluted in DMSO to a concentration of 10 mg/mL. The polymer vectors were then incubated while stirring with the Oregon Green label at a final concentration of 1 mg/mL for 1 hour in the dark at room temperature, followed by an additional 1 hour incubation in the dark without stirring. After which, excess dye was removed by a 3,500 molecular weight dialysis tube (SpectraLabs, Spectra/Por Dialysis Membrane in 0.1% sodium azide), and placed into 1-liter of de-ionized water and stirred at 4° C. After 12 hours the de-ionized water was changed and the sample stirred for an additional 12 hours. Finally, the de-ionized water was removed and changed to 1-liter of 20mM HEPES and stirred for 12 hours. The sample was then removed and placed into a sterile 15-mL Falcon tube and frozen at -80° C overnight. Finally, the samples were placed on a lyophilizer for 48-72 hours to freeze dry. The samples were then weighed and re-suspended in 20mM HEPES buffer at a concentration of 2.5 mg/mL. The luciferase DNA plasmid was labeled using a MIRUS Cy5 Label*IT* Kit (Mirus Inc., Madison, WI). Labeling was carried out according to the manufacturer's protocol. Purification of excess dye from the Cy5 labeled DNA was carried out by means of ethanol precipitation according to the manufacturer's protocol. Following labeling the polymer and luciferase DNA plasmid were each stored at -20°C until use.

For confocal imaging studies, cells were plated in LabTek II glass chamber slides at a cell density of 100,000 cells per well. The formation and transfection of fluorescently-labeled polymer/DNA complexes were prepared using the same methods as previously described above. Thirty minutes prior to imaging, Hoechst 33342 blue nuclear stain (Invitrogen, Eugene, OR) was added to each chamber at a final concentration of 30 μM according to manufacturer's protocol. After which, the media was removed and the samples washed with dPBS and fixed using BD cytofix fixation buffer (BD Bioscience) according to the manufacturer's protocol. Cells were then mounted using SlowFade Gold© anti-fade reagent (Invitrogen), and a coverslip was placed over the chamber and sealed with clear nail polish. Confocal images were captured using an Olympus FV-1000 confocal microscope (Olympus) using a 60x/1.42 NA oil-immersion objective. Individual fluorophore intensity was adjusted using an individual standard for each fluorophore prior to imaging by the Olympus FV-1000 software. The Cy5 label were excited using a 643 nm wavelength and detection was set for a 670 nm emission wavelength. The Hoechst 33342 label was excited by a 405 nm wavelength and a 451 nm emission wavelength were collected. Imaging limits (z-slices) were set to collect the top and bottom boarders of the cell at a step size of 0.4 μm and 800 pixel resolution. A total of three images were collected for each experimental and control sample. Fluorescent intensity was increased equally for each representative image used for publication.

3.2.5. Endosomal entrapment

This experiment followed the same procedure used for studying cellular uptake by confocal microscopy as mentioned previously. Murine DC 2.4 cells were transfected

with polymer/DNA complexes, which were formed with non-labeled polymer and Cy5-labeled luciferase DNA plasmid. The endosome/lysosome was visualized by introducing 100 nM of LysoTracker Green DND-26 (Invitrogen) to the cells 10 minutes prior to imaging. Ascorbic acid (5 μM) was used as the mounting media, in order to limit the affects of photobleaching since LysoTracker Green is used specifically in living cells. The LysoTracker Green fluorochrome was excited by a 488 nm emission wavelength and a 520 nm wavelength detected. All samples were maintained on ice until imaged, to slow any endosomal release of the polyplexes. Imaging limits (z-slices) were set to collect the top and bottom boarders of the cell at a step size of 0.4μm and 800 pixel resolution. A total of three images were collected for each experimental and control samples.

3.2.6. Endocytotic pathway inhibition and quantification

Filipin III (F4767, Sigma-Aldrich) was dissolved in DMSO to a final concentration of 10 μg/mL. Prior to use of Filipin III, cell viability was assessed by MTT in murine DC 2.4 showing that Filipin III has no cytotoxicity over a range of concentrations (0.0 to 5.0 μg/mL). Twenty-four hours prior to transfection, DC 2.4 cells were plated in a LabTek II 4-well chamber slide at a cell density of 100k per well in 1 mL of DC 2.4 complete cell culture media. Thirty minutes prior to transfection, the cell media was removed and replaced with DC 2.4 complete media containing Filipin III at final concentrations of 0.0, 0.75, and 1.5 μg/mL. Cell media was removed at the time of transfection and cells were washed once with dPBS and replaced with serum-free DC 2.4 media supplemented with Filipin III at final concentrations of 0.0, 0.75, and 1.5 μg/mL. Cells were transfected with polymer/DNA complexes formed using non-labeled polycationic polymers and Cy5-labeled luciferase DNA plasmid in the presence of Filipin

III and incubated at 37°C, 99% humidity, and 5% CO_2 for 4 hours. After 4 hours of incubation, the cell media was removed and the cells washed 2x with dPBS and replaced with DC 2.4 complete cell media containing Filipin III for an additional 20 hours. Thirty minutes prior to imaging, Hoechst 33342 blue nuclear stain was added to each chamber at a final concentration of 30 μM. After which, the media was removed and the samples were washed with PBS, and fixed according to the manufacturer's protocol using BD cytofix fixation buffer. The cells were then mounted with SlowFade Gold© anti-fade reagent mounting media and sealed with a glass cover slip and clear nail polish. Samples were imaged using the same method used for cellular uptake as described above. The concentration of Filipin III (0.0, 0.75, 1.5 μg/mL) for caveolae inhibition in murine DC 2.4 cells was optimized by quantifying the cellular uptake inhibition of Alexa Fluor 488 labeled cholera-toxin subunit B (CT-B) (Invitrogen) (Figure 4b) at concentrations ranging from 0.0 to 5.0 μg/mL by flow cytometry and confocal microscopy.

3.2.7. Quantification of confocal images

The method used for quantification of confocal images was adopted from a method developed by Akita et al. designed to calculate total pixel area. Confocal images were collected using an Olympus FV-1000 confocal microscope (Olympus) as described above per subcellular event. Post microscopy, confocal images were then imported and analyzed in ImageJ (National Institute of Health, Maryland) imaging software. Imported confocal images were opened in individual color components and converted to 8-bit images. Individual cells used for the analysis were then isolated from each image, eliminating cells that were damaged or dead. The cellular uptake of Cy5-labeled luciferase DNA plasmid for each cell was measured by individually thresholding each

cells z-slice and quantifying the total pixel area within a region of interest (ROI) drawn around the cell membrane.

Association of the polymer/DNA complex was quantified by measuring the degree of colocalization of the spatial overlap and the overlap between the Oregon Green-488 polymer and Cy5-luciferase DNA plasmid. Each complex component was thresholded individually for each z-slice. The total pixel area of the Cy5-luciferase DNA plasmid was calculated as well as the colocalization of the polymer/DNA, which was measured, by the ImageJ colocalization plug-in. The percentage of complex association was determined by dividing the colocalized total pixel area by the total Cy5-DNA pixel area; the same method was applied for determining the percentage of endosomal entrapment. Nuclear uptake was quantified by capturing the total pixel area of Cy5-luciferase DNA plasmid within a ROI of the nuclear membrane using the same method used for cellular uptake previously mentioned above. The geometry of nuclei was determined by stacking the z-slices into 3-D images and orthogonal views to verify DNA within the nuclei. Nuclear complex association was quantified using the same method as mentioned previously. A total number of 30 cells were analyzed for each experimental group based on the coefficient of variance[90]. No fluorescent enhancement was performed on any of the images prior to image quantification. Analysis of images was randomized by blinding the image quantifier to the polymer complex treatment.

3.2.8. Complex stability in serum-free media

Polymer polyplexes were prepared at an N/P ratio of 8:1 by adding 50 μL of polymer solution (0.1 μg/μL final concentration) to 50 μL of pEGFP-N1 DNA plasmid solution (0.08 μg/μL final concentration) in 20 mM HEPES buffer. The solution was

vortexed and allowed to incubate in the dark at room temperature for 30 minutes. Following incubation, the polyplexes were added to 2 mL of DC 2.4 serum-free media (Dulbecco modified Eagle medium low glucose supplemented with 1% penicillin/streptomycin, and 1% HEPES (1M)) warmed to 37° C. The baseline (0 hour) polymer complexes diameter size distribution was measured by dynamic light scattering using a 90plus dynamic light scattering particle analyzer (Brookhaven Instruments). The complexes were than placed into a 37° C incubator for 1 and 4 hours and particle size distribution measured. A total of three replicates were measured for each polymer at each time point. The data was analyzed by collecting the Gaussian (G(d)) and Cumulative (C(d)) distribution of each sample, and placed into bins (1-100 units) ranging from 100 to 10,000 nm. The data was plotted as Cumulative distribution versus particle diameter.

3.2.9. Circular dichroism of polycationic polymers

Polymer complexes were prepared at an N/P ratio of 8:1 at a final volume of 200 μL by adding 100 μL of the polymer solution (0.625 μg/μL final concentration) to 100 μL pEGFP-N1 DNA plasmid solution (0.25 μg/μL) in 20 mM HEPES. The complexes were then incubated at room temperature for 30 minutes prior to analysis. The secondary structure of the DNA plasmid was then measured using a J-815 Spectropolarimeter (JASCO, Easton, MD). The complex samples were run using 200 μL of solution at a wavelength range of 220 to 320 nm at a scanning speed of 50 nm/min at 25° C. A total of 5 accumulations were collected for each sample. Naked GFP-DNA plasmid and polymer only (each polymer) were run as positive and negative controls.

3.2.10. Transmission electron microscopy (TEM)

The size and morphology of $PAEM_{150}$, PLL_{150}, and PEI polymer/GFP DNA complexes at an N:P ratio of 8:1 incubated for 4 hours in serum-free media was observed using a JEOL 1200 EXII transmission electron microscope. TEM samples were prepared prior to imaging by first placing a droplet of the polymer/DNA complex onto a carbon-coated EM grid followed by negative staining by phosphotungstic acid (1.0%, pH 4-5).

3.2.11. Statistical analysis

Statistical analysis was carried out using a two-sample Student's t-test with unequal variance. Statistical significance was determined as a p-value, which was less than 5%.

3.3. Results and Discussion

3.3.1. Transfection efficiency of murine DC 2.4 cells

The design and development of polymeric vectors are critical for successful delivery of exogenous DNA for gene therapy or DNA vaccine applications. To date a vast number of polymer chemical designs have been employed with minimal knowledge as how these polymers interact within the cellular environment[96,121]. Therefore, the motivation of this current study is to understand the structural-functional relationship of polycationic polymers' chemical backbone structure with transfection efficiency by investigating the polymers' interaction with subcellular events in dendritic cells. This is most evident when comparing the transfection efficiency of polycationic polymers with similar chemical structures, where a variation in transfection efficiency between polymers is observed (Figure 3.1). The transfection efficiency of murine DC 2.4 cells was

tested using three different polycationic polymers: PEI, PAEM and PLL over a time course ranging from 30 minutes to 24 hours in order to assess the degree of transfection, and highlight the differences in transfection efficiency between polymer structure. Results showed that transfection for PEI and PAEM began primarily within the 4 hours of initial transfection of the polymer complexes and reached an optimal level of transfection by 12 to 24 hours (Figure 3.1B). PLL_{150} on the other hand, showed minimal improvement in transfection efficiency over the same range of time (Figure 3.1B). In terms of performance PEI and PAEM showed increased levels of GFP positive cells as well as mean fluorescence intensity (MFI) with increasing time (Figure 1b). Meanwhile PLL reported minimal increases in transfection efficiency in either GFP positive cells or MFI. These results were confirmed by fluorescent microscopy of GFP positive cells which showed PEI and $PAEM_{150}$ had high levels of GFP positive DC 2.4 cells after 24 hours; PLL showed similar levels of GFP fluorescence to that of the naked GFP-plasmid control (Figure 3.1).

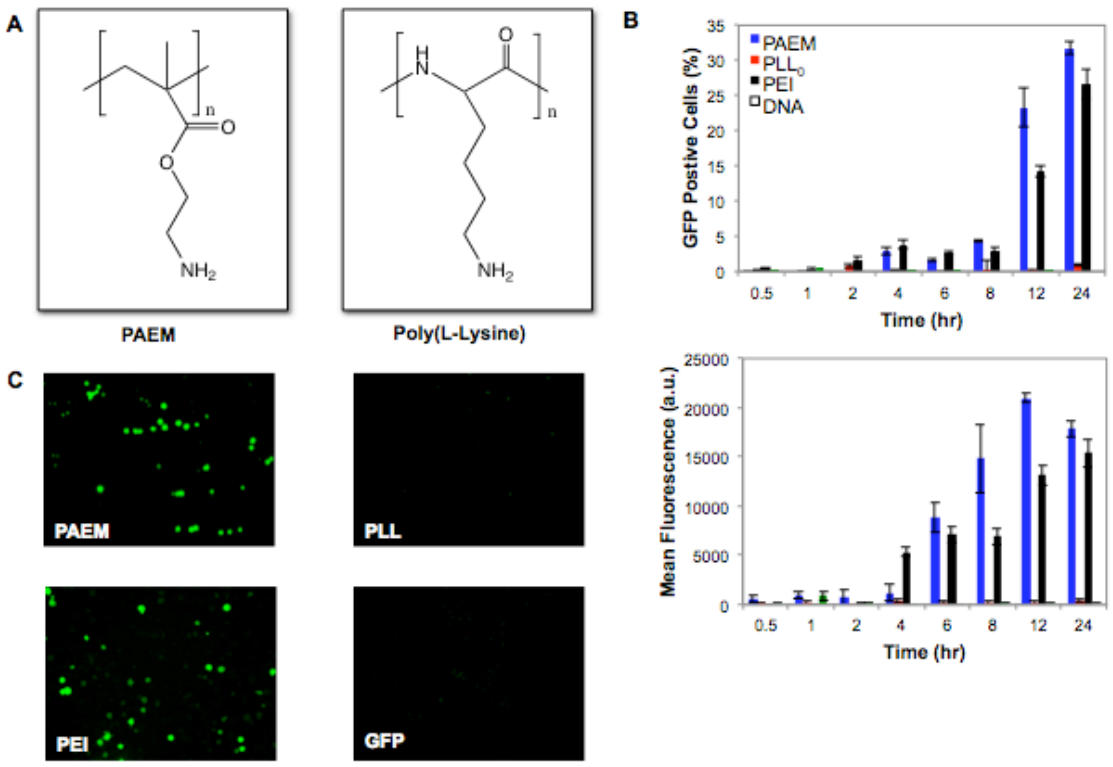

Figure 3.1. Transfection efficiency and subcellular trafficking quantification of PAEM, PLL and PEI polycationic polymers. (**a**) Chemical structure of PAEM, PLL, and PEI polycationic polymers. (**b**) Transfection efficiency time course of PAEM, PLL, PEI and naked GFP DNA plasmid in murine DC 2.4 dendritic cells showing percentage of GFP positive cells and mean fluorescence intensity (MFI) as measured by flow cytometry. (**c**) Fluorescence microscopy images of GFP positive murine DC 2.4 cells transfected with PEI, PAEM, PLL and naked GFP DNA plasmid. Transfection efficiency data is represented by the mean and standard deviation of three ($N = 3$) experimental replicates. Mean fluorescent intensity is depicted in arbitrary units (a.u.). Statistical analysis was performed using a Student's t-test, (* $p < 0.05$, ** $p < 0.01$, # $p < 0.001$).

A potential explanation for the variation in transfection efficiency amongst these polymer lies within the cellular interaction of the polymers with specific subcellular events such as cellular uptake, endosomal entrapment, and nuclear uptake[81]. To accurately convey a relationship between chemical backbone structures, we synthesized a linear polycationic PAEM polymer as well as PLL using living chain polymerization techniques to assure polymers with similar degrees of polymerization (150 repeat units) and narrow molecular weight distribution (Table 3.1).

3.3.2. Synthesis and characterization of PAEM and PLL polymers

The $PAEM_{150}$ and PLL_{150} were synthesized using living chain-polymerization techniques. $PAEM_{150}$ was synthesized using ATRP (Atom Transfer Radical Polymerization) and PLL_{150} by an open chain-polymerization, which allows for an average degree of polymer (DP) of 150 repeating units as well as providing a narrow molecular weight distribution (Table 3.1). Branched PEI was commercially purchased and possessed a similar molecular weight to that of $PAEM_{150}$ and PLL_{150}. All three polycationic polymers showed the ability of forming complexes with GFP-DNA plasmid at an N:P ratio of 8:1 as seen by dynamic light scattering (Table 3.1). DLS measurements showed that PLL_{150} possessed a smaller effective diameter than that of $PAEM_{150}$ and PEI. The zeta-potential of PLL_{150} was also slightly higher than that of both $PAEM_{150}$ and PEI, yet were still statistically similar (Table 3.1). The binding affinity (ethidium bromide assay) was higher in $PAEM_{150}$ and PLL_{150} shown by ethidium bromide quenching at an N/P ratio of 2:1, while ethidium bromide quenching of PEI did not occur until an N/P ratio of 4:1. The stability of $PAEM_{150}$ and PEI was higher than that of PLL_{150}, by requiring a heparin concentration of 0.6 and 0.7 IU/μg in order to dissociate the complex (Table 3.1). Of the three polymers, PEI possessed the lowest cell viability (92%) as determined by MTT assay.

Table 3.1. Polymer characterization.

Polymer	DP	Mn	PDI	Dynamic Light Scattering [a]		Ethidium Bromide Exclusion [b]	MTT Assay	Heparin Assay
				Particle Diameter (nm)	Zeta Potential (mV)	N/P Ratio of EB Quenching	Cell Viability (%)	Heparin (IU/μg)
PAEM	150	19,350	1.17	123.5 ± 1.5	35.1 ± 4.0	2	100	0.6
PLL	150	19,225	1.15	83.3 ± 2.3	41.8 ± 4.0	2	95	0.4
PAEM	100	10,047	1.2	103.1 ± 1.4	38.5 ± 10.6	2	98	0.4
$PAEM_{Am}$	100	10,511	1.11	68.7 ± 0.7	36.5 ± 8.2	2	98	0.0
PEI		10,000	2.5	113.8 ± 0.9	36.1 ± 2.8	4	92	0.7

[a] *Performed in 20mM HEPES buffer*

[b] *N/P ratio which decreases ethidium bromide fluorescence by ≥ 50%*

Data represents Mean and Standard Deviation

3.3.3. Polycationic polymer stability and DNA condensation

Recently it has been shown that particle size may be important to targeting and internalization of nanoparticles in dendritic cells[122]. Therefore, in order to understand if a difference in particle size is responsible for the variation among the transfection efficiency, the initial effective diameter of $PAEM_{150}$, $PAEM_{Am}$, PLL_{150}, and PEI was quantified by dynamic light scattering (Table 3.1) in 20 mM HEPES buffer. Interestingly, $PAEM_{150}$ as well as PEI exhibited similar effective diameters of approximately 114 to 125 nm, while PLL_{150} particles were smaller in diameter (83 nm) yet within statistical range of $PAEM_{150}$ and PEI. However, the effective diameter only portrayed the median particle diameter and did not include the polydispersity of the polymer/DNA complexes.

Therefore, polymer/DNA complexes were prepared in 20 mM HEPES buffer and visualized via transmission emission microscopy (TEM) to visualize the heterogeneity of the polymer complexes[123]. The TEM images show that both the $PAEM_{150}$ and PEI polymer/DNA complexes form a range of different sized round shaped particles, while PLL_{150} offers a number of different sized particle shapes, which include long/short linear rods and oval/round particles (Figure 3.2B). A potential reason for this particle formation

is that the PLL_{150} is causing the plasmid DNA to repeatedly bend and fold into linear rods[124]. Considering that the transfection occurred in the presence of serum-free media and not in 20 mM HEPES over a course of time. The polymer/DNA particle true particle size, as well as size distribution, was quantified using the complexes Gaussian and cumulative distributions in a more physiological relevant environment that used DC 2.4 serum-free media warmed to 37° C at 0, 1, and 4 hour time points (Table 3.2). Looking at the size distribution of $PAEM_{150}$, PLL_{150} and PEI, the baseline $PAEM_{150}$ data revealed a large mono-distributed population of 70% with an initial particle diameter of approximately 300 nm. At the same time point, PLL_{150} and PEI shared a similar mono-distribution of 81% and 100% respectively and an initial diameter of 200 nm. However, as time increased, nearly 50% of $PAEM_{150}$ and 88% of PEI were $\geq$ 400 nm, while 100% of PLL_{150} remained within 300 nm. After 4 hours, 50% of $PAEM_{150}$ and 47% of PEI were within the range of 400 to 800 nm, while only 29% of PLL_{150} ranged from 500 to 1200 nm; majority of the PLL_{150} population remained below the 500 nm threshold. The difference in size distribution for $PAEM_{150}$ and PEI may be a result of either polymer/DNA complex aggregation or destabilization of the complex itself. However, the resemblances of chemical structure between $PAEM_{150}$, PLL_{150} and PEI would suggest that all three polymers form complexes in a similar manner with similar complex stability.

Table 3.2. Cationic polymer size distribution in serum-free media.

Polymer	DP	0 hr		1 hr		4 hr	
		%	Diameter (nm)	%	Diameter (nm)	%	Diameter (nm)
PAEM	150	70	300	49	400	32	400
						32	≥ 500
PLL	150	81	200	100	300	23	500
						11	≥ 1000
PEI		100	200	88	400	21	400
						62	≥ 500

Performed in DC2.4 serum-free media at 37° C

The interaction of the polycationic polymer with the DNA plasmid can also be studied by evaluating the changes of the DNA structure by circular dichroism. Figure 3.2 shows the binding interaction of $PAEM_{150}$, PLL_{150}, and PEI with GFP-DNA plasmid. The naked GFP control showed a characteristic B-form profile with a negative peak at 244 nm and a maximum peak at 274 nm[125]. With the addition of PEI to the GFP plasmid the maximum positive peak experienced a red shift and a decrease in magnitude of the positive peak. This suggested that the GFP-plasmid underwent a conformational change from B-form structure into a C-form secondary structure[126]. The negative peak also underwent a change in magnitude while also undergoing a red shift affecting the helicity of the GFP plasmid[127]. With the addition of $PAEM_{150}$ and PLL_{150} we saw a greater red shift in the positive and negative peaks as well as being accompanied by a decrease in magnitude; showing that binding affinity of $PAEM_{150}$ and PLL_{150} was greater than that of PEI. The PAEM and PEI controls showed no positive reading for a secondary structure; however, PLL_{150} showed a positive peak at 220 nm due to being a polypeptide.

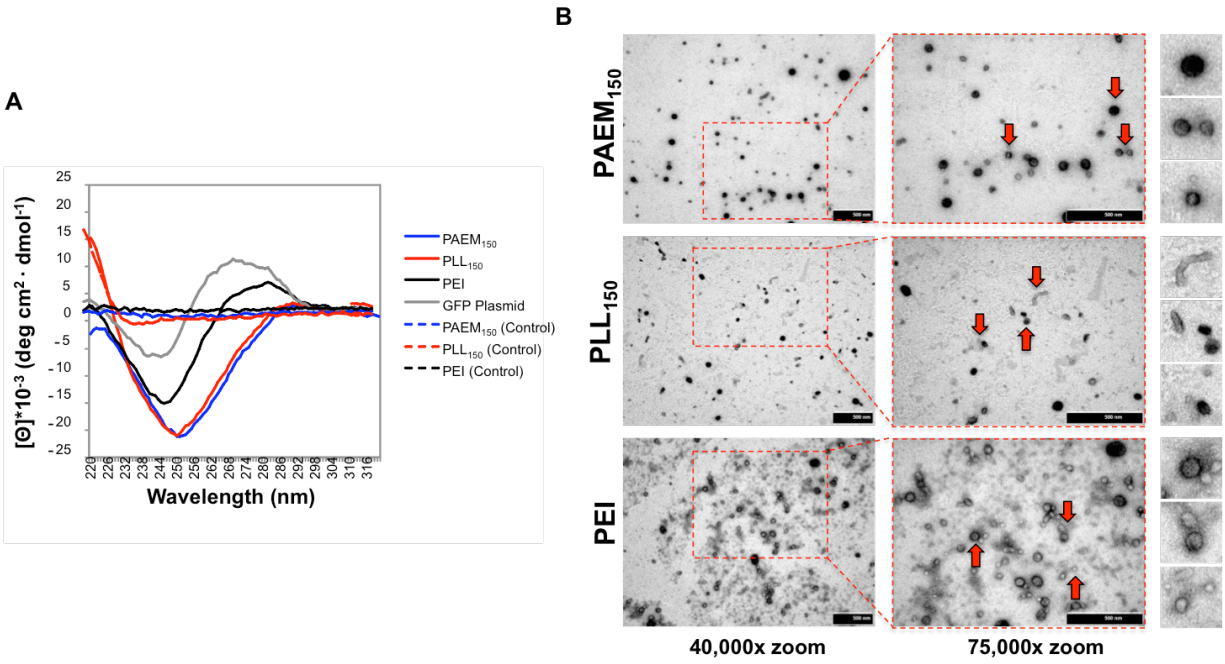

Figure 3.2. Complex stability and complexation studies. **(a)** Circular dichroism of $PAEM_{150}$, PLL_{150} and PEI. Configuration of DNA packing by complexation with cationic polymers. (**b**)TEM images of $PAEM_{150}$, PLL_{150}, and PEI. Samples were prepared in 20mM HEPES buffer solution using EGFP-plasmid DNA at an N/P ratio of 8:1 an incubated in serum-free media for 4 hours at 37° C. Red arrowheads depict the areas where individual zoomed in images were referenced.

3.3.4. Transfection efficiency $PAEM_{150}$ and PLL_{150}

A focused transfection efficiency study of $PAEM_{150}$, PLL_{150} and PEI at 24 hours using a GFP-DNA plasmid reporter gene was quantified by flow cytometry (Figure 3.3). The transfection efficiency was reported in the percentage of cells producing a green fluorescent signal as well as the intensity of the fluorescent signal. The percentage of GFP positive cells for $PAEM_{150}$ was significantly higher ($p < 0.01$) than PLL_{150} while maintaining a similar level of transfection efficiency to that of the PEI control (Figure 3.3). The mean fluorescence intensity data reflected a similar outcome to that of the percentage of GFP positive cells, with $PAEM_{150}$ reflecting comparable levels of MFI to that of PEI, while also being significantly higher than that of PLL_{150} (Figure 3.3).

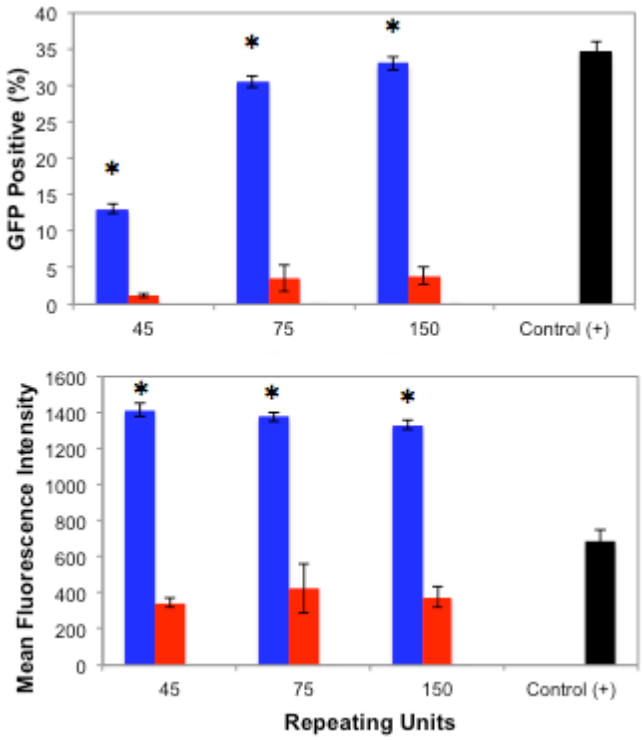

Figure 3.3. Transfection efficiency of $PAEM_{150}$, PLL_{150} and PEI polycationic polymers. Transfection efficiency of $PAEM_{150}$, PLL_{150}, and PEI in murine DC 2.4 dendritic cells showing percentage of GFP positive cells and mean fluorescence intensity (MFI) as measured by flow cytometry. Transfection efficiency data is represented by the mean and standard deviation of three ($N = 3$) experimental replicates. Mean fluorescent intensity is depicted in arbitrary units (a.u.). Statistical analysis was performed using a Student's t-test, (* $p < 0.05$, ** $p < 0.01$, # $p < 0.001$). Fluorescent intensity of individual fluorophores increased for representative images.

3.3.5. Subcellular trafficking of $PAEM_{150}$ and PLL_{150} in DC 2.4 cells

Initial reports have stated that the level of GFP expression can be correlated to the amount of cellular uptake in individual cells[128]. In order to determine whether the variation in transfection efficiency between $PAEM_{150}$ and PLL_{150} was due to differences in subcellular trafficking, the cellular uptake was visualized via confocal microscopy by utilizing a Cy5 luciferase-DNA plasmid complexed either to PEI, $PAEM_{150}$, or PLL_{150}. The confocal images were further analyzed using a method developed by Akita et al. to quantify the total pixel area of the Cy5-DNA cellular uptake within the cell membrane[90].

Quantification of the confocal images yielded that the cellular uptake for all three polymer complexes as well as naked DNA begins within the first hour of transfection with $PAEM_{150}$ exhibiting significantly higher cellular uptake at 1 ($p < 0.05$) and 4 ($p < 0.05$) hours. This may be attributed to the larger effective particle diameter of $PAEM_{150}$ (Table 3.1), which according to van der Aa et al. allows for faster sedimentation on the cell surface than smaller particles[129]. However, by 24-hours the level of cellular uptake for $PAEM_{150}$ was slightly higher than PLL_{150}, yet within statistical limits (Figure 3.4B). Cellular uptake of PEI also increased, but by 24-hours the amount of uptake was significantly less ($p < 0.05$) than that of either $PAEM_{150}$ or PLL_{150}.

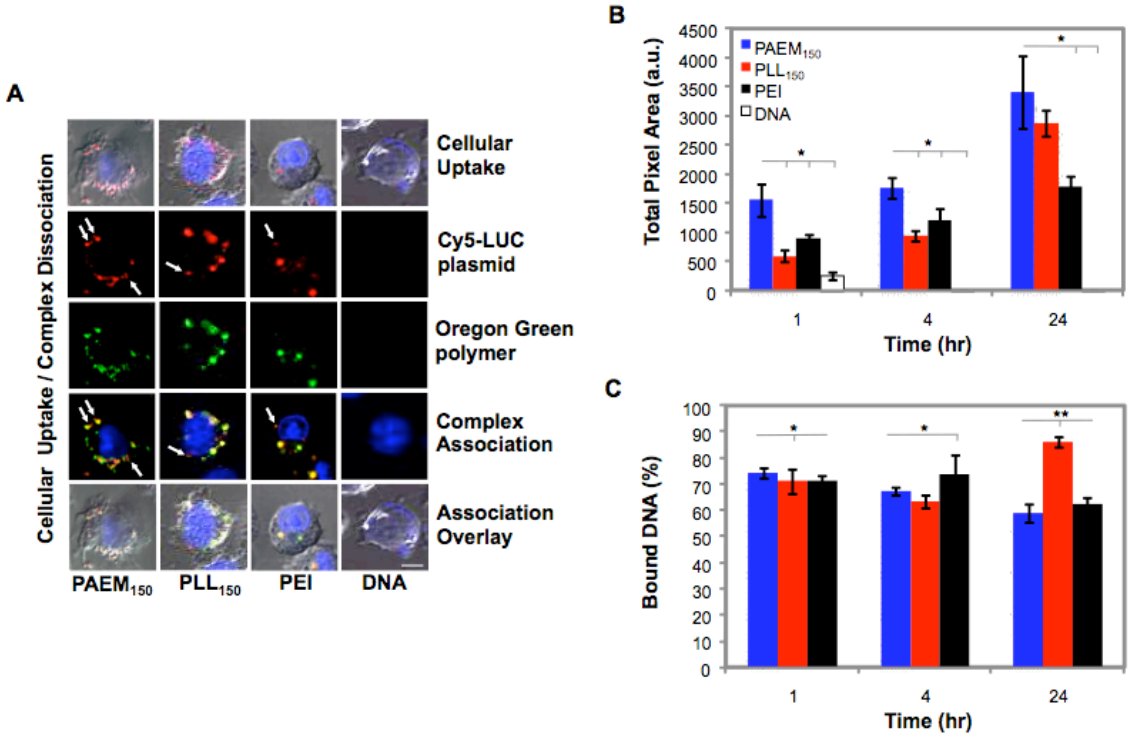

Figure 3.4. Subcellular trafficking quantification of $PAEM_{150}$, PLL_{150} and PEI polycationic polymers. (**a**) Fluorescence microscopy images of GFP positive murine DC 2.4 cells transfected with PEI, $PAEM_{150}$, PLL_{150} and naked GFP-DNA plasmid, white arrowheads represent unbound Cy5-DNA plasmid. (**b**) Quantification of confocal microscopy images measuring complex cellular uptake and (**c**) percentage of complex association Subcellular trafficking data is represented by mean and standard error of thirty ($N = 30$) randomly selected cells. Statistical analysis was performed using a Student's t-test, (* $p < 0.05$, ** $p < 0.01$, # $p < 0.001$). Fluorescent intensity of individual fluorophores was enhanced for representative images.

Once complexes are internalized into the cell the location and time of the complex dissociation is important to transfection efficiency[90]. The dissociation of the polymer complexes were visualized by the colocalization of the Cy5-DNA fluorescence with that of the Oregon Green-488 polymer. Confocal images revealed regions of unbound Cy5-DNA (white arrow head) for both the $PAEM_{150}$ and PEI polymers, while PLL_{150} high amounts of colocalization remained even after 24-hours (Figure 3.4C). The percentage of Cy5-DNA bound to either $PAEM_{150}$ or PEI decreased from 1 to 24-hours suggesting that the $PAEM_{150}$ and PEI complexes are dissociating within the cell over time. PLL_{150}, however, had vastly different results than $PAEM_{150}$; mostly the inability to dissociate even after 24-hours. The quantity of Cy5-DNA bound to PLL_{150} was similar to $PAEM_{150}$ and PEI after 1-hour, and by 4-hours the level of unbound Cy5-DNA decreased. But, by 24-hours, the percentage of bond DNA is significantly higher ($p < 0.01$) than PAEM150 (Figure 3.4C). The discrepancy between the complex dissociation is most likely due to the fact that the hydrophobicity of $PAEM_{150}$ is decreasing the electrostatic interaction between the $PAEM_{150}$ polymer and the DNA, therefore allowing the complexes to dissociated more easily[106]. However, this observation is contradicted by the fact that a higher concentration of heparin is needed to dissociate the $PAEM_{150}$ complexes (Table 1).

Previously, endo/lysosomal entrapment has been shown to be one of the primary subcellular barriers responsible for limiting transfection efficiency, due to the harsh acidic environment found within endo/lysosomal bodies[70]. As documented throughout the literature[46,66,130], the low transfection efficiency of PLL can be attributed to its inability to facilitate endosomal escape. Therefore, we visualized the colocalization of

the Cy5-DNA with endo/lysosomal bodies using LysoTracker Green DND-26 (Figure 3.5). After 24-hours, representative confocal images show free cytostolic Cy5-DNA plasmid (white arrow head) for both $PAEM_{150}$ and PEI, while PLL_{150} maintains elevated levels of Cy5-DNA plasmid colocalized with the fluorescently labeled endo/lysosomes. The absence of fluorescent signal for naked DNA suggests that by 24-hours the naked DNA is degraded (Figure 3.5B), which clarifies why the cellular uptake of naked DNA decreases with time as seen in Figure 3.5A. Quantification displays that endo/lysosomal entrapment occurs as soon as 1-hour post-transfection; $PAEM_{150}$ and PEI had significantly lower endo/lysosomal entrapment than that of PLL_{150} (Figure 3.5B). At 4-hours the amount of PLL_{150} and PEI complexes found within the endo/lysosome increased, while $PAEM_{150}$ decreased slightly. After 24-hours, 80% of the PLL_{150} complexes were still conferred within the endo/lysosome while nearly 50% of $PAEM_{150}$ and PEI complexes were colocalized within endo/lysosomes suggesting that the other 50% of the complexes may be within the cytosol. Our results confirmed these findings by showing that a large quantity of PLL_{150} complexes (60-80%) were found within the endo/lysosome between 1 to 24-hours (Figure 3.5B). The elevated level of endo/lysosomal entrapment of PLL_{150} might account for the high percentage of complex association, in that PLL_{150} begins to release the Cy5-DNA within the first 4 hours post-transfection. However, as time increases to 24-hours, the acidic endo/lysosomal environment degrades any unbound Cy5-DNA, thus leaving only associated PLL_{150} complexes (Figure 3.5B). The likelihood of PLL_{150} re-condensing the DNA plasmid is minimized by the high concentration of polyanions and anionic protein within the cell, which may shield the positive charge of the polymer[117]. The large quantity of PEI found

within the cytosol is easily explained since PEI has been documented as being able to induce endo/lysosomal release by buffering the endosomal pH via the proton sponge mechanism[46,51].

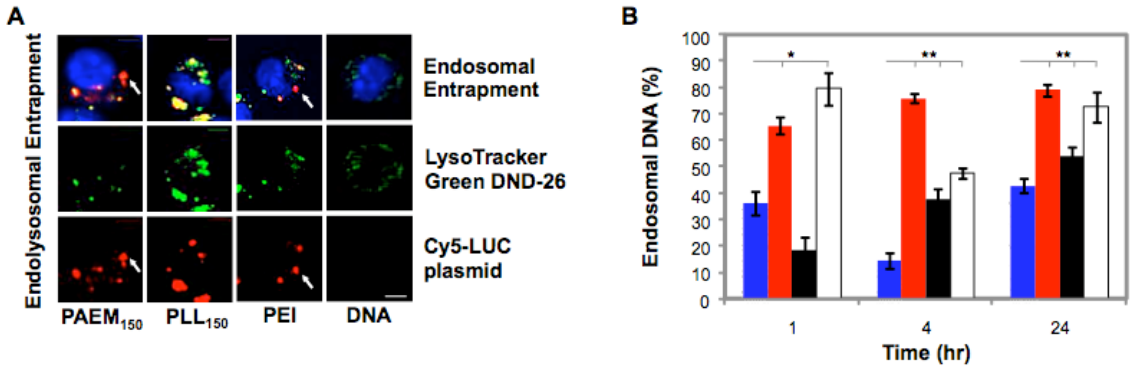

Figure 3.5. Subcellular trafficking quantification of $PAEM_{150}$, PLL_{150} and PEI polycationic polymers. (**a**) Fluorescence microscopy images of GFP positive murine DC 2.4 cells transfected with PEI, $PAEM_{150}$, PLL_{150} and naked GFP-DNA plasmid, white arrowheads represent unbound Cy5-DNA plasmid. (**b**) Quantification of complex endosomal entrapment in murine DC 2.4 cells at 1, 4, and 24 hours. (Subcellular trafficking data is represented by mean and standard error of thirty (N = 30) randomly selected cells. Statistical analysis was performed using a Student's t-test, (* $p < 0.05$, ** $p < 0.01$, # $p < 0.001$). Fluorescent intensity of individual fluorophores was enhanced for representative images

The final subcellular barrier and main target for the polymer/DNA complex is nuclear uptake of the DNA plasmid as well as complex dissociation[117,131]. Therefore, the amount of total and unbound Cy5-DNA delivered into the cell nucleus was quantified for each polymer (Figure 3.6). The representative images depict that by 24-hours, a small amount of Cy5-DNA can be seen within the cell nuclei with the $PAEM_{150}$ and PEI polymers (Figure 3.6A). Conversely, neither PLL_{150} nor naked DNA shows colocalization of plasmid DNA with the nuclei after 24-hours. Quantification of the confocal images verified that the highest degree of nuclear uptake belongs to $PAEM_{150}$ (Figure 3.6B), with nuclear uptake occurring as early as 1-hour post transfection. The bulk of nuclear transfection for PEI and PLL_{150} was not seen until 24-hours, at which time the level of nuclear uptake of $PAEM_{150}$ and PEI was significantly higher ($p < 0.05$) than that of PLL_{150} and naked DNA. Taking into account complex dissociation, the

amount of unbound Cy5-DNA was also quantified, which shows that despite $PAEM_{150}$ ability to traffic to the nucleus within the first hour of transfection the amount of unbound Cy5-DNA was extremely low. The Cy5-DNA does not dissociated from $PAEM_{150}$ until sometime after 1 hour (Figure 3.6B), where a small amount of unbound Cy5-DNA can be seen by 4-hours. Through 24-hours, the level of unbound Cy5-DNA within the cell nuclei increased, with $PAEM_{150}$ and PEI accounting for significantly higher amounts than that of PLL_{150} (Figure 3.6). $PAEM_{150}$ and PEI ability to traffic large quantities of Cy5-DNA into the cytosol as well as the cell nucleus, coupled with PLL_{150} poor endosomal escape and nuclear uptake accounts for the differences seen in the transfection efficiency for each polymer (Figure 3.3). Farrell et al. arrived at similar results with PLL and PEI, exhibiting similar cellular uptake in bone marrow-derived stromal cells. Yet, the rate-limiting step resided in the fact that PEI was more efficient intracellularly than PLL.

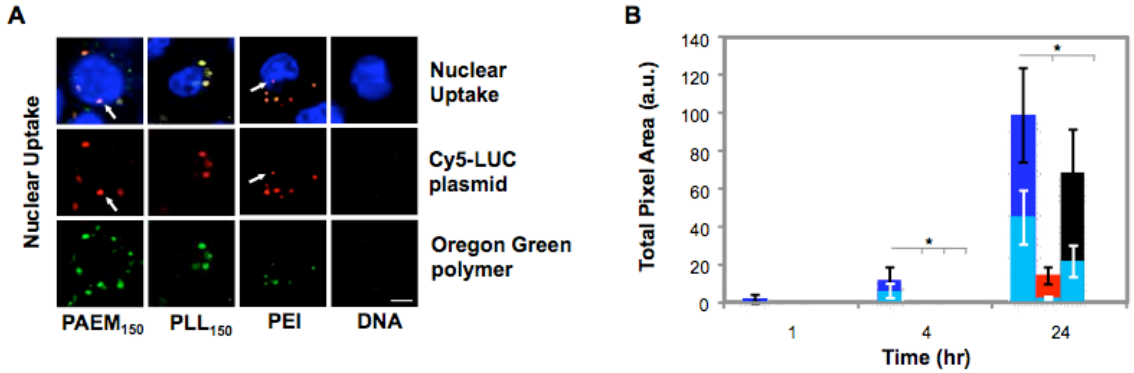

Figure 3.6. Subcellular trafficking quantification of $PAEM_{150}$, PLL_{150} and PEI polycationic polymers. (**A**) Fluorescence microscopy images of GFP positive murine DC 2.4 cells transfected with PEI, $PAEM_{150}$, PLL_{150} and naked GFP-DNA plasmid, white arrowheads represent unbound Cy5-DNA plasmid as well as Cy5-DNA trafficked into the nucleus.. (**f**) Quantification of confocal images, showing Cy5 labeled luciferase DNA plasmid in DC 2.4 cell nuclei. The graphs show the total amount and unbound (light blue) Cy5-DNA plasmid taken up into the nucleus. Subcellular trafficking data is represented by mean and standard error of thirty (N = 30) randomly selected cells. Statistical analysis was performed using a Student's t-test, (* $p < 0.05$, ** $p < 0.01$, # $p < 0.001$). Fluorescent intensity of individual fluorophores was enhanced for representative images.

3.3.6. Synthesis and characterization of $PAEM_{Am}$ and $PAEM_{100}$

Despite, the high transfection efficiency and nuclear uptake of $PAEM_{150}$, an interestingly anomaly still remains, which is $PAEM_{150}$ ability to escape endo/lysosomal bodies, despite having a similar chemical structure to that of PLL_{150}, which we have seen is highly contained with in the endo/lysosome. Much like PLL_{150}, $PAEM_{150}$ only possesses primary amines on its side chain, which lack the buffering capacity needed to facilitate the "proton sponge" mechanism seen with PEI at an acidic endosomal pH[132]. The lack of buffering capability of $PAEM_{150}$ suggested that $PAEM_{150}$ might somehow disrupt the endosomal membrane. Therefore, we hypothesized that the ester group found within the $PAEM_{150}$ side chain was cleaved within the endo/lysosome by esterase, thus forming poly(methyl acrylate) acid (PMAA) with a carboxylic acid group on the side chain which has been shown to promote lysosomal destabilization[133]. Therefore, we synthesized a new poly(*2-aminoethyl methacrylate amine*) ($PAEM_{Am}$) possessing an amide group in place of the ester group found within the $PAEM_{150}$ side chain. $PAEM_{Am}$ and $PAEM_{100}$ polycationic polymers was synthesized by RAFT (reversible addition-fragmentation chain transfer) polymerization, resulting in polymers with an average DP of 100 repeating units and similar molecular weight (Table 3.1). $PAEM_{Am}$ is a linear polymers; possessing a primary amine located on the polymer side chain (Figure 3.7). Despite the slight difference in side chain structure, $PAEM_{Am}$ complexes display similar charge potential (zeta-potential), binding affinity (ethidium bromide) and cell viability (MTT-Assay) as that of $PAEM_{100}$ (Table 3.1). However, $PAEM_{Am}$ differs from $PAEM_{100}$ by forming complexes with smaller effective diameters as well as having less complex stability when introduced to low concentrations of heparin (Table 3.1). However, the

$PAEM_{Am}$ complex was shown to be less stable than its $PAEM_{100}$ counterpart by heparin exclusion assay, where the $PAEM_{Am}$ complex was unstablized by the high concentration of ionic salts in the 150 mM NaCl vehicle solution (0.0 IU/μg) (Table 3.1)[104].

3.3.7. Transfection efficiency of $PAEM_{Am}$ and $PAEM_{100}$

GFP DNA plasmid was complexed with either $PAEM_{Am}$ or $PAEM_{100}$ and incubated with murine DC 2.4 cells. The transfection efficiency of $PAEM_{Am}$ and $PAEM_{100}$ was determined by quantification of the percentage of GFP positive cells, as well as the proteins' mean fluorescence intensity via flow cytometry after 24-hours. The overall mean percentage of GFP positive cells for $PAEM_{Am}$ was lower than that of $PAEM_{100}$ and PEI however; due to the high variation within the $PAEM_{Am}$ group the difference is statistically irrelevant (Figure 3.7B). Interestingly, despite having a lower percentage of GFP positive cells, the level of mean fluorescence intensity for $PAEM_{Am}$ is comparable to that of either $PAEM_{100}$ or PEI.

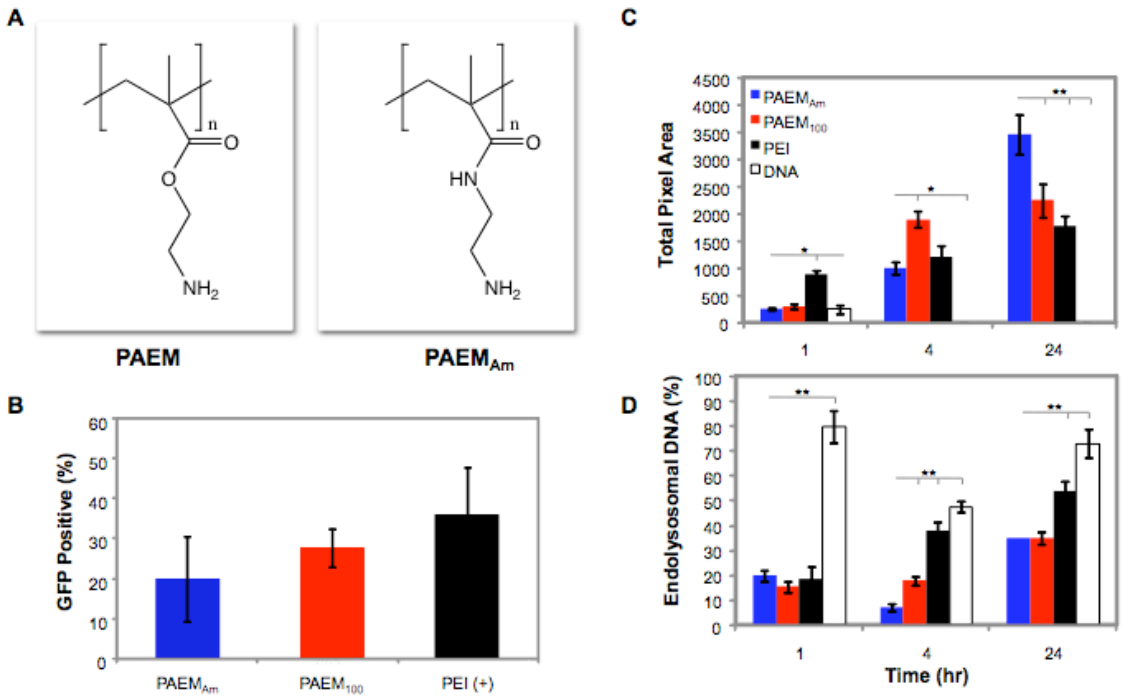

Figure 3.7. Affect of PAEM side chain modification of transfection efficiency and subcellular trafficking. (**a**) Chemical structure of $PAEM_{Am}$ polycationic polymer. (**b**) Transfection efficiency of $PAEM_{Am}$, $PAEM_{100}$, and PEI depicting the percentage of GFP positive cells as well as mean fluorescence intensity in murine DC 2.4 cells after 24-hours. (**c**) Quantification of confocal microscopy images measuring complex cellular uptake and (d) endolysosomal entrapment after 1, 4, and 24-hours. (Transfection efficiency data is represented by the mean and standard deviation of three ($N = 3$) experimental replicates. Mean fluorescent intensity is depicted in arbitrary units (a.u.). Subcellular trafficking data is represented by mean and standard error of thirty ($N = 30$) randomly selected cells. Statistical analysis was performed using a Student's t-test, (* $p < 0.05$, ** $p < 0.01$, # $p < 0.001$).

3.3.8. Subcellular trafficking of $PAEM_{Am}$ and $PAEM_{100}$

After 24-hours, representative cellular uptake images for Cy5-DNA complexed with either $PAEM_{Am}$ or $PAEM_{100}$ show a higher amount of Cy5-DNA taken up into the cell for $PAEM_{Am}$ than that of $PAEM_{100}$ (Figure 3.7C,D). Quantification of these images verifies that by 24-hours, $PAEM_{Am}$ has a significantly higher ($p < 0.01$) level of cellular uptake compared to its $PAEM_{100}$ counterpart (Figure 3C). Interestingly, prior to 24-hours the cellular uptake of $PAEM_{Am}$ is significantly lower ($p < 0.05$) than $PAEM_{100}$; specifically at 4-hours, where as at 1-hour both $PAEM_{Am}$ and $PAEM_{100}$ exhibit

significantly lower ($p < 0.05$) levels of cellular uptake compared to the PEI control. The extent of complex dissociation for $PAEM_{Am}$ appears to be similar to that of $PAEM_{100}$ from the confocal images and colocalization quantification (data not shown). At the initial time point of 1-hour, all three polymers again show similar levels of complex association (~70%). By 24-hours, the amount of associated $PAEM_{Am}$ complexes decreased by a similar amount to PEI (14%) and $PAEM_{100}$ (9%).

Colocalization of Cy5-DNA with fluorescently labeled endosomes was minimal for $PAEM_{Am}$ and $PAEM_{100}$ complexes after 24 hours (Figure 3.7C). Quantification of the images verified that $PAEM_{Am}$ and $PAEM_{100}$ exhibit lower levels of endosomal entrapment than PEI at 4 and 24-hours, after displaying similar amounts of endosomal entrapment at 1 hour (Figure 3.7C). By 24-hours, more than 60% of the $PAEM_{Am}$ and $PAEM_{100}$ complexes are outside of the endosome. Confocal images for $PAEM_{Am}$ and $PAEM_{100}$, verified that both polymers allow for trafficking of Cy5-DNA into the cell nucleus (Figure 3.7D). Unlike $PAEM_{150}$, the initial nuclear uptake for both polymers occurs within 4-hours of transfection and increases by 24-hours with the total amount of nuclear uptake for $PAEM_{100}$ being slightly higher (Figure 3.7D). The total amount of unbound nuclear DNA follows the same trend as the total nuclear uptake, where both $PAEM_{Am}$ and $PAEM_{100}$ show initial nuclear uptake to occur within 4-hours and increase by 24-hours; however, $PAEM_{Am}$ displays higher levels of unbound nuclear DNA (Figure 3.7D). The modification of the PAEM side chain shows limited effect on the transfection efficiency or subcellular events, more importantly endo/lysosomal entrapment, suggesting that PAEM polymer/DNA complexes might be utilizing different endocytotic pathways than other polycationic polymers.

3.3.9. Endocytotic pathway

A number of reports have focused on the mechanism of endocytotic uptake of non-viral vectors as an explanation to the difference in transfection efficiency[73,88,118,129,134-138]. Two of the most widely researched endocytotic pathways have been the clathrin-mediated and caveolae/lipid raft dependent pathways[135,136,139-141]. Caveolae/lipid raft dependent endocytosis has been described as an ideal pathway for use in DNA vaccines since it bypasses the endosome[73]. However, according to von Gersdorff et al. caveolae/lipid rafts are cell type specific and an extensive literature search yielded no evidence of whether or not murine DC 2.4 cells contain caveolae[134]. Therefore, cholera toxin subunit B (CT-B) was used to determine if caveolae/lipid raft dependent endocytosis was present in murine DC 2.4 since CT-B has been shown to traffic into cells primarily via caveolae/lipid raft mediated endocytosis[129,142]. Since, lipid rafts are primarily composed of sphingolipids, cholesterol, and specific proteins the caveolae/lipid raft dependent endocytosis was inhibited by means of Filipin III a cholesterol-binding reagent[134,143]. In order to verify that the Filipin III presence and inhibition of caveolae in murine DC 2.4 cells, FITC labeled cholera subunit toxin-B (CT-B) was used, since it has been known to be taken up into cells primarily through the caveolae/lipid raft-mediated pathway[129,142]. It is noteworthy to point out that the cytotoxicity of Filipin III on DC 2.4 showed little to no cytotoxicity at concentrations from 0.0 to 5.0 μg/mL by MTT-assay (data not shown). The inhibition concentration range was determined via flow cytometry by quantifying the decrease in cellular uptake of the CT-B with increasing Filipin III concentration (Figure 3.8A). To verify the inhibition of CT-B into DC 2.4 cells confocal images show that at low concentrations of

inhibitor (0.0 µg/mL) CT-B was actively taken up into cells (Figure 3.8B). However, as the concentration of Filipin III was increased the quantity of CT-B taken up into the cell cytoplasm was decreased eventually to a point where cellular uptake of CT-B was inhibited and contained exclusively on the exterior of the cell membrane (Figure 3.8A). This clarifies why the flow cytometry data shows positive cellular uptake of CT-B at higher concentrations of Filipin III (Figure 3.8B).

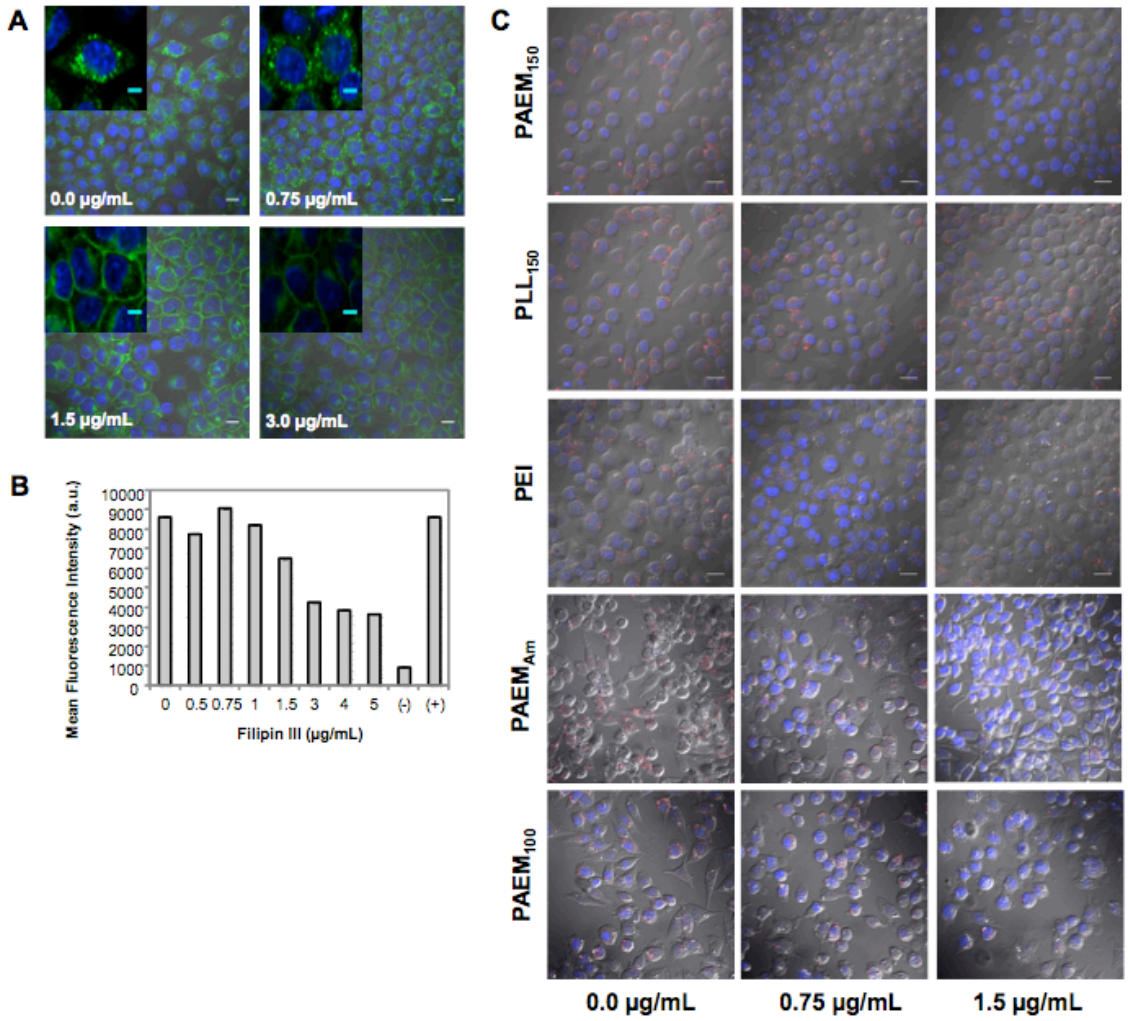

Figure 3.8. Endocytotic pathway inhibition of murine DC 2.4 cells. (**a**) Inhibition of the caveolae endocytotic pathway was confirmed using cholera toxin subunit B (CT-B) with increasing concentration of Filipin III. (**b**) Quantification of CT-B cellular uptake inhibition with increasing Filipin III concentration by flow cytometry. (**c**) Representative confocal images of the effect of Filipin III on cellular uptake after 24 hours for $PAEM_{150}$, PLL_{150}, PEI, and $PAEM_{Am}$. (CT-B flow cytometry data is represented by the mean and standard deviation of three ($N = 3$) experimental replicates. Mean fluorescent intensity is depicted in arbitrary units (a.u.). Statistical analysis was performed using a Student's t-test, (* $p < 0.05$, ** $p < 0.01$, # $p < 0.001$)

To verify if any of the cationic polymers were dependent on the caveolae/lipid raft dependent pathway, the transfection efficiency of pretreated DC 2.4 cells transfected with cationic polymers complexed with GFP-plasmid DNA was measured by flow cytometry after 24-hours (Figure 3.9C). Interestingly, of the three cationic polymers only $PAEM_{150}$ and PEI showed a decrease in the percentage of GFP positive cells with increasing Filipin III concentration, while PLL_{150} remained unchanged (Figure 3.9C), suggesting that $PAEM_{150}$ and PEI transfection may be dependent on caveolae-mediated endocytosis.

To understand how the Filipin III was inhibiting the transfection efficiency, confocal images were taken of murine DC 2.4 cells treated prior to transfection with Filipin III and transfected with $PAEM_{150}$, PLL_{150}, or PEI complexed with Cy5 labeled luciferase-DNA plasmid (Figure 3.8C). Initial representative confocal images demonstrated that at an initial Filipin III concentration of 0.0 μg/mL all of the polymer complexes shared similar normalized levels of cellular uptake. With increasing Filipin III concentration, the quantity of Cy5-DNA taken up into the cell decreases for all PAEM polymers as well as PEI, while the level of cellular uptake for PLL_{150} remained continuous. Quantification of the confocal images (Figure 3.9A) confirmed that increasing concentrations of Filipin III significantly decreased the level of cellular uptake of $PAEM_{150}$ by 54% (0.75 μg/mL) and 69% (1.5 μg/mL), while at the same concentrations PLL_{150} revealed no significant difference in cellular uptake. Use of Filipin III also inhibited the uptake of PEI, limiting cellular uptake by up to 38% at a concentration of 1.5 μg/mL (Figure 3.9A). A recent literature search verified these results, where a complete repression of PEI transfection efficiency was seen in HeLa

cells[137], as well as partial inhibition in A549 cells treated with Filipin III[135]. Quantification of the nuclear uptake of the Cy5 labeled luciferase-DNA plasmid showed that the amount of $PAEM_{150}$ and PEI complex DNA within the nuclear envelope is significantly decreased as a result of increasing Filipin III concentration. The effect of Filipin III on PLL_{150} was minimal, since the amount of DNA within the nucleus remained relatively unchanged, suggesting no dependence on the caveolae-mediated pathway by maintaining a constant transfection; leading that PLL_{150} traffic into the DC 2.4 cells primarily through a non-caveolae mediated pathway. The inhibition of the PAEM and PEI polymers transfection efficiency, cellular uptake and nuclear trafficking as well as CT-B by the administration of Filipin III demonstrates that these vectors may be taken up into murine DC 2.4 cells primarily by caveolae/lipid raft dependent endocytosis. Despite trafficking into the cell via caveolae/lipid rafts, the percentage of PAEM and PEI complexes trapped with the endosome still increases from 1 to 24 hours (Figure 3.5); this is most likely to due to the fact that caveolae-mediated endocytosis has the potential to traffic to the either the endoplasmic reticulum or the early endosome[141,144].

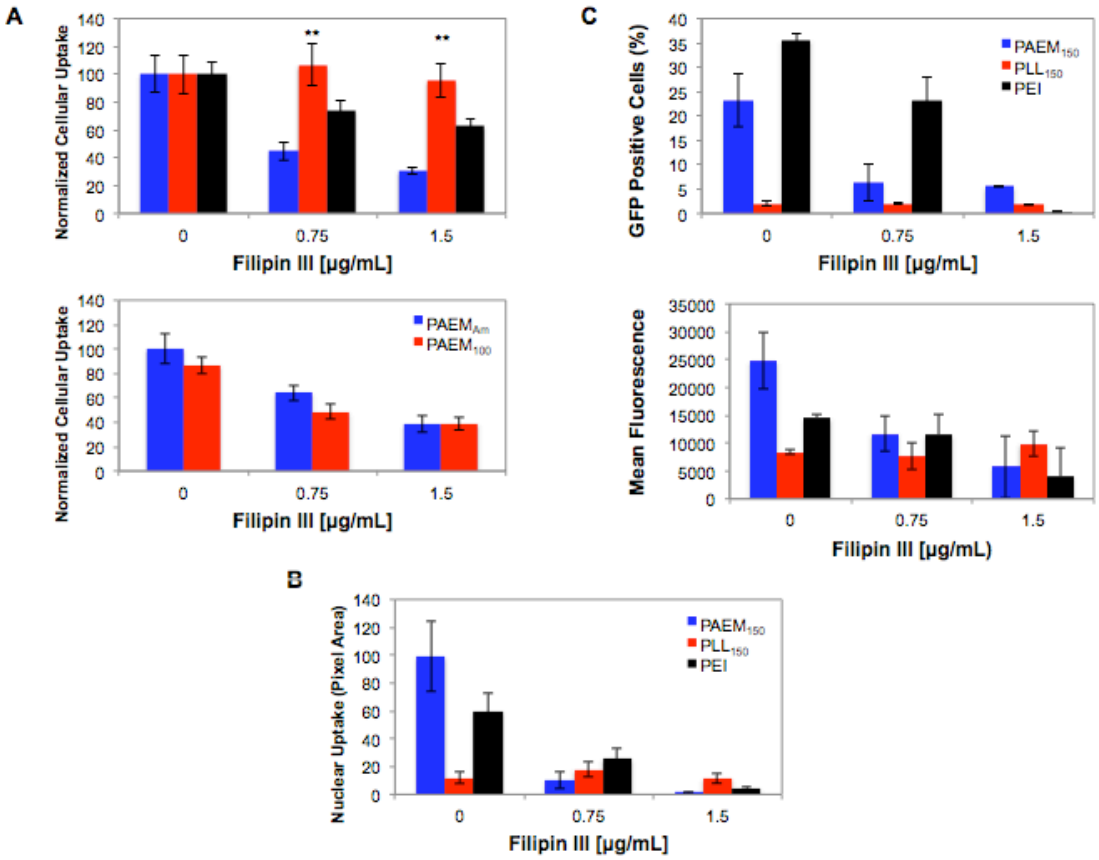

Figure 3.9. Endocytotic pathway inhibition of murine DC 2.4 cells. (**a)** Quantification of confocal images showing the inhibition of cellular uptake for $PAEM_{150}$, PLL_{150}, PEI and $PAEM_{Am}$ polymers. (**b)** Filipin III inhibition of nuclear uptake. **(c)** Effect of Filipin III on the transfection efficiency of $PAEM_{150}$ and PLL_{150}**.** Flow cytometry data is represented by the mean and standard deviation of three (N = 3) experimental replicates. Mean fluorescent intensity is depicted in arbitrary units (a.u.). Subcellular trafficking data is represented by mean and standard error of thirty (N = 30) randomly selected cells. Statistical analysis was performed using a Student's t-test, (* $p < 0.05$, ** $p < 0.01$, # $p < 0.001$).

The difference in endocytotic pathways between $PAEM_{150}$ and PLL_{150} can be largely attributed to differences in their physiochemical properties such as surface charge, hydrophobicity, shape, and particle size[70,72]. A number of studies have shown that differences in cationic polymer hydrophobicity can drive increased cellular uptake, by promoting stronger binding of the polymer/DNA complex to the hydrophobic portion of the cell plasma membrane such as lipid rafts, which might play a role in the endocytotic route taken by the complexes[121,145]. A simple examination of the cationic backbone of

each polymer revealed that the high quantity of hydrocarbons along $PAEM_{150}$ creates a more hydrophobic structure compared to the amine containing structure of PLL_{150}.

Another possibility is the effect of complex size and shape on cellular uptake. In a study looking at the particle size of PEI polymer/DNA complexes, Ogris and co-workers reported that PEI particles ranging from 500 and greater were more efficient in gene expression compared to smaller particles[146]. These findings were confirmed by Rejman et al. using fluorescently labeled latex beads with varying diameters, which revealed that microspheres with a diameter of approximately 200 nm was primarily internalized via the clathrin-mediated pathway, while microspheres with an approximate diameter of 500 nm were trafficked into the cells via the caveolae-mediated pathway[75]. TEM microscopy images show that $PAEM_{150}$ and PEI complexes remain circular in shape however PLL_{150} possess three distinct shapes (Figure 3.2), it is this shape of the complex with might dictate which endocytotic pathway the complex utilizes[147]. Despite this evidence, unfortunately, the question still remains as to what molecular characteristic of these polymer/DNA complexes might effect the endocytotic internalization whether it is the hydrophobicity, complex size, or another unrevealed characteristic, since we do not have concrete evidence suggesting that any one of these or all of these attributes are responsible for the differences in transfection between these polymers.

3.4. Conclusions

In this study we were able to quantify the fluorescent colocalization between fluorescently-labeled DNA plasmid, polymer, and cellular organelles from confocal microscopy images according to a method developed by previously Akita et al. We were able to conclude from the quantification that endosomal entrapment is the overall main subcellular barrier limiting the transfection efficiency of PLL_{150}, by limiting complex dissociation and preventing nuclear translocation. From this work we were also able to conclude that differences in the polymer backbone structure may account for variations in the complex hydrophobicity, stability, size and shape, which may allow complexes of specific diameters to traffic into the DC 2.4 cell via caveolae/lipid raft dependent endocytosis, therefore bypassing endo/lysosomal entrapment. This work may be beneficial to improving the transfection efficiency of future DNA vaccine systems, by highlighting the importance of polymer backbone structure in optimizing a polycationic polymer vector, which can target specific endocytotic pathways.

Chapter 4: Effect of Dendritic Cell Type and Maturation on Transfection Efficiency of Synthetic Polymer Gene Carriers

4.1. Introduction

Dendritic cells (DCs) are viewed to many as the most efficient antigen-presenting cell for their ability to orchestrate both a cell-mediated and humoral immune response[11,12,13,18,25]. Immature DCs have the specific function of capturing and processing antigens or proteins found within peripheral tissue[16], into smaller fragments which can then be presented on the dendritic cell surface via the major histocompatibility complex (MHC) molecules[23,24]. Maturation of DCs leads to migration from the peripheral tissue to the draining lymph nodes, and to phenotypical changes such as loss endocytotic and phagocytotic uptake, and up-regulations of co-stimulatory molecules CD40, CD80, and CD86[15]. Upon arrival into the lymph system, T-cells (CD4+ and CD8+) are activated by the coupling of the antigen-activated MHC complexes on the DCs with the T-cell antigen receptor (TCRs), initiating T-cell proliferation and differentiation[15,20,24]. The activated T-cell then activates a humoral immune response by initiating proliferation and maturation of immature B-cells. Therefore, an effective DNA vaccination against cancer and infectious disease requires properly designed molecular delivery vehicles that target antigen-presenting cells and successfully protects the exogenous DNA. Despite the attempt to harness the potential potency of DC-based DNA vaccines, the ability to produce robust transfection in DCs *in-vitro* is still limited[116].

In hopes of improving transfection, a large number of nonviral gene-delivery polymers with diverse chemical structure and property have been reported[96]. Yet, there is a lack of understanding of the interactions between nanoparticulate polyplexes and

antigen-presenting dendritic cells. More specifically, the transfection efficiency of polyplexes has been shown to be dependent on cell type[134]. Boussif et al. designed a study that measured the transfection efficiency of PEI across 25 different cell-types, which yielded significantly different levels of transfection efficiencies for multiple cell lines depending on the cell type. Similarly, Intra et al. showed that branched PEI had significantly different gene expression activity in HEK293, COS-7, HepG2, and HeLa cells *in-vitro*. Therefore, the interaction of specific polycationic polymers within one dendritic cell type may not correspond to other dendritic cell lines or subtypes. Furthermore, while the phenotypical maturation of DCs is critical in the generation of antigen-specific immunity, the effect of maturation state of DCs on polymer-mediated gene transfection efficiency is limited. More specifically, the state of maturation has been known to affect subcellular trafficking by slowing cellular uptake[150].

Here, we examined two cationic polymers with well-defined chain-length and narrow molecular weight distribution; namely, poly(2-aminoethyl methacrylate) (PAEM)[110], and poly(L-lysine) (PLL), via controlled polymerization methods. These polymers were used to transfect two distinct types of murine DCs: an immortalized cell line (DC 2.4), which was previously transfected with a retrovirus and independent of granulocyte macrophage colony stimulating factor (GM-CSF); and immature bone marrow-derived primary DCs (BMDC), and the relationship between DC maturation state and transfection was investigated.

4.2. Experimental Materials and Methods

4.2.1. Bone marrow-dendritic cell isolation

Murine bone marrow-derived dendritic cells were harvested from 20-week-old male C57Bl/6 mice according to a method published previously[148]. Mice were euthanized using $C0_2$ inhalation in accordance with University of Minnesota Institutional Animal Care and Use Committee. After which, the left and right femurs and tibia were removed from the mouse and washed with PBS and 70% ethanol for 1 minute. The bones were then washed and placed in warm RPMI 1640 media. Both ends of the femur and tibia were cut off and the bone marrow was flushed out into a 50mL conical tube by pushing 10mL of RMPI 1640 through the bone with a 25-gauge needle attached to a 10cc syringe. The cells were then purified by passing the cell solution through a cell strainer and spun down in a centrifuge. Red blood cells were lysed using Ack lysing buffer and incubated in a 37° C water bath for 5 minutes. The cells were washed with RMPI 1640 media and spun down. The cells were suspended in complete 10% serum containing media (RPMI 1640, 10% fetal bovine serum, 1% sodium pyruvate, 1% penicilin/streptomycin, 1% L-glutamine, 1% HEPES) supplemented with 3% GM-CSF and 1μL/mL of 2-ME and plated in a 6-well plate (Corning) at a cell density of 5 million cells/3mL. The cell media was changed every second day and supplemented with GM-CSF and 2-ME for a total of 6 days. After 6 days the cells were trypsinized and plated according to the experimental protocols shown below.

4.2.2. Dendritic cell transfection efficiency

Murine dendritic cells were cultured in complete cell culture media DC 2.4 media (Dulbecco modified Eagle medium low glucose supplemented with 10% fetal bovine

serum, 1% penicillin/streptomycin, and 1% HEPES (1M); Invitrogen, Carlsbad, CA) or BMDC complete media and maintained at 37°C, 99% humidity, and 5% CO_2. For transfection efficiency studies, cells were plated in a 12-well cell culture plate (Corning, Corning, NY) at a cell density of 100,000 cells per well, 24 hours prior to transfection. Prior to transfection, the cell media was removed and the cells were washed once with PBS (Dulbecco phosphate buffer solution, pH 7.4; Invitrogen, Calsbad, CA), and replaced with complete serum-free DC 2.4 media (Dulbecco modified Eagle medium low glucose supplemented with 1% penicillin/streptomycin, and 1% HEPES (1M)) or BMDC media (RPMI 1640 media supplemented 1% penicillin/stretpmycin, 1% sodium pyruvate, 1% HEPES). Cells were then transfected with polymer/DNA complexes at an N:P ratio of 8:1 containing 2 μg of GFP DNA plasmid (Elim Biopharmeceutics) and incubated at 37°C, 99% humidity, and 5% CO_2 for 4 hours, after which the cell media was removed and the cells were washed 2x with PBS and replaced with complete media containing 10% serum and allowed to incubate for an additional 20 hours at 37°C, 99% humidity, and 5% CO2. After the 24 hour time point, the cell media was removed and the cells again washed with PBS followed by 2-4 minutes incubation with trypsin-EDTA at room temperature. The wells were then washed with PBS and placed into FACS tubes (BD-Bioscience), and the cells were spun down to pellet. The cell supernatant was removed and the cells were re-suspended in 300μL FACS buffer (1% Bovine serum albumin (Sigma-Aldrich, St. Louis, MO), 1% sodium azide (Sigma) in PBS (Gibco)). The percentage of GFP and mean fluorescent intensity (MFI) were characterized by a LSR II flow cytometer (Bioscience, San Jose, CA). Polymer/luciferase-DNA plasmid controls were also included for each polymer to calibrate for the polymer autofluorescence. The

purity of the polymer/DNA complexes as well as media were tested for endotoxin activity using a Pyrogent LAL gel clot assay (Lonza), which showed that the endotoxin level was well below 0.125 EU/mL.

4.2.3. Fluorescent labeling and subcellular trafficking

The method used to monitor the subcellular trafficking of $PAEM_{75}$, PLL_{75}, and PEI polycationic polymers was the same as the method outline previously[110]. Initially, all three polymers were labeled with Oregon Gree-488 fluorescent label (Invitrogen) using the same protocol as outlined by Godbey et al. Excess fluorescent label was removed via dialysis using a 3,000 to 3,500 molecular weight dialysis tubing in de-ionized water (dH_2O) for 48 hours, with the water being replaced every 12 hours. The purified polymer solution was than lyophilized for 48 hours and suspended in sterile 20 mM HEPES buffer and stored at 4 °C until use. Luciferase-DNA plasmid was labeled with Cy5 fluorescent label using a Cy5 Label-*IT* kit (Mirus) and purified by ethanol precipitation according to the manufacture's protocol.

For monitoring cellular uptake, complex dissociation, and nuclear uptake/dissociation, fluorescently-labeled polymer/DNA complexes were formed using the same procedure as described above. Polymer/DNA complexes were used to transfect dendritic cells plated in 4-well Lab-Tek II chamber slides (Nunc) at a cell density of 100,000 cells/mL, in serum-free conditions. After which, the cells were washed with PBS and the cells replenished with complete 10% serum containing DC 2.4 or BMDC media. The subcellular trafficking was monitored at a number of time points including 1, 4, and 24 hours post initial transfection. Thirty minutes prior to imaging the cell nuclei was labeled with Hoechst 33342 at a final concentration of 30 mM. The cells were then

washed 2x with PBS and fixed using BD Cytofix according to the manufactures protocol. The cells were then mounted with SlowFade Gold® (Invitrogen) and covered with a coverslip and sealed with clear nail polish.

For endosomal entrapment, non-fluorescent labeled were complexed with Cy5-labeled luciferase DNA plasmid at an N:P ratio of 8:1. The cells were then incubated with the polymer/DNA complexes as described for cellular uptake. However, prior to imaging, the late endo/lysosomal bodies were labeled with a fluorescently labeled LAMP-1 antibody (eBioscience). After the designated incubation time, the cells were washed 2x with PBS and fixed with BD-Cytofix according to the manufacture's protocol. Next, the cells were permeabilized using 0.5% Saponin (Sigma) solution (in PBS) at room temperature for 30 minutes. The cells were then washed 2x with PBS and the cells suspended in PBS. Non-specific binding was prohibited by incubating the cells with CD16/32 antibody for 5 minutes on ice prior to addition of LAMP-1. Afterward, LAMP-1 and Hoechst 33342 were added to the cells and incubated on ice for 30 minutes. The cells were then washed 2x with PBS and mounted as described above. Confocal images were collected with an Olympus FV-1000 using a 60x/1.42 NA oil immersion lens equipped with Fluoview Imaging software.

4.2.4. Subcellular trafficking image quantification

Quantification of confocal images was modeled after procedures previously described elsewhere[90,110]. Three separate confocal images were captured for each treatment group and time points. The confocal images were randomized and the operator blinded to the treatment and time point. The confocal images were opened in ImageJ (NIH) software, and converted from 16-bit to 8-bit images, and the background

subtracted. A cell was selected at random and the outside of the cell was traced with a region of interest (ROI), which was determined by using the phase contrast channel. The amount of fluorescence within the cell was threshold and the pixel area for each cell slice was calculated. The total pixel area was calculated from the summation of the pixel area for each slice. The complex dissociation and endosomal entrapment was calculated by using the ImageJ colocalization plug-in using the colocalization of the Cy5 (red) and Oregon Green or LAMP-1 (green) channels. The percentage of complex dissociation/endosomal entrapment was calculated by dividing the total colocalization pixel area by the total pixel area. Finally, the nuclear uptake was quantified by drawing a ROI around the Hoechst 33342 labeled (blue channel) nuclei and the total pixel area of the Cy5-labeled DNA within the nucleus collected. The free-nuclear DNA was calculated by subtracting the total nuclear DNA pixel area by the complexed DNA pixel area. A total of 30 cells from each treatment group and time point was quantified as previously described[110].

4.2.5. LPS transfection and subcellular trafficking

Transfection and subcellular trafficking of BMDC treated with lipopolysaccharide (LPS) utilizes the same protocols outline above. However, the LPS were introduced at varying times (Prior, during, and post transfection) to ensure differing states of cell maturation. Twenty-four hours prior to initial transfection BMDC were incubated with 2 μL of LPS (Invitrogen) at a concentration of 2 μg/mL and incubated at 37 °C. Afterward, the media was removed and the cells washed 2x with warm PBS and replaced with serum-free BMDC media and then transfected as previously outlined. For co-treatment, the BMDC cell media was removed and washed 2x with warm PBS and transfected with

polymer/DNA complexes in conjugation with LPS for a total time of 4 hours. Then the media was removed and the cells were washed 2x with PBS and replaced with complete 10% serum BMDC media supplemented with 2 μL of LPS and incubated in cell culture conditions for an additional 20 hours. Cells that received post-treatment were transfected as normal, however, after transfection the serum-free media was removed and the cells washed 2x with PBS and replaced with complete 10% BMDC media containing 2 μL and incubated at cell culture conditions for 20 hours.

4.2.6. LPS induced BMDC maturation

In conjugation with the LPS-treated transfection, the BMDC cell maturation was also quantified. After cell harvesting, the cells were washed with PBS and spun down to pellet. The cell supernatant were removed and the cells re-suspended in 100 μL FACs buffer. Non-specific Fc-receptor binding was blocked by addition of FC16/32 blocking antibody to each sample for 5 minutes on ice. Next, co-stimulatory proteins CD40 (PE), CD80 (PerCp-Cy5.5), CD86 (Pacific Blue), as well as MHC class II I-Ab (Alexa Fluor 700) and dendritic cell marker $CD11c^+$ (PE-Cy7) (Biolegend) were labeled on ice for 15 minutes with a cocktail of antibodies according to the manufacture's protocol. In addition to the experimental treatment samples, compensation controls for each marker were made using LPS as the positive control and blank cells as the negative control. The cells were washed with 1 mL of FACs buffer and spun down. The cells were then re-suspended in 300 μL of FACs buffer. The degree of cell maturation was then quantified by using an LSR II flow cytometer and FACs-Diva software (BD-Bioscience).

4.2.7. LPS dextran cellular uptake inhibition

Similar to the LPS transfection experiment outlined above, BMDC were treated with LPS at varying times prior, during, and post-transfection. BMDC were incubated with 2 μL of FITC-labeled dextran (Sigma) at a concentration of 1mg/mL for 4 hours in serum-free conditions. After four hours the cells were washed and the media was replaced with complete 10% BMDC media and incubated for an additional 20 hours. After, the cells were washed with PBS and removed with trypsin-EDTA and placed into a FACs tubes. The cells were spun down and the supernatant removed and then suspended in 300 μL of FACs buffer. The cellular uptake of the FITC-labeled dextran was quantified by using a FACs Calibur flow cytometer.

4.3. Results and Discussion

In order for DNA vaccines to work effectively *in-vivo,* the transfection of dendritic cells is vital for orchestrating a significant immune response. With a number of dendritic cell lines and subsets, the ability to transfect immortal dendritic cell lines is the most important, since these cell lines will better represent the dendritic cell phenotype seen *in-vivo*. Therefore, in the present study, we examine the relationship between dendritic cell maturation state and transfection using two cationic polymers with well-defined chain-length and narrow weight distribution. To determine if different dendritic cell lines result in varying transfection efficiencies, two different dendritic cell lines- one an immortal bone marrow-derived dendritic cell (BMDC) and the other an immortalized dendritic cell (DC 2.4) which was previously transfected with a retro-virus expressing granulated macrophage colony-stimulating factor (GM-CSF) were transfected.

4.3.1. Dendritic cell transfection efficiency

The two cationic polymers ($PAEM_{75}$ and PLL_{75}) with specific molecular weights and narrow weight distribution were previously synthesized using living chain polymerization techniques[110]. These polymers have been previously reported to bind GFP plasmid to similar degrees as well as similar effective particle diameters and zeta-potential charges (Table 3.1). Polymer/DNA complexes were formed at an N:P ratio of 8:1 using GFP DNA plasmid in 20 mM HEPES buffer. Two different dendritic cell types, DC 2.4 and bone marrow-derived dendritic cells (BMDC), were transfected with the polymer/DNA complexes for 4 hours in serum-free media before changing the media back to 10% serum containing media for 20 hours. Antibody staining for $CD11c^+$ BMDC yielded a dendritic cell population of 85-92%, with the remaining population being mostly macrophage. After 24 hours, the transfection efficiency $PAEM_{75}$ and PEI in DC 2.4 cells is significantly higher than $CD11c^+$ BMDC (Figure 4.1). On the other hand, PLL_{75} has limited transfection efficiency in both dendritic cell lines, mostly due to the high endo/lysosomal entrapment of the polymer, thus limiting its efficiency[81]. The simple explanation for the difference of transfection between the two dendritic cell types may be due to a difference in the cellular uptake of the DNA complexes, which has been shown to affect the level of GFP expression[128]. Therefore, an in-depth investigation into the subcellular trafficking of fluorescently-labeled DNA plasmid and polymer was performed.

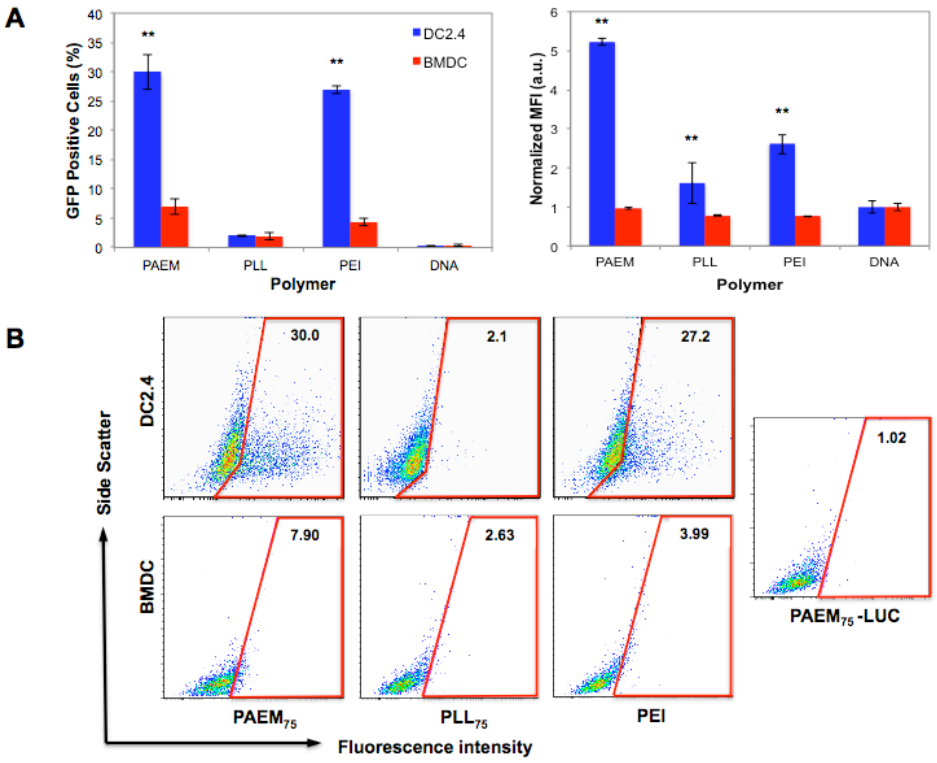

Figure 4.1. Transfection efficiency of cationic polymers in murine DC 2.4 and bone marrow-derived dendritic cells (BMDC) at 24 hours **(a)** Comparison of transfection efficiency between $PAEM_{75}$, PLL_{75} and PEI two murine dendritic cell lines, DC 2.4 and BMDC showing the percentage of GFP positive cells and the mean fluorescence intensity (MFI) as measured by flow cytometry. (**b**) Transfection flow cytometry dot plots, representing the difference in positive cells within a luciferase control gate. Percentage within the luciferase gate is percentage of GFP positive cells before correction for 1.02% luciferase overlap. Transfection efficiency data is represented by the mean and standard deviation of three (N = 3) experimental replicates. Mean fluorescent intensity is depicted in arbitrary units (a.u.). Statistical analysis was performed using a Student's t-test, (* $p < 0.05$, ** $p < 0.01$).

4.3.2. Dendritic cell subcellular trafficking

As has been seen in the past, the subcellular trafficking of polymer/DNA complexes can dictate transfection efficiency[90,110]. Therefore, we complex labeled a luciferase-DNA plasmid with a Cy5 fluorophore with an Oregon-Green 488 labeled polymer in order to visualize the trafficking of the complex within dendritic cells. Quantification of cellular uptake (level of Cy5 within the cell) showed similar amounts of cellular uptake between DC 2.4 and BMDC cells within the first hour; however, by 4 to 24 hours, the BMDC had significantly less cellular uptake than DC 2.4 cells (Figure 4.2).

Despite, the different cell types, all three cationic polymers were able to dissociate from the plasmid DNA.

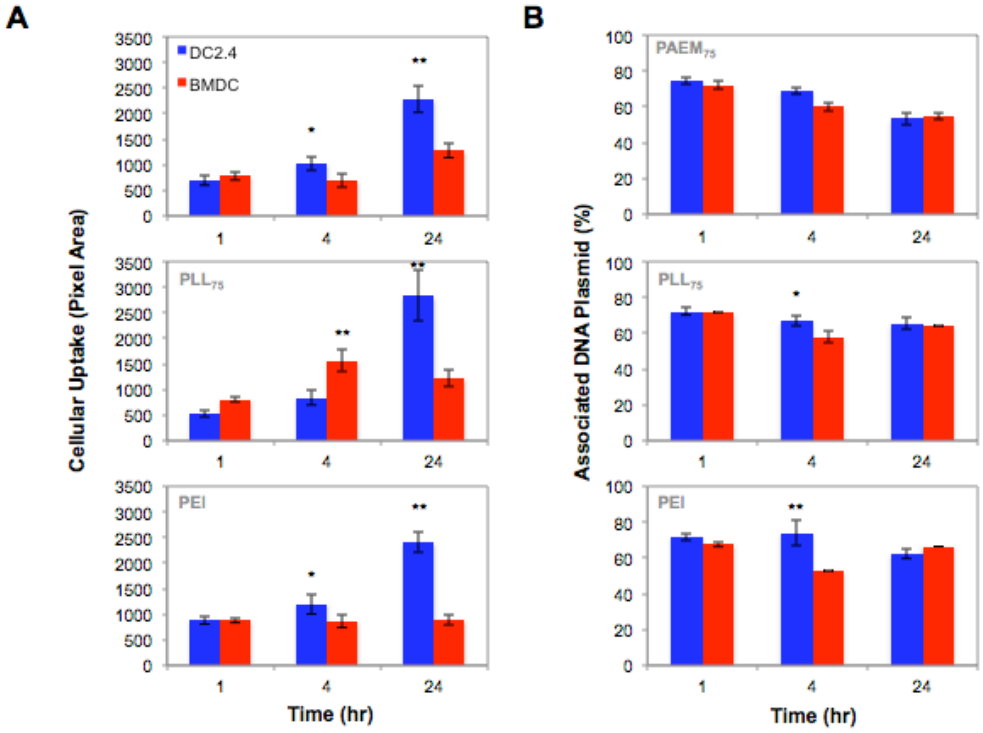

Figure 4.2. Subcellular trafficking of cationic polymers in murine DC 2.4 and bone marrow-derived dendritic cells (BMDC). **(a)** Quantification of the cellular uptake of PAEM75, PLL75, and PEI amongst DC2.4 and BMDC cells at time points of 1, 4, and 24 hours using Cy5 labeled luciferase DNA plasmid via confocal microscopy. (**b**) Quantification of the amount of Cy5-Luc DNA plasmid still associated with Oregon Green-488 labeled at 1, 4, and 24 hours. Subcellular trafficking data is represented by the mean and standard error of 30 cells randomly selected from three ($N = 3$) experimental replicates. Statistical analysis was performed using a Student's t-test, (* $p < 0.05$, ** $p < 0.01$)

PLL has been shown in the past to be susceptible to endolysosomal entrapment[3,81]. The amount of plasmid DNA Cy5 trafficked to endo/lysosomal vesicles could be quantified by labeling acidic vesicles with FITC-labeled LAMP-1 antibody, which labels exclusively for the late endosome or lysosome. As previously noted, PLL_{75} was unable to escape the endo/lysosome with upwards of 65% of the polymer/DNA complex being found within the acidic vesicles for both dendritic cell lines (Figure 4.3).

Similar results were found for $PAEM_{75}$ and PEI, which also displayed significant increases in the amount of DNA plasmid found within the endo/lysosome in BMDC cells.

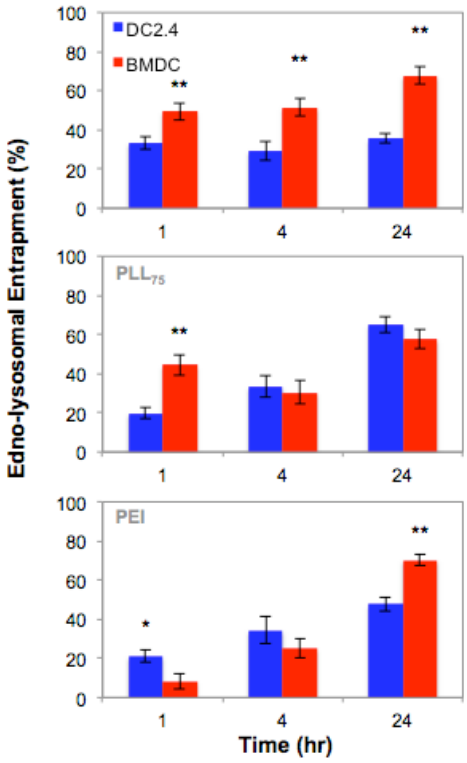

Figure 4.3. Endo-lysosomal entrapment of cationic polymers in murine DC 2.4 and bone marrow-derived dendritic cells (BMDC). Quantification of the percentage of Cy5-Luc DNA plasmid conferred within the lysosome via confocal microscopy. The lysosome was labeled using a FITC labeled LAMP-1 antibody. Lysosomal entrapment data is represented by the mean and standard error of 30 cells randomly selected from three ($N = 3$) experimental replicates. Statistical analysis was performed using a Student's t-test, (* $p < 0.05$, ** $p < 0.01$).

Since the target location of the DNA plasmid is the nucleus where the exogenous DNA plasmid is transcribed, the total amount of Cy5-labeled DNA plasmid as well as free Cy5 DNA plasmid was quantified. Despite having lower cellular uptake and endo/lysosomal escape, BMDC had higher amounts of total and free DNA within the cell nucleus within the first 4 hours compared to DC 2.4 cells (Figure 4.4A). However, by 24 hours, the quantity of DNA plasmid within the BMDC was significantly lower than DC 2.4 cells. The lower amount of DNA within the nucleus may limit the possibility of DNA

transcription, and a number of reports suggest DNA transcription may not occur if the plasmid is still protected by the cationic polymer[70,71]. Thus, the amount of free dissociated DNA plasmid within the nucleus was significantly lower amongst the BMDC cell line by 24 hours for both cell lines (Figure 4.4B). The lower cellular uptake of the polymer/DNA complexes, high endo/lysosomal entrapment, and low total and free nuclear uptake in BMDC correlates well with the lower transfection efficiency.

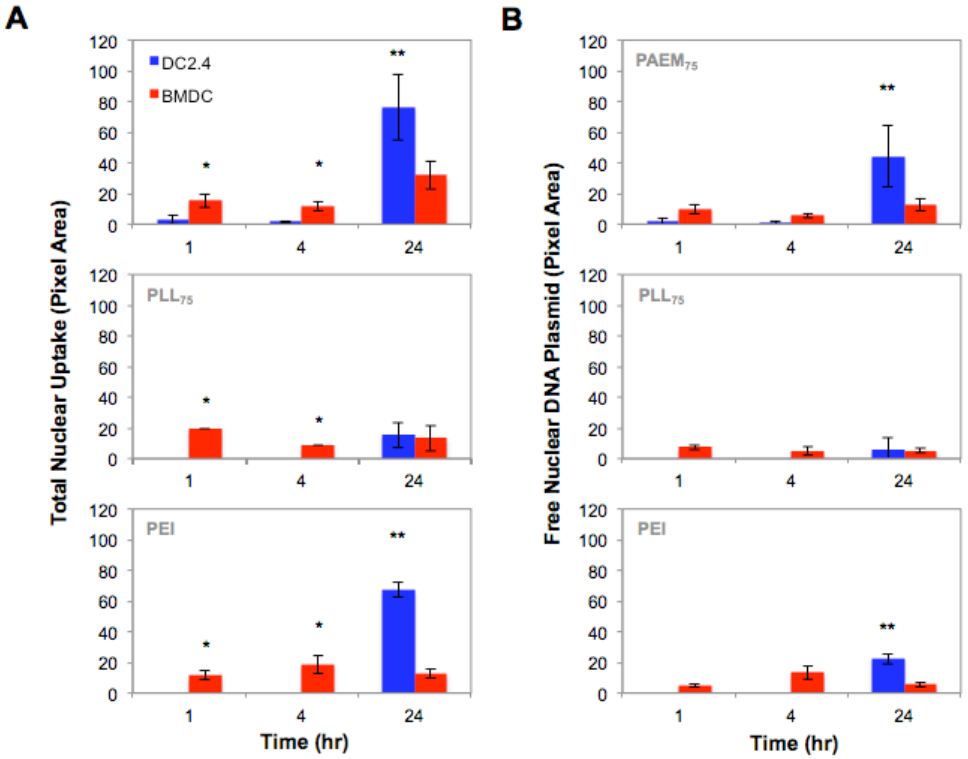

Figure 4.4. Nuclear uptake of cationic polymers in murine DC 2.4 and bone marrow-derived dendritic cells (BMDC). **(a)** Quantification of the total nuclear uptake of $PAEM_{75}$, PLL_{75}, and PEI in DC 2.4 and BMDC cells at time points of 1, 4, and 24 hours using Cy5 labeled luciferase DNA plasmid via confocal microscopy. (**b**) Quantification of the free (unbound) Cy5-Luc DNA plasmid within the nucleus. Subcellular trafficking data is represented by the mean and standard error of 30 cells randomly selected from three ($N = 3$) experimental replicates. Statistical analysis was performed using a Student's t-test, (* $p < 0.05$, ** $p < 0.01$).

4.3.3. LPS induced maturation states

Since DC 2.4 cells have been previously transfected with a retro-virus the state of dendritic cell maturation may play a role in the transfection efficiency and subcellular trafficking[148]. A number of reports have shown that maturation of BMDC have altered the cells phenotype; by decreased phagocytosis as shown by decreased cellular uptake of dextran[11,152,153] and increased gene transcription and cytokine production[154]. To drive BMDC into different maturation states, lipopolysaccharides (LPS) a graham negative bacteria, known to induce cell maturation in dendritic cells by utilizing the toll-like receptor (TLR), specifically TLR-4[155], was incorporated at different time intervals during transfection (Figure 4.5).

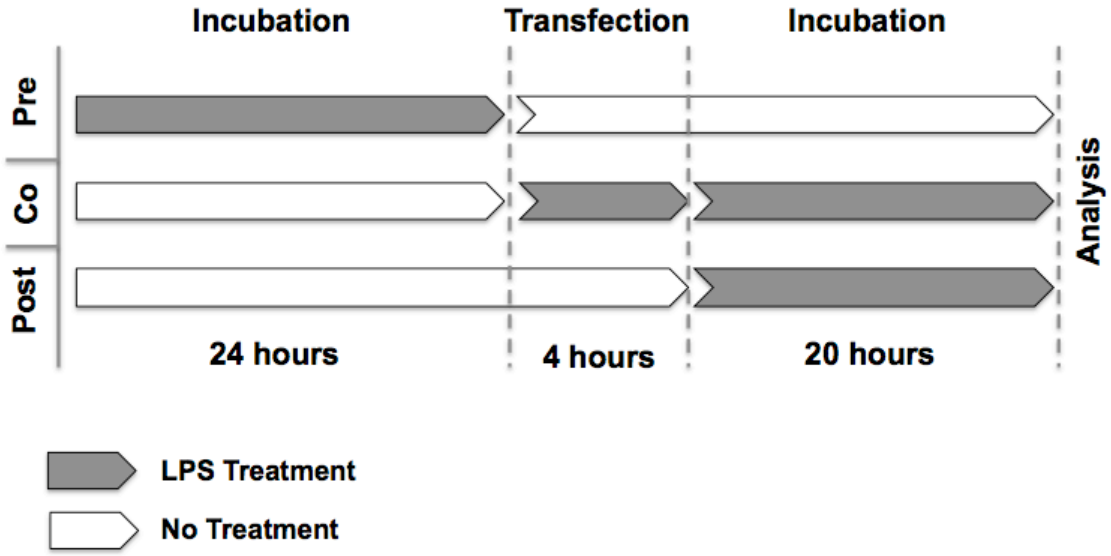

Figure 4.5. Timeline representing the lipopolysaccharide (LPS) treatment of murine dendritic cells. LPS treatment was administered in conjunction with transfection either prior (LPSPrior), during (LPSCo), or after (LPSPost) initial transfection. The concentration of LPS used was 2µg/mL.

Maturation of DCs caused an up-regulation of MHC I and II, CD80, CD86, and CD40 as well as CD83, p55 and LAMP and increased production of cytokines IL-12, IL-15, and IL-18, which are needed for stimulation of CD4+ T-cells[20]. Therefore, the

different states of maturation of BMDC were quantified via flow cytometry by labeling for co-stimulatory signals CD40, CD80, CD86, and MHC Class II (I-Ab) (Figure 4.6). By introducing LPS 24 hours prior (LPS^{Pre}) to transfection, the state of maturation for BMDC was higher than BMDC co-treated (LPS^{Co}) and post-treatment (LPS^{Post}) with LPS. This drove the BMDC into a semi-mature state, yet higher than the non-treated control (LPS^{Non}). Supporting evidence has been reported that the time of LPS incubation may affect the state of maturation within BMDC[155,156]. Yet, when the level of maturation was compared between the dendritic cell lines, the CD40 and CD80 signal for DC 2.4 cells was significantly higher than that of BMDC, suggesting the DC 2.4 cells produced a stronger co-stimulatory response. However, the BMDC had a broader range and higher signal for co-stimulatory CD86, and MHC Class II (I-Ab) suggesting that the BMDC were producing a more overall robust maturation (Figure 4.6A). Comparison of both the dendritic cell baseline LPS^{Non} groups, the maturation state of DC 2.4 is higher than that of BMDC, suggesting that the semi-mature state of the DC 2.4 might be responsible for the higher level of transfection efficiency.

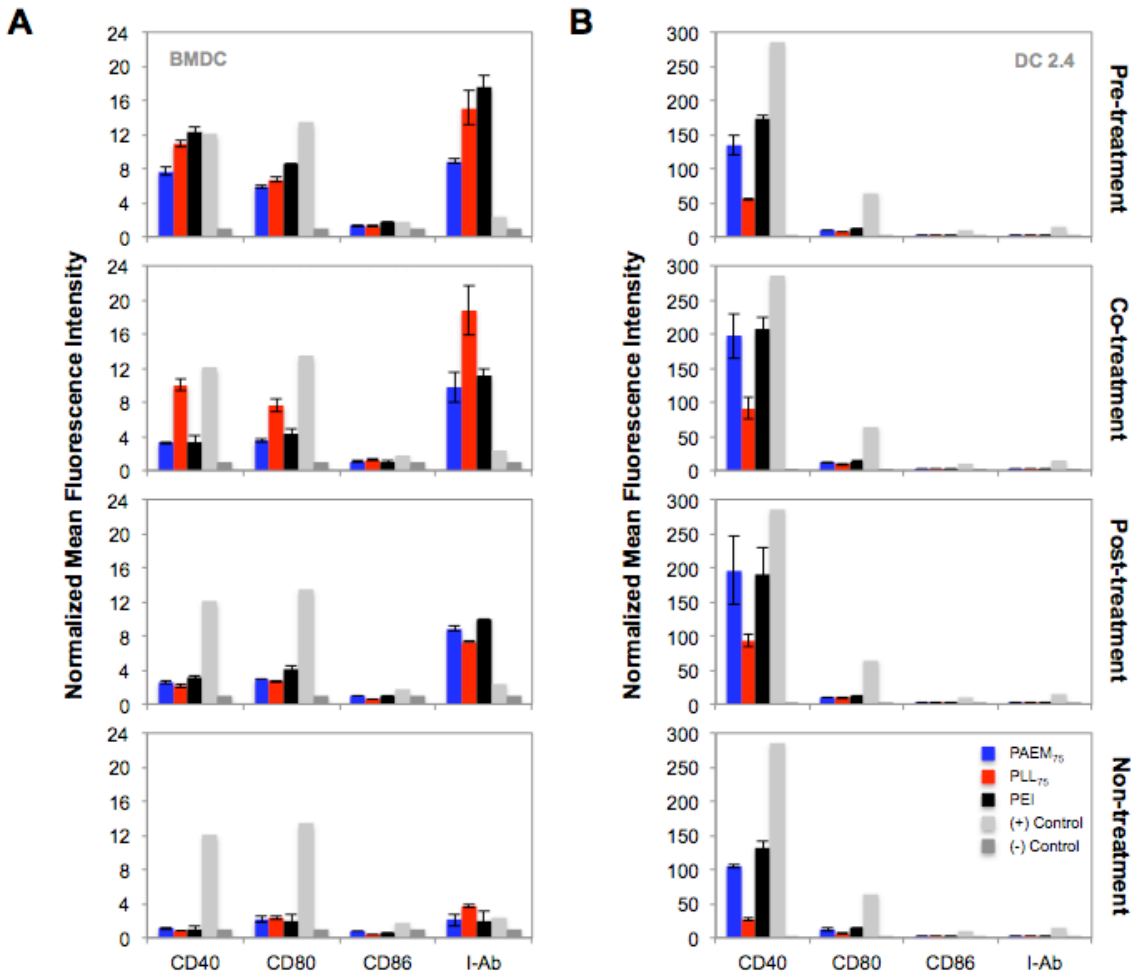

Figure 4.6. Dendritic cell maturation state represented by co-stimulatory upregulation. **(a)** Quantification of the co-stimulatory proteins CD40, CD80, and CD86 in BMDC cells after treatment with LPS at varying time points within transfection with $PAEM_{75}$, PLL_{75}, and PEI (**b**) State of dendritic cell maturation of DC 2.4 cells after stimulation with LPS in conjunction with transfection. The degree of cell maturation was quantified by measuring the mean fluorescence intensity of anti-body specific fluorophores. Maturation data is represented by the mean and standard deviation from three (N = 3) experimental replicates. Statistical analysis was performed using a Student's t-test, (* $p < 0.05$, ** $p < 0.01$).

4.3.4. LPS treated transfection efficiency of BMDC

The effect of the LPS treatment on the transfection efficiency of BMDC was studied by again treating BMDC with LPS at various time points: LPS^{Pre}, LPS^{Co}, and LPS^{Post}. Interestingly, the percentage of GFP-positive cells increased for $PAEM_{75}$ during co and post-incubation of the BMDC with LPS and the polymer/DNA complexes (Figure 4.7A); almost to a similar transfection level to that of $PAEM_{75}$ in DC 2.4 cells (Figure

4.1). Yet, despite the high percentage of GFP-positive cells the mean fluorescence intensity these cells possessed was similar to those of the control non-treatment group (Figure 4.7A).

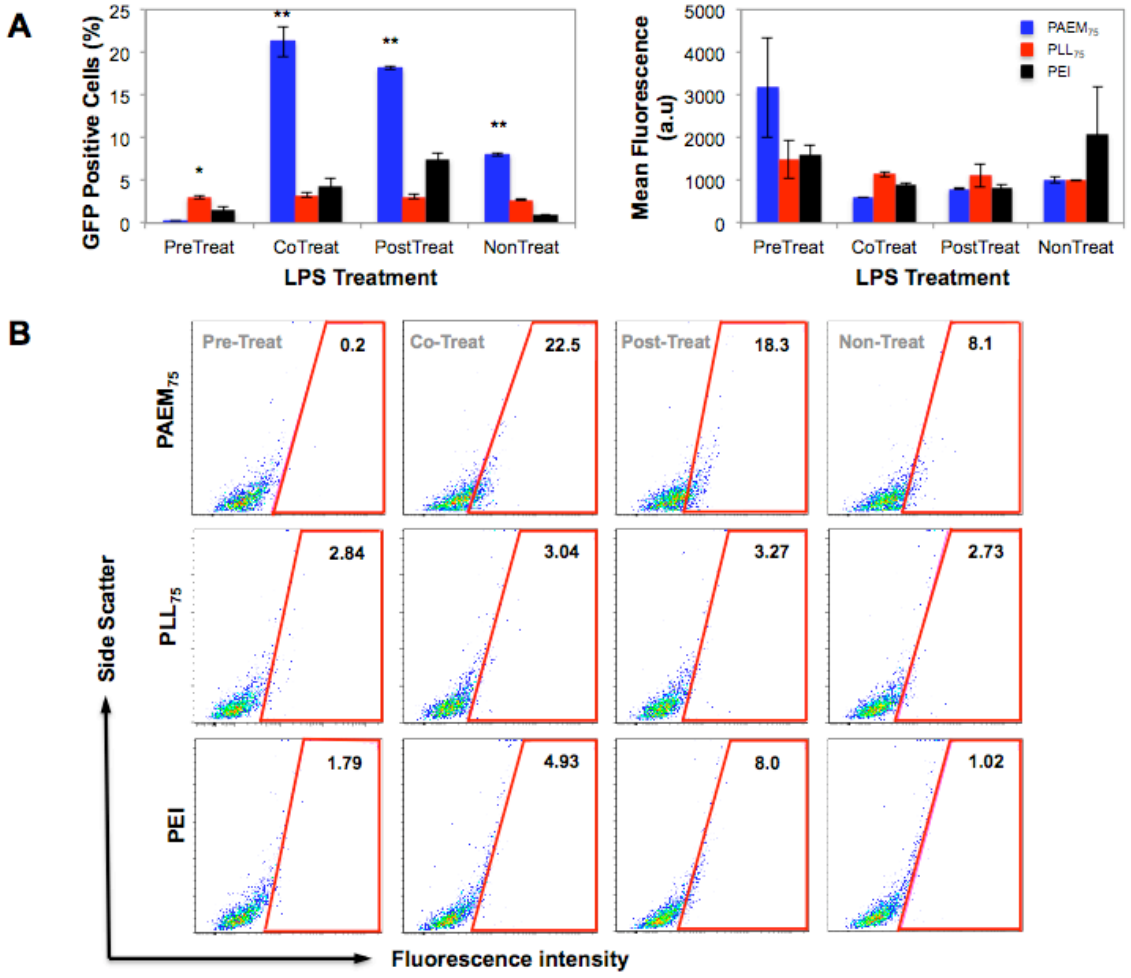

Figure 4.7. Transfection efficiency of LPS activated bone marrow derived dendritic cells. **(a)** Transfection efficiency of PAEM75, PLL75, and PEI in BMDC at different states of activation. (**b**) Flow cytometry dot plots representing the cell population shifts as a result of dendritic cell activation with LPS. The transfection efficiency was quantified by measuring the percentage of GFP positive cells as well as the mean fluorescence intensity (MFI). Transfection data is represented by the mean and standard deviation from three ($N = 3$) experimental replicates. Statistical analysis was performed using a Student's t-test, (* $p < 0.05$, ** $p < 0.01$).

The flow cytometry dot plots showed there was a shift in the overall cell population into the GFP-positive gate when compared to the luciferase-negative gate control. Yet the mean fluorescence intensity of these cells remained similar to that of the

non-treatment group (Figure 4.8). This is most likely a result of elevated transcription and translation of dendritic cell innate activation and maturation proteins[154]. This can only be verified by carrying out real-time PCR (RT-PCR) to measure the mRNA levels of the GFP DNA plasmid.

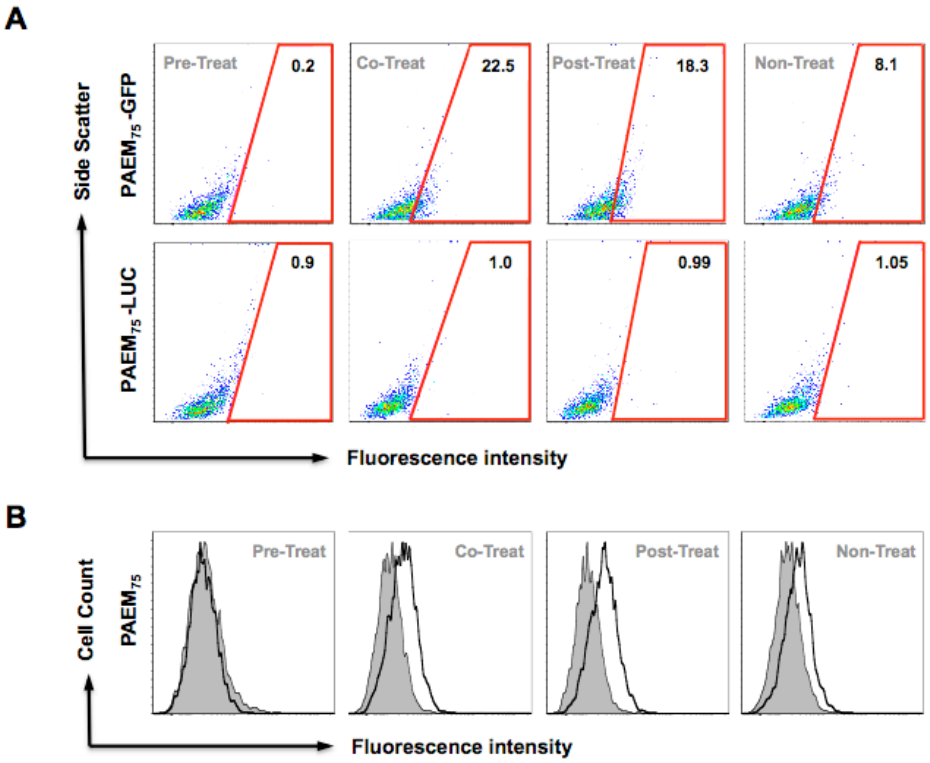

Figure 4.8. Transfection efficiency of LPS activated bone marrow derived dendritic cells. **(a)** Flow cytometry dot plots of $PAEM_{75}$, PLL_{75}, and PEI in BMDC at different states of activation compared to the LUC control gate show a positive shift of the cell population (**b**) Fluorescence intensity histograms representing the cell population shifts as a result of dendritic cell activation with LPS. Transfection data is represented by the mean representative GFP positive cell population of ($N = 3$) experimental replicates.

4.3.5. LPS treated subcellular trafficking of BMDC

Initial reports have shown that maturation of dendritic cells limits phagocytosis of dextran into the cell; therefore, we incubated BMDC with FITC-labeled dextran after treating the cells with LPS using the same interval cycle used for the maturation. Of the four treatment groups the only group to limit the uptake of dextran was the LPS^{Pre} group;

the three remaining groups did not limit uptake (Figure 4.9). These results are similar to other reports, which limit the cellular uptake of dextran through dendritic cell maturation[152,153]. Interestingly, when using polymer/DNA complexes the cellular uptake is not limited by the LPS^{Pre} treatment like dextran. Rather, the cellular uptake is only limited by LPS^{Post} treatment, which may be a result of the LPS activating the dendritic cells thus arresting the cellular uptake of the polyplexes into the cell (Figure 4.10).

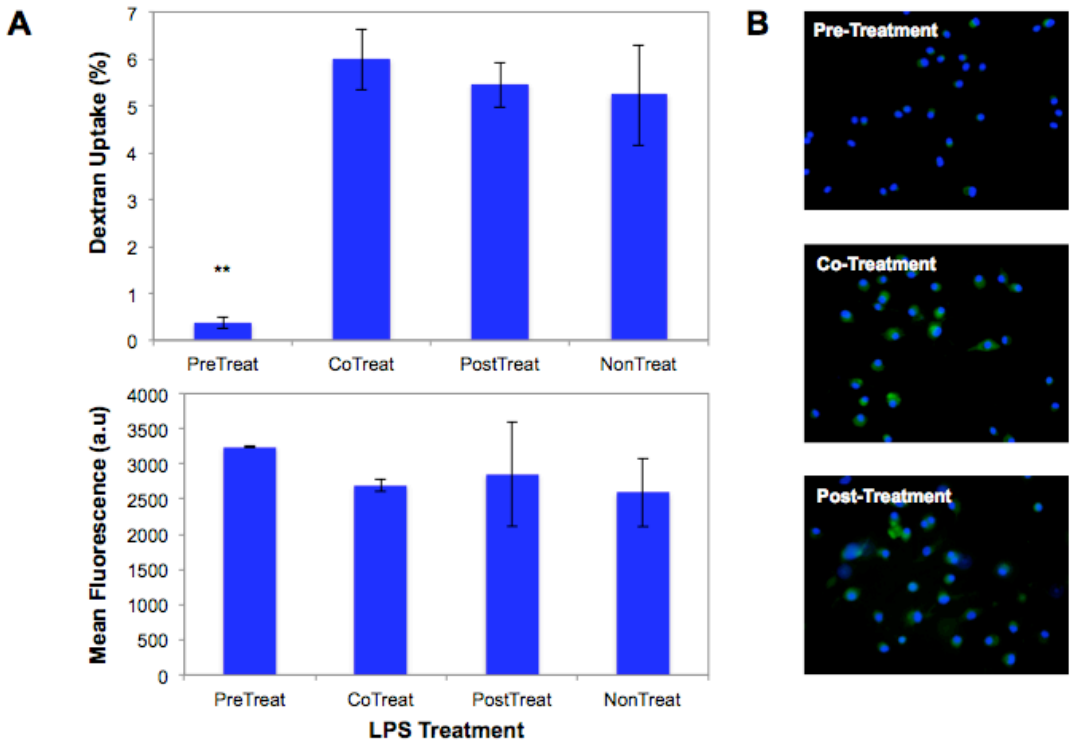

Figure 4.9. Cellular uptake inhibition of dextran. **(a)** Quantification of FITC-dextran inhibition in semi-maturated BMDC as a result of LPS activation by flow cytometry. **(b)** fluorescent microscopy images of FITC-dextran cellular uptake. Cellular uptake data is represented by the mean and standard deviation from three (N = 3) experimental replicates. Statistical analysis was performed using a Student's t-test, (* $p < 0.05$, ** $p < 0.01$).

Overall, the cellular uptake of the complexes is not limited by the state of maturation of the dendritic cells, this may be due to the polymer/DNA complexes utilizing a different endocytotic pathway, such as caveolae or lipid raft dependent entry,

while dextran uses a mannose receptor mediated pathway[152]. The endocytotic pathway used by the $PAEM_{75}$ and PLL_{75} complexes, was unfortunately unable to be studied here, since initial MTT assays showed that endocytotic inhibitors, Filipin III and chlorpromazine are extremely cytotoxic to BMDC (data not shown). The state of maturation also has limited effect on the state of endo/lysosomal entrapped and nuclear uptake (Figure 4.10B).

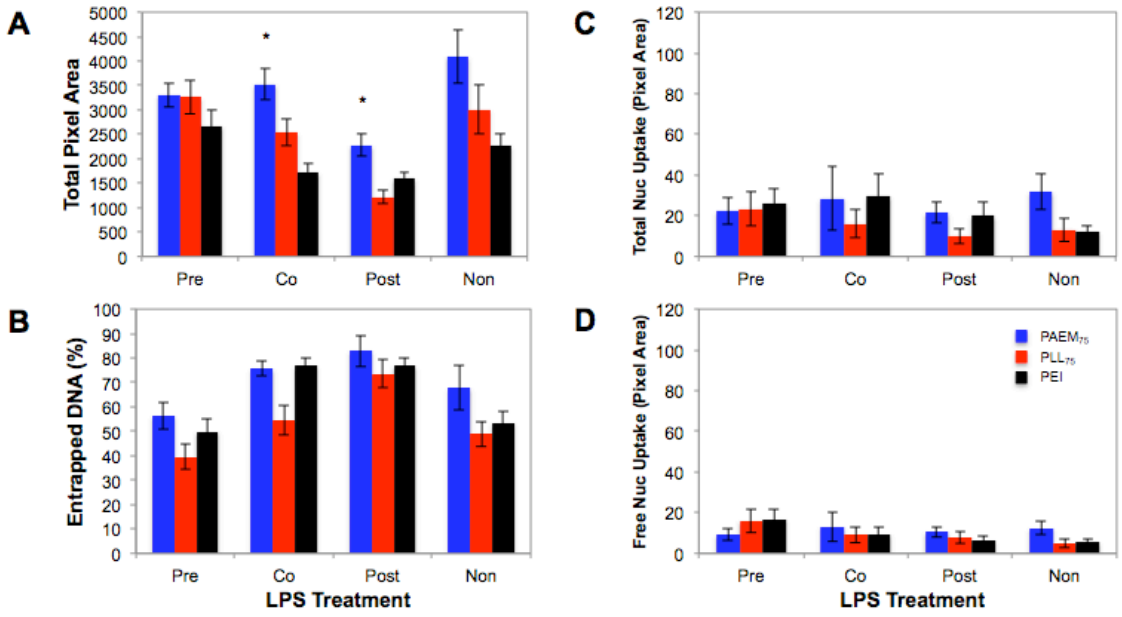

Figure 4.10. Subcellular trafficking of cationic polymers in activated BMDC. **(a)** Cellular uptake, **(b)** lysosomal entrapment, and **(c,d)** nuclear uptake of $PAEM_{75}$, PLL_{75} and PEI in BMDC as a function of maturation state after 24 hours. Subcellular trafficking data is represented by the mean and standard error of 30 cells randomly selected from three ($N = 3$) experimental replicates. Statistical analysis was performed using a Student's t-test, (* $p < 0.05$, ** $p < 0.01$).

Interestingly, the LPS affected the endo/lysosomal entrapment of these polymer/DNA complexes, in that the percentage of the complexes entrapped within the endo/lysosome increased slightly for the LPS^{Co} and LPS^{Post} treatment groups (Figure 4.10B). Despite the higher volume of Cy5-labeled DNA within the endo/lysosome, the quantity of Cy5-labeled DNA whether total or free did not change with any of the LPS

treatments, when compared to non-treatment (Figure 4.10C). We believe the increase in the percentage of GFP-positive cells is a result of elevated gene transcription occurring within the semi-mature BMDC dendritic cells. This also potentially explains why the mean fluorescence of these cells was low since, it has been shown that dendritic cell activation also up-regulates the transcription of specific maturation and activation proteins[154]. More specifically, more of the GFP plasmid is being transcribed in the semi-mature cells but the urgency to translate the protein is minimal compared to other vital proteins.

4.4. Conclusions

From this work we were able to conclude that despite similarities in cell type, lineage differences in transfection efficiency stem from differences within subcellular trafficking. We were also able to show that incubating bone marrow-derived dendritic cells (BMDC) with lipopolysaccrides (LPS) for different time intervals drove dendritic cells into different degrees of cell maturation. Also, semi-mature dendritic cells have an elevated level of gene transfection compared to immature cells. However, the minimal effect of maturation on the subcellular trafficking and the minimal mean fluorescence intensity (MFI) of BMDC GFP-positive cells points to the possibility that the influence on gene transfection might be independent of the delivery processes such as cellular uptake, endo/lysosomal entrapment, and nuclear uptake, but rather through post-delivery events such as transcriptional and translational processes.

Chapter 5: Cationic Polymer Trafficking Efficacy in *In-Vitro* and *In-Vivo* Tumor Models

5.1. Introduction

Chemotherapy is one of a number of currently used treatments for cancer, yet despite its effectiveness in some cases, it has a number of drawbacks, which limit chemotherapeutics efficacy. Two of the major obstacles impeding chemotherapeutics are poor water solubility[157] and unintentional targeting of proliferating or dividing cells, specifically in the bone marrow or digestive tract[158]. As a result of these drawbacks, the concentration and frequency of chemotherapy treatments have been limited, with the intention on improving drug solubility and patient comfort, at the cost of drug effectiveness[159]. In order to improve the potency of poorly soluble chemotherapeutic drugs, such as doxorubicin, into cancer cells, researchers have packaged chemotherapy drugs into micelles[160] and polymerosomes[161]. Delivery of these drug-filled micelles is then delivered to the cell via the enhanced permeability and retention (EPR) effect, where the chemotherapy is delivered to the tumor[162]. Yet, the micelle size and morphology are important for enhanced delivery of these systems into the tumor extracellular matrix[163]. Recently, an effort focused on the use of naturally occurring peptides, such as melittin, magainins, defensins, and lactoferrins, to target and disrupt the cellular membrane of cancer cells[158]. However, the clinical use of such peptides as anti-cancer drugs is limited by poor production and stability[164]. Coincidentally, similar work is being done using cationic polymers as antimicrobial agents, due to their high cytotoxicity and cell membrane disruption[165]. Cationic polymers make an ideal anti-cancer drug therapy since they offer a number of benefits such as high stability, easy production, water solubility

and polymer modification. Here, we examined the effect of a cytotoxic cationic polymer, poly (6-amino-1-hexyl methacrylate) (PAHM), synthesized in our lab for use as an anti-cancer drug using 2-dimensional and 3-dimensional toxicity assays of human and mouse cell lines as well as through *in-vivo* breast cancer tumor challenge.

5.2. Experimental Methods and Materials

5.2.1. Polymer cytotoxicity characterization

The cytotoxicity of PAHM polymers was assessed by means of 2-D cell viability MTT assays using four different cancer cell lines: mouse breast cancer cell line EMT-6 (ATCC, Manassas, VA), human breast cancer cell lines MDA-MB-231 (ATCC) and MCF-7 (ATCC), and human glioblastoma cancer cell line T98 (ATCC) after 24 and 48 hours of treatment, while doxorubicin was used a control. All of the four cancer cell lines were incubated in corresponding cell culture media, EMT-6 media (DMEM high glucose, 10% FBS, 100 U/mL penicillin/streptomycin), T98 and MDA-MB-231 media (DMEM low glucose, 10% FBS, 100 U/mL penicillin/streptomycin), MCF-7 media (DMEM low glucose, 10% FBS, Humulin insulin, 100 U/mL penicillin/streptomycin), at 37° C, and a humidified atmosphere containing 5% CO_2.

EMT-6 cells were seeded into 96-well plates at 5000 cells/well and cultured for 20h in EMT-6 media at 5% CO_2 and 37°C. Afterwards, polymers of various molecular weight and concentrations were added to the cells and cultured for 24 or 48 hours. MTT in PBS (5 mg/mL, 20 μL) was then added to each well, reaching a final concentration of 0.5 mg/mL. After 4 hours, unreacted MTT was removed by aspiration. The formazan crystals were dissolved in 150 μL of DMSO, and the absorbance was measured at 570 nm

using a Bio-Tek Synergy HT plate reader. Cell viability was calculated by [absorbance of cells exposed to polymers]/ [absorbance of cells cultured without polymers] in percentage. The concentration of drug needed to reduce the cell density by 50% (IC_{50}) was recorded.

5.2.2. Tumor spheroid formation

The tumor spheroid formation utilized a method devised by Friedrich et al. as previously described[166]. The initial seeding of tumor spheroids began with lining the bottom of 96 well plates (Corning) with an agarose solution made up of 0.15 g agarose mixed with 10mL of DMEM low glucose media. The agarose was sealed with aluminum and sterilized for 20 minutes at 120° C and 2 bar. After sterilization the agarose solution was removed and placed onto a hot plate (~ 60° C) inside of a sterile tissue culture hood for plating. Using an Eppendorf multi-well pipette 60 μL of the warm agarose solution was placed into the bottom of a flat bottom 96 well plate. The agarose was allowed to solidify for 5 minutes before addition of the cells. In order to produce spheroids of a diameter of approximately 200 μm, 200 μL of either human T98 (glioblastoma) or MCF-7 (breast cancer) cells were plated on top of the solidified agarose at a cell density of 7,500 cells per mL and incubated in a cell culture incubator at 37° C, 99% humidity, and 5% CO_2 for 10 days.

5.2.3. Tumor spheroid characterization

The tumor spheroids were characterized using both fluorescent and white light microscopy. Images of the initial spheroid formation were collected using the phase contrast capabilities of an Olympus IX-70 fluorescent microscope after 24 hours, 4 days, and 10 days. In order to verify the presence of a live outer shell and necrotic inner core

within the tumor spheroids, live/dead staining (Invitrogen) was used according to the manufacture's protocol. A cocktail of calcein (1mg/mL) and ethidium homodimer (2mM) were mixed and introduced to the spheroid media 30 minutes prior to imaging. The spheroids were imaged using an Olympus FV-1000 IX-2 inverted confocal microscope using a 10x/1.42 NA lens.

5.2.4. Fluorescent drug penetration

Labeling of the polymer vectors were carried out by a method previously described elsewhere[81] using Alexa Fluor 594 carboxylic acid, succinimidyl ester (Invitrogen, Eugene, OR). The Alexa Fluor 594 label was diluted in DMSO to a concentration of 10 mg/mL. $PAHM_{20}$ were then incubated while stirring with the Alexa Fluor 594 label at a final concentration of 1 mg/mL for 1 hour in the dark at room temperature, followed by an additional hour incubation in the dark without stirring. Excess dye was removed with a 3,500 molecular weight dialysis tube (SpectraLabs, Spectra/Por Dialysis Membrane in 0.1% sodium azide), and placed into 1-liter of de-ionized water and stirred at 4° C for 8 hours. The de-ionized water was changed and the sample stirred for an additional 12 hours. The sample was then removed and placed into a sterile 15-mL Falcon tube and frozen at -80° C overnight. Finally, the samples were placed on a lyophilizer for 48-72 hours to freeze dry. The samples were then weighed and re-suspended in 20mM HEPES buffer at a concentration of 2.5 mg/mL. The PAHM-AF594 was further sterilized by passing the polymer solution through a 0.22 micron filter. Penetration was quantified using ImageJ image analysis software. First, a region of interest was drawn around the outer perimeter of the spheroid and the area was measured. Next, the inner area of the drug treatment perimeter was measured and then

subtracted from the outer area measurement. The data was normalized to allow for differences in spheroid area between the experiments.

5.2.5. In-vitro spheroid PAHM cytotoxicity

T98 and MCF-7 spheroids were seeded as outlined above. PAHM polymers with varying chain lengths of 18, 38, and 100 repeating units were aliquoted into serial dilutions of 1, 40, and 400 μg/mL. A volume of 20 μL of PAHM was introduced to 10-day old T98 glioblastoma spheroids after an initial white light microscopy image was collected. The spheroid geometry was continuously monitored by collecting microscopy images over the course of 28 days. Polyethylenimine (PEI) and doxorubicin (DOX-HCl) were used as positive controls and non-treated T98 spheroids served as a negative control. The area of each spheroid treatment group was quantified using ImageJ imaging software. A region of interest (ROI) was drawn around the outer diameter of the spheroid and the area of the ROI was quantified in conjunction with the spheroid perimeter and Feret diameter for each time point. The area of each spheroid was plotted as a function of polymer concentration.

5.2.6. In-vivo tumor challenge

Thirty female 12-14 week old Balb/C mice were seeded with EMT-6 cells under the third nipple on the left flank as previously described above. The mice were allowed to incubate under constant food and water for 7 days prior to experimental treatments. After 7 days the mice were randomized into six groups of five mice. The mouse weight was recorded and the tumor length and width were measured using digital calipers. The mice were ear tagged for identification and animal tracking before the mice were injected with 20μL of $PAHM_{20}$ (9.1 mg/kg), $PAHM_{20}$ (3.6 mg/kg), or PBS intratumorally. The

mice were monitored every day and the tumor geometry and mouse weight were recorded every second day post injection. The mice were injected every fourth day after the previous injection. The tumor volume was calculated using the following equation [(length^2) x (width)]/2. After 18 days the mice were euthanized by CO_2 inhalation and the tumor, spleen, kidneys, liver, and lungs were harvested and fixed in 4% paraformaldehyde for 24 hours at 4° C. Prior to fixation, the harvested tumor length and width, as well as tumor weight, were recorded. Pictures were captured for each animal post organ-harvesting for comparison.

5.2.7. Live animal imaging

A single female 14-week old Balb/C mouse was seeded with 2 million murine EMT-6 breast cancer cells suspended in PBS via subcutaneous injection under the third proximal nipple on the left flank and allowed to grow for 8 days. After 8 days of incubation, the mouse was anesthetized with isofluorene. A single 20 μL injection of PAHM-AF750 (3.6 mg/mL) was administered into the center of the tumor and released over the course of 30 seconds. The mouse was then imaged using a Xenogen Live Animal Imaging workstation. The fluorescence filter pair and filter scan were used to capture the PAHM-AF750 emission. The baseline fluorescence was visualized after 0, 10, 20 and 30-minutes post initial injection. The animal received follow-up booster injections on day 4 and day 8 post initial injection with live animal imaging occurring directly prior to and after the injection for comparison. Additional live animal images were taken on days 1, 3, 6, and 10 for comparison with post injection images. On day 10 the mouse euthanized by CO_2 inhalation and dissected. The dissected mouse was imaged to verify the biodistribution of the PAHM-AF750 within other organs or tissues within

the mouse. The tumor, spleen, kidneys, liver, and lungs were further dissected and harvested from the mouse and imaged separately in the Xenogen Spectrum to confirm the absence of fluorescent labeling in the peripheral organs. The Xenogen data was analyzed using Living Image V4.1 (Caliper LifeSciences). The fluorescent intensity scale for all PAHM-AF750 sample time points was set using the fluorescent only control imaged prior to the experiment. All animals were handled and euthanized in accordance to the regulations and guidelines set forth by the University of Minnesota IACUC and animal review board.

5.2.8. Statistical analysis

Statistical analysis was carried out using a two-sample Student's t-test with unequal variance. Statistical significance was determined as a p-value, which was less than 5%.

5.3. Results and Discussion

5.3.1. Polymer characterization and cell cytotoxicity

The efficacy of PAHM as an anti-cancer drug was screened using a simple 2-D MTT cell viability assay. The MTT assay consisted of a number of cancer cell lines including human glioblastoma (T98), breast cancer (MCF-7 and MDA-MB-231) and murine breast cancer (EMT-6). Doxorubicin (DOX-HCl) was used as a control for comparison since it is frequently used as treatment in these cell lines[167-169]. Each cancer cell line was plated into 96 well plates and incubated over night in normal cell culture conditions. After 24 hours, the cells were incubated with varying concentrations of $PAHM_{18}$, $PAHM_{38}$, and $PAHM_{100}$ over the course of 24 and 48 hours with the

concentration of each anticancer drug required to decrease the cell viability of each cancer cell lines (IC_{50}) being measured (Table 5.1). Of the four cancer cell lines used the PAHM polymer possessed a lower IC_{50} concentration than DOX-HCl for all three of the human cell lines T98, MCF-7 and MDA-MB-231, this is most likely do to these cancer cell lines being drug resistant and having limited reaction to DOX-HCl[159,170,171]. However, the cell viability of EMT-6 cells is decreased more efficiently by the DOX-HCl, as compared to the PAHM groups despite being known to be semi-multidrug resistant. *In-vitro* culturing of EMT-6 cells has been previously shown to decrease the multi-drug resistance, which might explain their sensitivity to DOX-HCl[172]. Interestingly, there did not appear to be any correlation between the PAHM molecular weight and IC_{50} (Table 5.1).

Despite displaying the ability of PAHM to decrease the overall cell viability of a number of cancer cell lines in two-dimensional (2-D) cell culture assays, the ability of 2-D cultures themselves to accurately predict the efficacy of an anti-cancer drug is hindered. More specifically, 2-D cell culture assays offer insufficient tissue-specific cell-to-cell interactions and cell-to-extracellular matrix since cells cultured in a monolayer environment often possess different phenotypical characteristics than those exhibited *in-vivo*[173,174]. It is these cell-to-cell interactions, which may dictate the true efficacy of the drug being tested. That has been seen firsthand with EMT-6 cells losing their resistance to DOX-HCl in 2-D culture (Table 5.1).

Table 5.1. PAHM cancer cell viability assay. (Data collected and provided by Weihang Ji)

Cell Line	Cell Type	Species	Time (h)	Anticancer Drug [μg/mL]			
				$PAHM_{18}$	$PAHM_{38}$	$PAHM_{100}$	DOX-HCl
EMT-6	Breast Cancer	Mouse	24	18	16	10	8
			48	12	14	10	4
MDA-MB-231	Breast Cancer	Human	24	9	14	13	27
			48	14	12	14	5
MCF-7	Breast Cancer	Human	24	12	18	11	N/A[a]
			48	12	11	8	25
T98	Glioblastoma	Human	24	16	16	13	35
			48	10	9	9	20

[a] No specific DOX-HCl concentration lowered the cell viability below the 50% threshold

5.3.2. Tumor spheroid formation

Three-dimensional tumor spheroids offer the benefit of the cells maintaining their original phenotype as well as establishing cell-to-cell interactions and regions of peripheral cell proliferation (outer region) and oxygen nutrient deficient hypoxia regions (center) which are more commonly seen *in-vivo* (Figure 5.1.)[174]. Therefore, in order to evaluate whether PAHM polymers can in fact be used as anti-cancer drugs *in-vivo*, we implemented a new cytotoxicity assay using three-dimensional tumor spheroids, consisting of the same cancer cell lines (T98 and MCF-7) used in the 2-D cell viability assay. Seeding of T98 glioblastoma cells using an agarose gel gravity technique was able to produce tumoral spheroids with a number of different diameters depending on the concentration of the initial cell seeding density. Higher concentrations of cells produced larger spheroids than spheroids seeded with lower cell concentration (Figure 5.1.B).

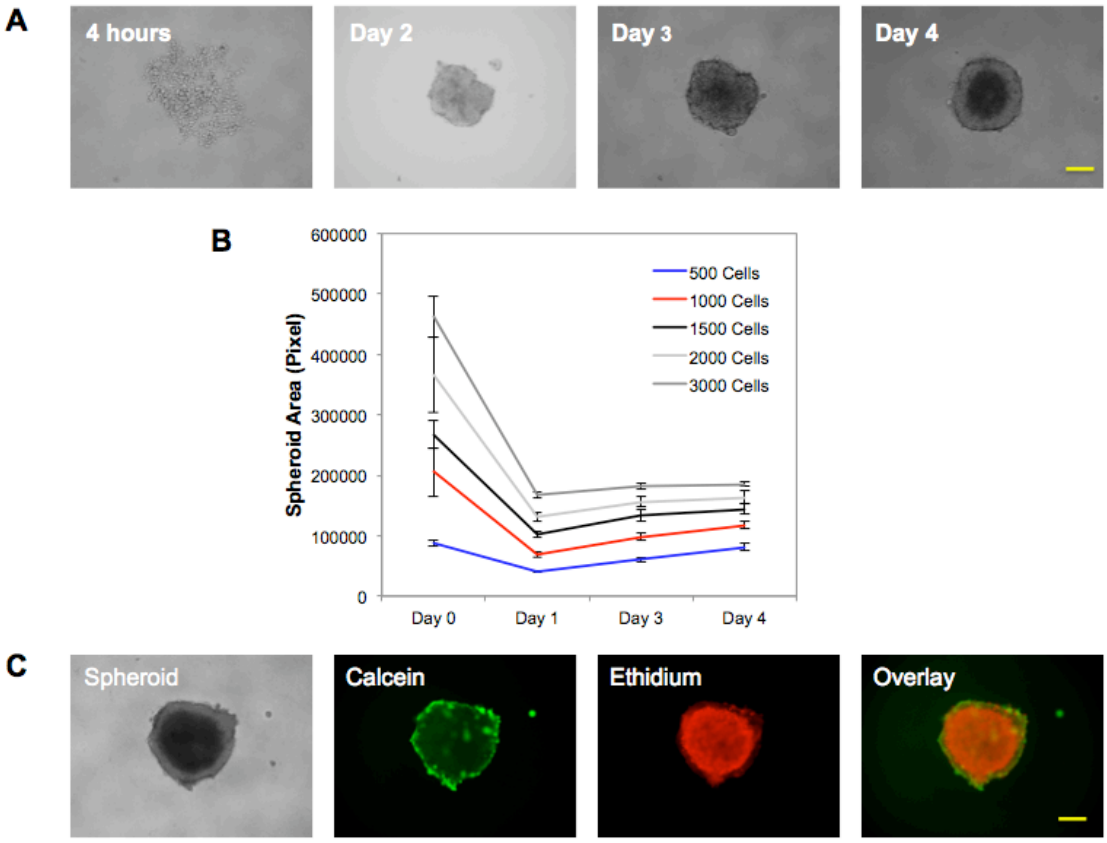

Figure 5.1. T98 glioblastoma tumor spheroid characterization. (**a**) Optical microscopy images of the formation of T98 spheroids over the course of 4 days. (**b**) Quantification of the T98 spheroids area over the same 4 day time course. (**c**) Fluorescent verification of the spheroid green proliferative outer core (calcein) and red hypoxia/necrotic inner core (ethidium homodimer). All images were captured using a 10x/0.25 NA. T98 spheroid size was quantified using ImageJ using N=3 spheroids per time point. Scale bar = 200 µm. Statistical analysis was performed using a Student's t-test, (* $p < 0.05$, ** $p < 0.01$, # $p < 0.001$).

This is of great importance since the ability to fine tune spheroids allows for the construction of two distinct regions within the spheroid, the first being along the spheroid periphery where the spheroid cells proliferate and expand. The second region is the nutrient and oxygen deficient hypoxia core which has been shown to be resistant to drug penetration[175]. Formation of tumor spheroids with T98 cell has shown the genesis of these two regions suggesting the proper formation of tumor spheroids (Figure 5.1). Live/dead staining of the tumor spheroids after 10 days post initial cell seeding, using calcein (live stain) and ethidium homodimer (dead stain) was carried out to verify the

existence of a live outer ring surrounding the hypoxia inner core (Figure 5.1.C). Visualization of the staining was done using confocal microscopy, which shows that the spheroid is in fact made up of two distinct regions, one outer living shell surrounding a necrotic nutrient deficient core. The confocal images also reveal the 3-dimensional geometry of the spheroid showing a hemisphere shaped object rather than a spheroid (Figure 5.1). The geometry of the spheroid was further confirmed to be spherical in shape by scanning electron microscope performed by Huang et al. using the same agarose gel gravity method with MCF-7 cells[176].

5.3.3. Drug penetration

One of the most widely known extracellular barriers regarding anti-cancer drugs is uptake into the tumor due to the high intratumoral pressure and extracellular matrix[175,177]. As mentioned previously, 2-D models have limited ability in predicting the efficacy of anti-cancer drugs *in-vivo*, therefore we investigated the ability of the PAHM long-chain and short-chain polymers to penetrate T98 tumor spheroids, by labeling the polymers with an Alexa Fluor 594 fluorophore (Figure 5.2). We investigated whether the AF-594 labeled PAHM was able to achieve similar drug penetration into T98 glioblastoma spheroid as DOX-HCl. The T98 spheroids were treated with a concentration of 40 μg/mL for $PAHM_{100}$, $PAHM_{18}$, or DOX-HCl 1 hour prior to imaging. Figure 5.2 shows medial z-slices taken by confocal microscopy of the spheroids as well as the fluorescence overlay depicting the drug penetration. Penetration of the DOX-HCl was limited to the outer region of the spheroid, which is similar to other reports studying the penetration of DOX-HCl into spheroids, which were primarily inhibited by the high interstitial pressure[178]. In the case of the PAHM polymers, the red fluorescence of both

$PAHM_{18}$ and $PAHM_{100}$ is found further within the outer cell perimeter suggesting that PAHM may offer improved spheroid penetration compared to DOX-HCl in T98 based spheroids due to its increased water solubility (Figure 5.2).

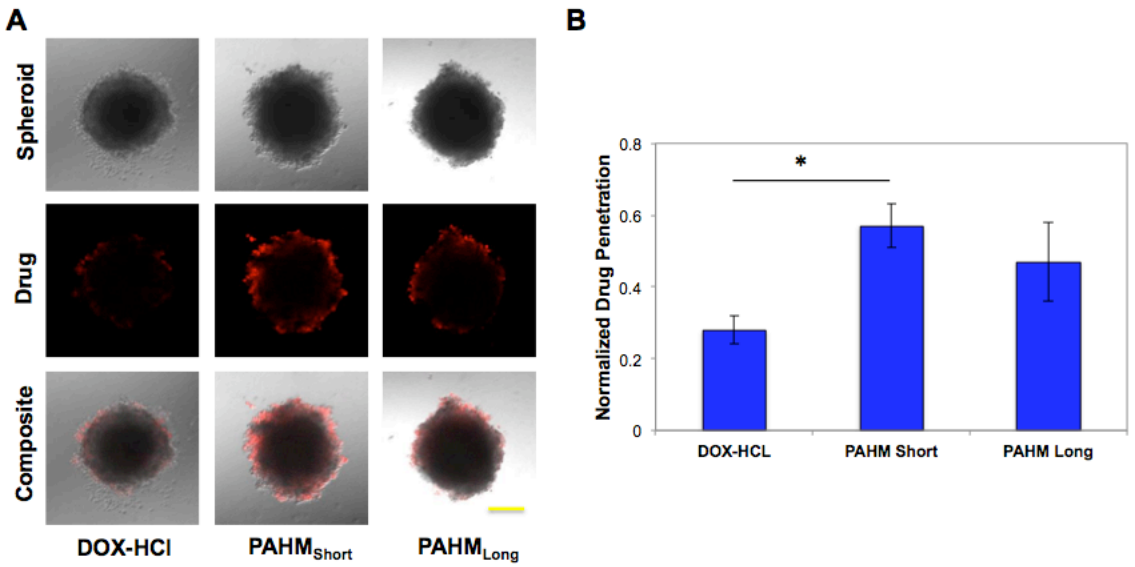

Figure 5.2. Anti-cancer drug penetration. (**a**) Confocal images of DOX-HCl, $PAHM_{18}$, and $PAHM_{100}$ fluorescence penetration into T98 spheroids at a concentration of 40 μg/mL. The PAHM polymers were previously labeled with an Alexa Fluor 594 fluorophore. All images were captured using a 10x/0.25 NA. Scale bar = 200 μm. (**b**) Quantification of fluorescently labeled anti-cancer drugs in T98 spheroids. Data represents normalized mean ± standard deviation. Statistical analysis was performed using a Student's t-test, (* $p < 0.05$, ** $p < 0.01$, # $p < 0.001$).

5.3.4. Spheroid cytotoxicity

The potential use of PAHM as an anti-cancer drug has shown promise with heightened cytotoxicity in multiple cancer cell lines (Table 5.1) and enhanced drug penetration in T98 spheroids (Figure 5.2). Therefore, we wanted to investigate the effects of long-term PAHM treatment in T98 spheroids. T98 spheroids were treated with increasing concentrations of the PAHM polymer with varying chain lengths of 18 (short), 38 (medium), and 100 (long) repeating units over the course of 28 days (Figure 5.3). Post-treatment of the spheroids with PAHM resulted in a decrease in the normalized area of the spheroids with increasing concentration regardless of the chain length. However,

at a concentration of 40 µg/mL and higher a chain length dependency becomes visible, where the smallest chain length $PAHM_{18}$ produces the largest change in spheroid area over time (Figure 5.3). The enhanced toxicity of the smaller molecular weight PAHM polymers is most likely given that smaller molecular weights have an improved permeability into tumors[165,176,179,180]; however, attempts to quantify the effective diameter of these polymers has been fruitless due to the small size. It is noteworthy to point out that despite having limited spheroid reduction capabilities, $PAHM_{100}$ inhibits spheroid growth at lower concentrations (1 µg/mL) than either $PAHM_{38}$ or $PAHM_{18}$. Despite the improved toxicity of the smaller PAHM polymers, the overall spheroid area reached a steady state within the first 24 to 48 hours post initial drug dosing this may be a result of PAHM not being able to penetrate into the necrotic core of the spheroid, as seen with the drug penetration study (Figure 5.2), and the fact that only the necrotic spheroid core remained after 7 days of treatment (Figure 5.3).

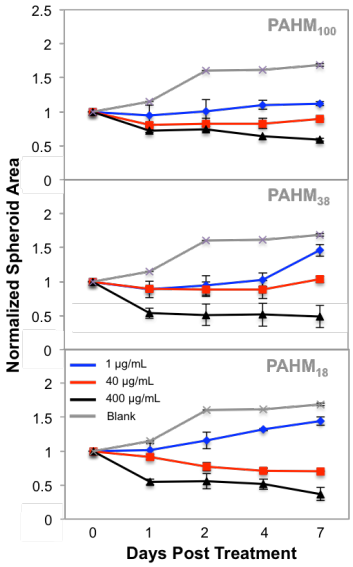

Figure 5.3. Anti-cancer drug toxicity of T98 spheroids. Quantification of optical microscopy images using ImageJ. All images were captured using a 10x/0.25 NA. Scale bar = 200 µm.

Interestingly, the toxicity of doxorubicin in the spheroids is minimal, specifically since the normalized area of the spheroids is increasing with DOX-HCl concentration and time (Figure 5.3B). This increase is likely due to the fact that glioblastoma is widely known to be multi-drug resistant (MDR) to a number of chemotherapeutic drugs including doxorubicin[170]. Yet, the overall size of the DOX-treated spheroids is larger than that of the non-treated control; likely a result of the DOX destabilizing the outer extracellular matrix of the spheroid allowing for the cells to fall to the bottom of the cell culture/agarose plate where proliferation continues (Figure 5.3A).

5.3.5. In-vivo tumor challenge

Establishment of an *in-vivo* murine breast cancer model was carried out by injection of EMT-6 cells under the left bottom flank of 14-week old female Balb/C mice. Following incubation of 7-8 days post initial injection, the tumor were challenged with PBS or $PAHM_{18}$ at a concentration of 3.6 or 9.1 mg/kg via intratumoral (I.T.) injection. The injections of either PAHM or PBS was followed up every forth day and the I.T. injection location varied, allowing for proper healing of the skin layer minimizing the leakage of the PAHM or PBS from the tumor.

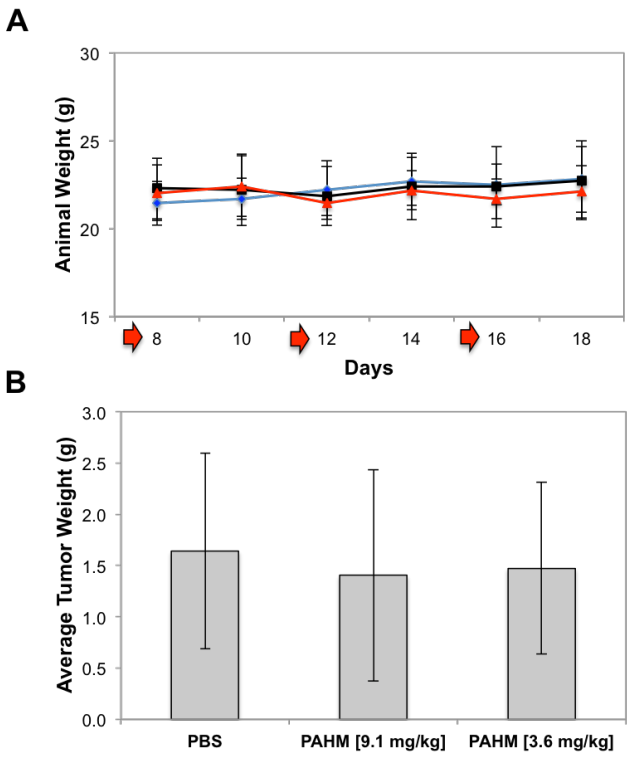

Figure 5.4. Animal body weight and average tumor weight. (**a**) Average animal body weight of Balb/C mice injected with EMT-6 over the course of PAHM and PBS injections. (**b**) Average dry tumor weight of explanted tumors from PAHM and PBS treatment groups. Data represents the mean ± standard deviation of N=10 for each group. Statistical analysis was performed using a Student's t-test, (* $p < 0.05$, ** $p < 0.01$, # $p < 0.001$).

The body weight of each treatment group was recorded and showed that neither the high or low concentration PAHM or PBS treatment groups affected the mouse weight (Figure 5.4), suggesting that the PAHM treatment offered limited systemic cytotoxicity due to the limited escape from the tumor. Measurement of the tumor volume resulted in minimal tumor regression for the either the PAHM or PBS treatment groups (Figure 5.5A,B,C). The overall mean tumor volume of either PAHM concentration offered similar tumor size to that of the PBS control (Figure 5.5D).

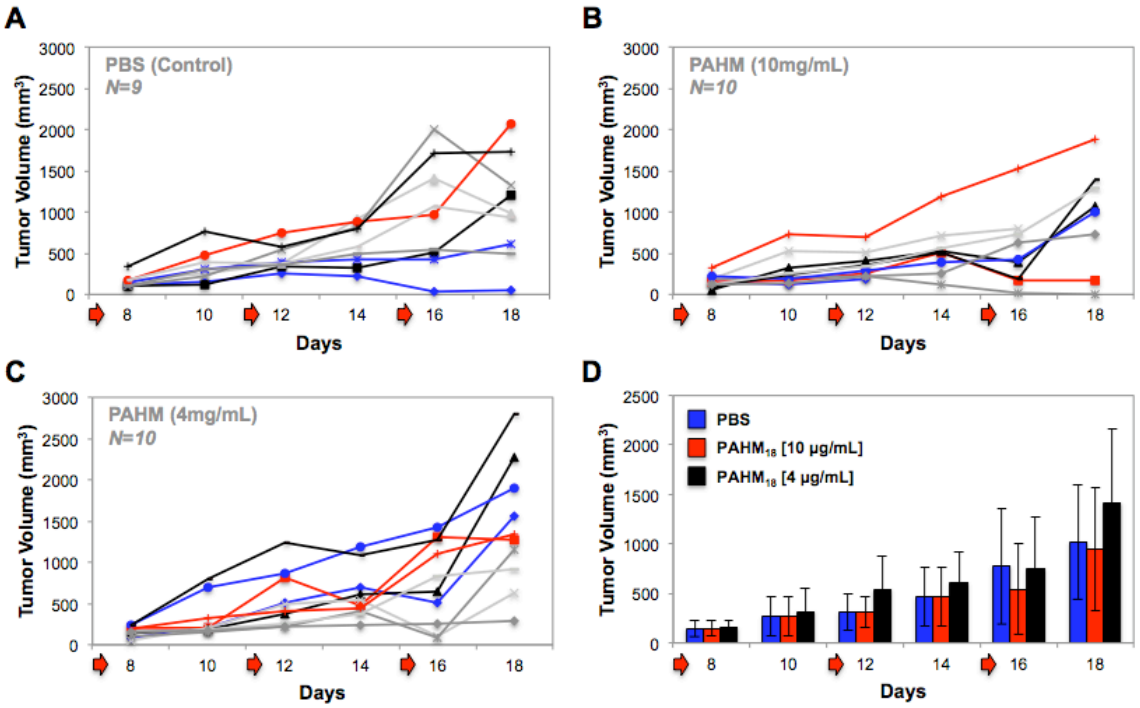

Figure 5.5. Quantification of EMT-6 tumor volume post intratumoral injection in-vivo. Individual tumor volume for each experimental group (**a**) PBS, (**b**) $PAHM_{18}$ [9.1 mg/kg] and (**c**) $PAHM_{18}$ [3.6 mg/kg]. (**d**) Cumulative analysis of between each drug treatment group. Data represents the mean ± standard deviation of *N*=10 for each group. Red arrows indicate days of injection. Statistical analysis was performed using a Student's t-test, (* $p < 0.05$, ** $p < 0.01$, # $p < 0.001$).

However, post-experimental harvesting of the EMT-6 tumor showed increased intratumoral decay for the PAHM [3.6 mg/kg] treatment groups compared to that of the PAHM [9.1 mg/kg] and PBS control. These findings suggest that the PAHM is localizing within the center of the tumor and has an inability to escape to the surrounding tumor tissue, which may be a result of the elevated intratumoral pressure[175,177].

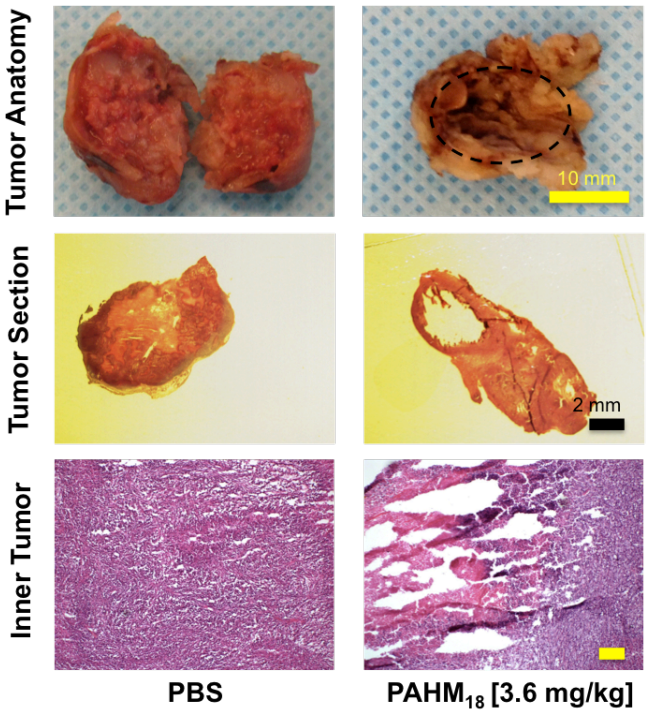

Figure 5.6. EMT-6 tumor histology. Images of explanted tumor size and morphology as well as H&E staining for characterization of intratumoral tissue. Black dotted lines separate the inner core of the tumor form the outer normal region. Tumor section shows area void of cancer cells for the PAHM experimental group. Images are representative of *N*=10 for each group. Scale bar = 10 mm (upper panel), 2 mm (middle panel) and 200 μm (lower panel).

Moreover, despite the intratumoral toxicity of PAHM, the outer region of the tumor is unchanged thus allowing the tumor to continue grow (Figure 5.6). This explains why the PAHM and PBS treatment groups have similar overall tumor volume and weight (Figure 5.5). Histology slices of explanted EMT-6 tumors showed that the make-up of the PAHM [3.6 mg/kg] treated tumor possessed void in the cell density within the center of the tumor than that of the PBS treatment group again supporting the fact that PAHM was toxic to the intratumoral region of the tumor, yet was inhibited by poor diffuse into the extracellular space (Figure 5.6). The biodistribution of the PAHM polymers show little systemic activity in the surrounding spleen, liver, or lung tissue (Figure 5.7).

However, the density of the kidney tissue is compromised for the PAHM [3.6 mg/kg], suggesting that some quantity of the PAHM is leaving the tumor and entering into the blood stream.

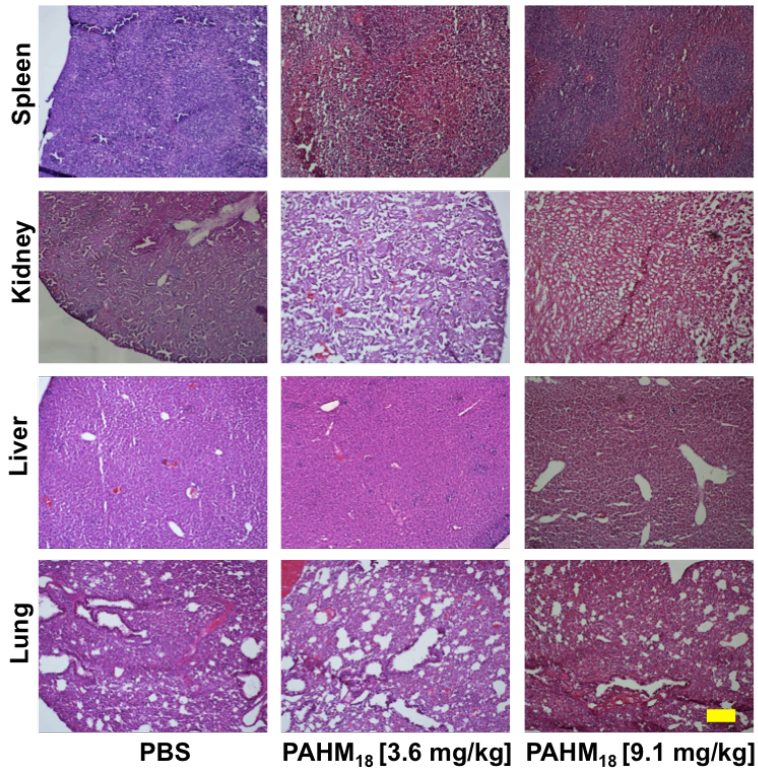

Figure 5.7. Histology slices representing explanted systemic organs; spleen, kidney, liver, lungs of EMT-6 treatment mice. Images are representative of *N*=10 for each group. Scale bar = 200 μm.

5.3.6. Live animal imaging

Despite signs showing that PAHM is not causing severe systemic toxicity due to the animals not exhibiting a fluctuation in body weight (Figure 5.4) as well as minimal tissue damage as seen with histology (Figure 5.7). We wanted to investigate the potential for biodistribution of the low concentration PAHM within the tumor and the mouse peripheral tissue. A 14 week old female Balb/C mouse possessing an EMT-6 tumor was injection I.T. with a Alexa Fluor 750 (AF750) fluorophore labeled PAHM polymer in accordance with the original in-vivo tumor challenge study and viewed by live animal

imaging over the course of 11 days. As shown in figure 5.8 the distribution of the PAHM-AF750 polymer does not leave the tumor within the first 30 minutes post initial injection, by 24 hours the fluorescence of the injected PAHM is localized within the tumor. By day 4 the initial fluorescence of the PAHM-AF750 labeled has decreased possibly do to metabolism or quenching of the AF750 signal by thickening of the tumor wall. However, immediately following the booster injection the fluorescence level returns to a similar level seen after the initial injection.

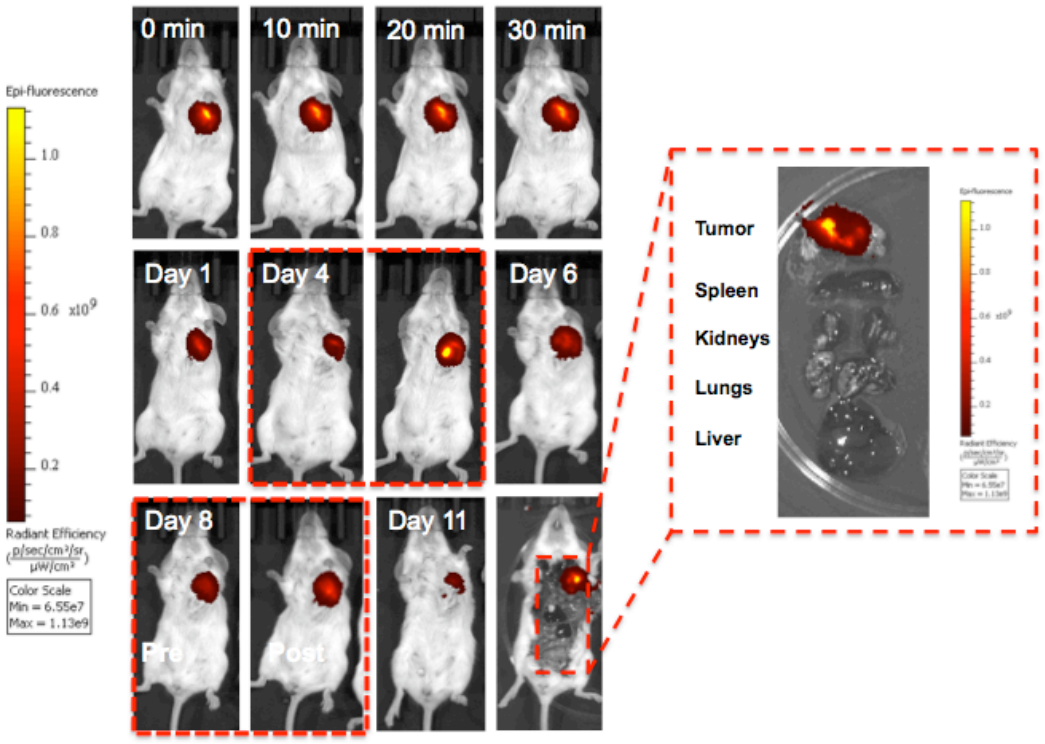

Figure 5.8. $PAHM_{18}$ live animal imaging. Biodistribution of Alexa Fluor 750 labeled $PAHM_{18}$ at a dosage of 3.6 mg/kg in EMT-6 bearing female Balb/C mice. The red squares surrounding the day 4 and 8 time points represent images prior to (left) and post (right) booster injection.

By day 11 the fluorescence is maintained within the tumor boundaries and no fluorescent signal is seen within the mouse periphery or systemic organs, suggesting that the PAHM is localized within the tumor (Figure 5.8). This is interesting since tumors are

known to have high rates of angiogenesis[172]. However, the drug never leaves the tumor suggesting that the tumor may be exhibiting low levels of angiogenesis, which has shown to increase intratumoral drug retention[181]. Dissection of the mouse revealed this to be the case, by showing that none of the harvested organs fluoresce red except the tumor, again showing that the PAHM-Cy7 was localized within the tumor boundaries (Figure 5.8). No signal was seen within the blood, which still does not rule out the possibility of the PAHM polymer being in the blood due to a potentially weak signal. A better indicator of PAHM presence in the blood would be to measure the level of hemoglobin in the blood, due to the lysing of red blood cells by PAHM.

5.4. Conclusions

In this work we synthesized a linear cationic polymer poly (6-amino-1-hexyl methacrylate) (PAHM) that has shown to be cytotoxic to a number of human breast and glioblastoma multidrug resistant cell lines. Anti-cancer drug screening in T98 tumor spheroids showed that PAHM has better cytotoxicity than commonly used chemotherapeutics such as doxorubicin. *In-vivo* intratumoral injections of PAHM into EMT-6 breast cancer bearing mice showed minimal tumor volume reduction, but higher amounts of tissue disruption compared to PBS controls, while also exhibiting minimal systemic toxicity. This work is the first of its kind evaluating the use of linear cationic polymers for use as anti-cancer drugs. Despite the inability to reduce the overall tumor volume *in-vivo*, PAHM has shown great potential to be used as an anti-cancer drug in multidrug resistant cancer cell lines and offers a springboard for future research in this field.

Chapter 6: Conclusions and Future Perspectives

6.1. Well-defined Chain Length for DNA Vaccines

Our work with poly(2-aminoethyl methacrylate) (PAEM) synthesized with narrow molecular weight and polydispersity allowed us to investigate the role chain length plays on transfection efficiency of dendritic cells as it relates to subcellular trafficking. PAEM polymers synthesized at small (45), medium (75), and long (150) repeating units showed that moderate and long-chain PAEM polymers offered higher transfection efficiency compared to the smaller PAEM polymer. Investigation into the relationship of the polymer chain length and subcellular trafficking allowed us to conclude that a number of subcellular processes are chain length dependent. Cellular uptake and complex dissociation of PAEM showed higher amounts of medium-and longer-chain PAEM were taken up into dendritic cells. Also, a higher percentage of DNA plasmid was still complexed to the longer-chain PAEM compared to the shorter-chain PAEM, which displayed the highest degree of dissociation. Nuclear uptake showed the same trend where the medium and longer-chain length PAEM resulted in higher total nuclear uptake, yet the longer chain polymer again inhibited DNA complex dissociation within the nucleus. From this work we were able to show that polymer molecular weight is a simple yet necessary characteristic to consider when designing linear cationic polymers for use in DNA vaccines. Fine-tuning of the polymer molecular weight can improve specific polymer/cell interactions such as increase cellular uptake, lower complex dissociation, and heighten nuclear uptake.

In order to improve on the all-around scope, further work should be done on understanding the translation of polymer molecular weight in different antigen-presenting cell lines, such as macrophages[11]. This will further help with understanding the effect of polymer molecular weight (chain length) on subcellular trafficking and overall transfection efficiency. Designing a cationic system which is fine-tuned for robust transfection of both dendritic cells and macrophages, may translate to improved cellular uptake and transfection *in-vivo*.

6.2. Structure-function Mechanisms of Polymer Vectors for Delivery to Dendritic Cells

The focus of this work was to further investigate the role of polymer structure on transfection efficiency and subcellular trafficking in dendritic cells. Because of the similarity in polymer structure between PAEM and poly(l-lysine) (PLL), a polymer which has been documented to be frequently trapped within the endolysosomal vesicles, we wanted to investigate why PAEM is able to transfect dendritic cells. From this work we were able to deduce that the main difference between PAEM and PLL is primarily a result of differences in the route of endocytotic uptake. The use of Filipin III, a lipid raft/caveolae inhibitor, resulted in an overall decrease in transfection efficiency of PAEM as a result of decreased cellular and nuclear uptake. The main conclusion from this work is that simple differences in polymer chemical structure may lead to differences in hydrophobicity and polymer size and shape; which may affect the polymer/cell interaction, specifically endocytotic routing of the polymer complexes.

Future directions for this work involve a number of different experiments looking into the overall difference in hydrophobicity of these two linear cationic polymers. First,

a simple polymer hydrophobicity assay, or partition assay, can be performed to quantify the hydrophobicity of the PAEM and PLL. However, this assay does not tell us specifics of chemical structure and how they relate to hydrophobicity. Therefore, more work needs to be done in understanding the interaction of the polymer in aqueous environments, such as polymer folding and determination of hydrophobic and hydrophilic regions. Yet, this again does not offer the complete story as to the polymer complex and cell interaction. Moreover, a better understanding of the polymer-DNA plasmid interaction needs to be investigated and the behavior of these polymer complexes in aqueous environments would be ideal[182]. From this work, better polymer design can be established due to better knowledge of how polymer complex hydrophobicity leads to specific cell interactions and the possibility of improved cellular uptake and transfection efficiency *in vivo*.

6.3. Effect of Dendritic Cell Type and Maturation on Transfection Efficiency

The purpose of this work was to understand the potential subcellular barriers inhibiting transfection of primary bone marrow-derived dendritic cells (BMDC). In this work we saw that the overall subcellular trafficking of BMDC was significantly different than DC 2.4 dendritic cells. The cellular and nuclear uptake of BMDC was significantly lower than DC 2.4 dendritic cells. Upon further investigation into the potential differences between these two dendritic cell lines, we found that DC 2.4 cells were previously transfected and are potentially in a state of activation and maturation. Maturation of BMDC with lipopolysaccharides (LPS), improved the percentage of GFP positive cells, yet the mean fluorescent intensity of these cells was still low. The main

take away from this work is that the degree of dendritic cell maturation may help improve the transfection efficiency of primary bone marrow-derived dendritic cells, and that the main limiting barriers of BMDC may be further downstream from subcellular trafficking, such as DNA transcription and translation.

Further advancement into understanding the effects of gene transcription and translation are needed to effectively conclude that BMDC maturation increases transfection. Experiments focusing on RT-PCR of the GFP mRNA sequence can be performed to quantify the levels of DNA plasmid transcription in BMDC at different maturation levels. A better understanding of the PAEM polymer cell interaction, such as endocytotic uptake pathways, can be measured and quantified by western blot specifically looking at caveolae (Cav-1) and clathrin mediated endocytosis (clathrin or dynamin-2)[70]. This may help distinguish which pathway PAEM is utilizing in BMDC and modifications to the polymer chemical structure can be made to specifically target lipid raft/caveolae mediated endocytosis pathways.

6.4. Cationic Polymer Toxicity in *In-vitro* and *In-vivo* Models

The work with poly (6-amino-1-hexyl methacrylate) (PAHM) as an anti-cancer agent showed that linear hydrophobic polymers can be used as potential anti-cancer drugs. PAHM showed high levels in cytotoxicity in 2-D cell culture and 3-D spheroid tumor models. Yet, the efficacy of PAHM to eliminate the hypoxia/necrotic core is limited. Moreover, it would be ideal to incorporate PAHM with a hypoxia toxic drug, such as tirapazamine (TPZ)[183], in order to improve the overall efficacy of PAHM as an anti-cancer drug. Unfortunately, the efficacy of PAHM in *in-vivo* EMT-6 models is

insufficient. However, this might be more specific of the tumor model itself and not an indication of PAHM efficacy. Other anti-cancer drug models using EMT-6 cells have shown similar levels of cell growth without recession, possibly stemming from the fact that EMT-6 cells are very proficient in repairing cell damage due to radiation and other anti-cancer cell therapies[184]. Therefore, more work needs to be done *in-vivo* using a more established tumor model such as B16-F10 melanoma models[185]. This model is an improvement over EMT-6 since first it has the potential to metastasize to systemic organs offering a better model to test the tumor suppression properties of potential anti-cancer drugs.

References

[1] Vaccine-Preventable Diseases, World Health Organization (WHO), http://www.who.int/immunization_monitoring/diseases/en/ (accessed 4 January 2009).

[2] Romani, N., Thrunher, M., Idoyaga, J., Steinman, R.M., Flacher, V. (2010). Targeting of antigens to skin dendritic cells: possibilities to enhance vaccine efficacy. *Immunology and Cell Biology*, 88, 424-430.

[3] Nguyen, D. H., Green, J. J., Chan, J. M., Langer, R., & Anderson, D. G. (2008). Polymeric materials for gene delivery and DNA vaccination. *Advanced Materials, 20*, 1.

[4] Robinson, H.L. (2007). HIV/AIDS Vaccines: 2007. Clinical Pharm. & Therap. 82, 6, 686-693.

[5] Rice, J., Ottensmeier, C., & Stevenson, F. (2008). DNA vaccines: Precision tools for activating effective immunity against cancer. *Nature Reviews, 8*, 108.

[6] Bachmann, M.F., Jennings, G.T. (2010). Vaccine delivery: a matter of size, geometry, kinetics and molecular patterns. *Nature Reviews: Immunology*. 10, 787-796.

[7] Jones, D. H., McDonald, S. C., Clegg, J. C. S., & Farrar, G. H. (1997). Poly(DL-lactide-co-glycolide)-encapsulated plasmid DNA elicits systemic and mucosal antibody responses to encoded protein after oral administration. *Vaccine, 15*(8), 814.

[8] Nestle, F.O. (2006). A new lease on life for dendritic cell vaccines. *Nature Biotechnology, 24*(12), 1483.

[9] Malmberg, K. J. (2004). Effective immunotherapy against cancer. *Cancer Immunol Immunother, 53*, 879.

[10] Greenland, J.R., Letvin, N.L. (2007). Chemical adjuvants for plasmid DNA vaccines. Vaccine, 25, 3731-3741.

[11] Banchereau, J., & Palucka, A. K. (2005). Dendritic cells as therapeutic vaccines against cancer. *Nature Reviews - Immunology, 5*, 296.

[12] Croci, D., Fluck, M., Rico, M., Matar, P., & Rabinovich, G. (2007). Dynamic cross-talk between tumor and immune cells in orchestrating the immunosuppressive network at the tumor microenvironment. *Cancer Immunol Immunother, 56*, 1687.

[13] Tacken, P. J., de Vries, J. M., Torensma, R., & Figdor, C. G. (2007). Dendritic cell immunotherapy: From ex vivo loading to in vivo targeting. *Nature Reviews - Immunology, 7*, 790.

[14] Faith, A., & Hawrylowicz, C. M. (2005). Targeting the dendritic cell: The key to immuntotherapy in cancer? *Clinical and Experimental Immunology, 139*(395)

[15] Banchereau, J., & Steinman, R. M. (1998). Dendritic cells and the control of immunity. *Nature, 392*, 245.

[16] Rabinovich, G. A., Gabrilovich, D., & Sotomayor, E. M. (2007). Immunosuppressive strategies that are mediated by tumor cells. *Annu Rev Immunolo, 25*, 267.

[17] Shortman, K., & Naik, S. H. (2007). Steady-state and inflammatory dendritic-cell development. *Nature Reviews - Immunology, 7*, 19.

[18] Randolph, G. J., Veronique, A., & Swartz, M. A. (2005). Dendritic-cell trafficking to lymph nodes through lymphatic vessels. *Nature Reviews - Immunology, 5*, 617

[19] Onaitis, M., Kalady, M., Pruitt, S., & Tyler, D. (2002). Dendritic cell gene therapy. *Surg. Oncol. Clin. N. AM, 11*, 645.

[20] Wilson-Welder, J. H., Torres, M. P., Kipper, M. J., Mallapragada, S. K., Wannemuehler, M. J., & Narasimhan, B. (2008). Vaccine adjuvants: Current challenges and future approaches. *Journal of Pharmaceutical Sciences, 8*, 1.

[21] Babensee, J. E. (2008). Interaction of dendritic cells with biomaterials. *Seminars in Immunology, 20*, 101.

[22] Hickman-Miller, H. D., & Yewdell, J. W. (2006). Youth has its privileges: Maturation inhibits DC cross-priming. *Nature Immunology, 7*(2), 125.

[23] Little, S. R., & Langer, R. (2005). Nonviral delivery of cancer genetic vaccines. *Adv Biochem Engin/Biotechnol, 99*, 93.

[24] Hu, Y., Litwin, T., Nagaraja, A., Kwong, B., Katz, J., Watson, N., et al. (2007). Cytosolic delivery of membrane-impermeable molecules in dendritic cells using pH-responsive core-shell nanoparticles. *Nano Letters, 7*(10), 3056.

[25] Jilek, S., Merkle, H., & Walter, E. (2005). DNA-loaded biodegradable micrparticles as vaccine delivery systems and their interaction with dendritic cells. *Advanced Drug Delivery Reviews, 57*, 377.

[26] Kasturi, S., Sachaphibulkij, K., & Roy, K. (2005). Covalent conjugation of polyethyleneimine on biodegradable micrparticles for delivery of plasmid DNA vaccines. *Biomaterials, 26*, 6375.

[27] Chang, C. W., Choi, D., Kim, W. J., Yockman, J. W., Christensen, L. V., Kim, Y. H., et al. (2007). Non0ionic amphiphilic biodegradable PEG-PLGA-PEG copolymer enhances gene delivery efficiency in rat skeletal muscle. *Journal of Controlled Release, 118*, 245.

[28] Collins, S. A., Guinn, B., Harrison, P. T., Scallan, M. F., O'Sullivan, G. C., & Tangney, M. (2008). Viral vectors in cancer immunotherapy: Which vector for which strategy? *Current Gene Therapy, 8*(2), 66.

[29] Pack, D. W., Hoffman, A. S., Pun, S., & Stayton, P. S. (2005). Design and delivery of polymers for gene delivery. *Nature Reviews - Drug Delivery, 4*, 581.

[30] Diez, S., & Tros de Ilarduya, C. (2006). Versatility of biodegradable poly(DL-lactide-co-glycolic acid) microspheres for plasmid DNA delivery. *Eurpoean Journal of Pharmaceutics and Biopharmaceutics, 63*, 188.

[31] Ando, S., Putnam, D., Pack, D., & Langer, R. (1999). PLGA microspheres containing plasmid DNA: Preservation of supercoiled DNA via cryopreparation and carbohydrate stabilization. *Journal of Pharmaceutical Sciences, 88*(1), 126.

[32] Akinc, A., Thomas, M., Klibanov, A., & Langer, R. (2005). Exploring polyethylenimine-mediated DNA transfection and the proton sponge hypothesis. *Journal of Gene Medicine, 7*, 657.

[33] McKeever, U., Barman, S., Hao, T., Chambers, P., Song, C., Lunsford, L., et al. (2002). Protective immune responses elicited in mice by immunization with formulations of poly(lactide-co-glycolide) microparticles. *Vaccine, 20*, 1524.

[34] Wang, L., Chaw, C. S., Yang, Y. Y., Moochhala, S. M., Zhao, B., Ng, S., et al. (2004). Preparation, characterization, and in vitro evaluation of physostigmine-loaded poly(ortho ester) and poly(ortho ester)/poly(D,L-lactide-co-glycolide) blend microspheres fabricated by spray drying. *Biomaterials, 25*, 3275.

[35] Hanes, J., Cleland, J. L., & Langer, R. (1997). New advances in microsphere-based single-dose vaccines. *Advanced Drug Delivery Reviews, 28*, 97.

[36] Gunatillake, P. A., & Adhikari, R. (2003). Biodegradable synthetic polymers for tissue engineering. *Eurpoean Cells and Materials, 5*, 1.

[37] Zolnik, B. S., & Burgess, D. J. (2007). Effect of acidic pH on PLGA microsphere degradation and release. *Journal of Controlled Release, 122*, 338.

[38] Brannon-Peppas, L., Ghosn, B., Roy, K., & Cornetta, K. (2007). Encapsulation of nucleic acids and opportunities for cancer treatment. *Pharmaceutical Research, 24*(4), 618.

[39] Park, T. G. (1995). Degradation of poly(lactic-co-glycolic acid) microspheres: Effect of copolymer composition. *Biomaterials, 16*, 1123.

[40] Walter, E., Moelling, K., Pavlovic, J., & Merkle H. (1999). Microencapsulation of DNA using poly(DL-lactide-co-glycolide) stability issues and release characteristics. *Journal of Controlled Release, 61*, 361.

[41] Walter, E., Dreher, D., Menno, K., Thiele, L., Kiama, S. G., Gehr, P., et al. (2001). Hydrophilic poly(DL-lactide-co-glycolide) microspheres for the delivery of DNA to human0derived macrophages and dendritic cells. *Journal of Controlled Release, 76*, 149.

[42] Walter, E., Dreher, D., Kok, M., Thiele, L., Kiama, S. G., Gehr, P., et al. (2001). Hydrophilic poly(-lactide-co-glycolide) microspheres for the delivery of DNA to human-derived macrophages and dendritic cells. *Journal of Controlled Release, 76*(1-2), 149.

[43] Li, M., Rouaud, O., & Poncelet, D. (2008). Microencapsulation by solvent evaporation: State of the art for process engineering approaches. *International Journal of Pharmaceutics, 363*(1-2), 26.

[44] Van de Weet, M., Hennink, W. E., & Jiskoot, W. (2000). Protein instability in poly(lactic-co-glycolic acid) microspheres. *Pharmaceutical Research, 17*, 1159.

[45] Lengsfeld, C. S., Manning, M. C., & Randolph, T. W. (2002). Encapsulating DNA within biodegradable polymeric microparticles. *Current Pharmaceutical Biotechnology, 3*(3), 227.

[46] Eliyahu, H., Barenholz, Y., & Domb, A. J. (2005). Polymers for DNA delivery. *Molecules, 10*, 34.

[47] Cho, Y. W., Kim, J., & Park, K. (2003). Polycation gene delivery systems: Escape from endosomes to cytosol. *Journal of Pharmacy and Pharmacology,* , 721.

[48] Jeong, J. H., & Park, T. G. (2002). Poly(-lysine)-g-poly(-lactic-co-glycolic acid) micelles for low cytotoxic biodegradable gene delivery carriers. *Journal of Controlled Release, 82*(1), 159.

[49] Zauner, W., Ogris, M., & Wagner, E. (1998). Polylysine-based transfection systems utilizing receptor-mediated delivery. *Advanced Drug Delivery Reviews, 30*(1-3), 97.

[50] Cristiano, R. J. (2002). Protein/DNA polyplexes for gene therapy. *Surg. Oncol. Clin. N. AM, 11*, 697.

[51] Boussif, O., Lezoualc'h, F., Zanta, M. A., Mergny, M. D., Scherman, D., Demeneix, B., et al. (1995). A versatile vector for gene and oligonucleotide transfer into cells in culture and in vivo: Polyethylenimine. *Proc. Natl. Acad. Sci., 92*, 7297.

[52] Akinc, A., Thomas, M., Klibanov, A., & Langer, R. (2005). Exploring polyethylenimine-mediated DNA transfection and the proton sponge hypothesis. *Journal of Gene Medicine, 7*, 657.

[53] Fischer, D., Bieber, T., Li, Y., Elsasser, H. P., & Kissel, T. (1999). A novel non-viral vector for DNA delivery based on low molecular weight, branched polyethylenimine: Effect of molecular weight on transfection efficiency and cytotoxicity. *Pharmaceutical Research, 12*(8), 1273.

[54] Shim, M. S., & Kwon, Y. J. (2008). Controlled delivery of plasmid DNA and siRNA to intracellular targets using ketalized polyethylenimine. *Biomacromolecules, 9*, 444.

[55] Ahn, C., Chae, S. Y., Bae, Y. H., & Kim, S. W. (2002). Biodegradable poly(ethylenimine) for plasmid DNA delivery. *Journal of Controlled Release, 80*(1-3), 273.

[56] Forrest, M. L., Koerber, J. T., & Pack, D. W. (2003). A degradable polyethylenimine derivative with low toxicity for highly efficient gene delivery. *Bioconjugate Chemistry, 14*(5), 934.

[57] Gosselin, M. A., Guo, W., & Lee, R. J. (2001). Efficient gene transfer using reversibly cross-linked low molecular weight polyethylenimine. *Bioconjugate Chemistry, 12*(6), 989.

[58] Kim, Y. H., Park, J. H., Lee, M., Kim, Y., Park, T. G., & Kim, S. W. (2005). Polyethylenimine with acid-labile linkages as a biodegradable gene carrier. *Journal of Controlled Release, 103*(1), 209.

[59] Green, J., Shi, J., Chiu, E., Leshchiner, E., Langer, R., & Anderson, D. (2006). Biodegradable polymeric vectors for gene delivery to human endothelial cells. *Bioconjugate Chem, 17*, 1162.

[60] Devalapally, H., Shenoy, D., Little, S., Langer, R., & Amiji, M. (2007). Poly(ethylene oxide)-modified poly(beta-amino ester) nanoparticles as a pH-sensitive system for tumor targeted delivery of hydrophobic drugs: Part 3. therapeutic efficacy and safety studies in ovarian cancer xenograft model. *Cancer Chemother Pharmacol, 59*, 477.

[61] Lynn, D. M., Anderson, D. G., Putnam, D., & Langer, R. (2001). Accelerated discovery of synthetic transfection vectors: Parallel synthesis ad screening of a degradable polymer library. *J. Am. Chem. Soc., 123*, 8155.

[62] Lynn, D. M., & Langer, R. (2000). Degradable poly(beta-amino ester): Synthensis, characterization, and self-assembly with plasmid DNA. *J. Am. Chem. Soc., 122*, 10761.

[63] Zugates, G. T., Tedford, N. C., Zumbuehl, A., Juhnjhunwala, S., Kang, C. S., Griffith, L. G., et al. (2007). Gene delivery properties of end-modified poly(beta-amino ester)s. *Bioconjugate Chem., 18*, 1887.

[64] Lynn, D. M., Amiji, M. M., & Langer, R. (2001). pH-responsive polymer microspheres: Rapid release of encapsulated material within the range of intracellular pH. *Angew Chemie Int Ed, 40*(9), 1707.

[65] Anderson, D., Akinc, A., Hossain, N., Langer, R. (2005). Structure/property studies of polymeric gene delivery using a library of poly(beta-amino esters). *Molecular Therapy, 11*(3), 426.

[66] Luten, J., van Nostrum, C. F., De Smedt, S. C., Hennink, W. E. (2008). Biodegradable polymers as non-viral carriers for plasmid DNA delivery. *Journal of Controlled Release, 126*(2), 97-110.

[67] Little, S., Lynn, D., Ge, Q., Anderson, D., Puram, S., Chen, J., et al. (2004). Poly-beta amino ester-containing microparticles enhance the activity of nonviral genetic vaccines. *PNAS, 101*(26), 9534.

[68] Wood, K., Little, S. R., Langer, R., Hammond, P. (2005). A family of hierachically self-assembling linear-denritic hybrid polymers for highly efficient targeted gene delivery. *Angew. Chem. Int. Ed., 44*, 6704.

[69] Leong, K.W. (2005). Polymeric Controlled Nucleic Acid Delivery. *MRS Bulletin, 30*, 640.

[70] Khalil, I.A., Kogure, K., Akita, H., Harashima, H. (2006). Uptake Pathways and Subsequent Intracellular Trafficking in Nonviral Gene Delivery. *Pharamacological Reviews, 58, 1,* 32.

[71] Grigsby C. L., Leong, K. W. (2010). Balancing protection and release of DNA: tools to address a bottleneck of non-viral gene delivery. *J. R. Soc., Interface*, 7, S67–S82

[72] Lechardeur, D., Verkman, A.S., Luckacs, G.L. (2005). Intracellular Routing of Plasmid DNA during Non-viral gene transfer. *Advanced Drug Delivery Reviews, 57,* 755.

[73] Won, Y.Y., Sharma, R., Konieczny, S.F. (2009). Missing pieces in understanding the intracellular trafficking of polycation/DNA complexes. *Journal of Controlled Release, 139,* 88.

[74] Ma, H., Diamond, S. L. (2001). Nonviral gene therapy and its delivery systems. *Current Pharmaceutical Biotechnology, 2*, 1.

[75] Rejman, J., Oberle, V., Zuhorn, I., Hoekstra, D. (2004). Size-dependent internalization of particles via the pathways of clathrin- and caveolae-mediated endocytosis. *Biochem J. 377, 1,* 159.

[76] Conner, S., Schmid, S. (2003). Regulated portals of entry into the cell. *Nature, 422, 6927,* 37.

[77] Maxfield, F.R., McGraw, T.E. (2004). Endocytic recycling. N*at Rev Mol Cell Biol.* 5: 121-32.

[78] Heller, J., Barr, J., Ng, S. Y., Abdellauoi, K. S., Gurny, R. (2002). Poly(ortho esters): Synthesis, characterization, properties, and uses. *Advanced Drug Delivery Reviews, 54*, 1015.

[79] Ng, S. Y., Vandamme, T., Taylor, M. S., & Heller, J. (1997). Synthesis and erosion studies of self-catalyzed poly(ortho esters). *Macromolecules, 30*, 770.

[80] De Laporte, L., Cruz Rea, J., Shea, L. D. (2006). Design of modular non-viral gene therapy vectors. *Biomaterials, 27*, 947.

[81] Godbey, W. T., Wu, K. K., & Mikos, A. G. (1999). Tracking the intracellular path of poly(ethylenimine/DNA complexes for gene delivery. *Proc. Natl. Acad. Sci., 96*, 5177.

[82] Godbey, W. T., Wu, K. K., & Mikos, A. G. (1999). Poly(ethylenimine) and its role in gene delivery. *Journal of Controlled Release, 60*(2-3), 149.

[83] Lai, W., Lin, M. C. Nucleic acid delivery with chitosan and its derivatives. *Journal of Controlled Release, In Press, Corrected Proof*

[84] Han, X., Fang, Q., Yao, F., Wang, X., Wang, J., Yang, S., Shen, B. (2009). The heterogeneous nature of polyethylenimine-DNA complex formation affects transient gene expression. *Cytotechnology*.

[85] Lucas, B., Remaut, K., Sanders, N. N., Braeckmans, K., De Smedt, S. C., & Demeester, J. (2005). Studying the intracellular dissociation of Polymer−Oligonucleotide complexes by dual color fluorescence fluctuation spectroscopy and confocal imaging†. *Biochemistry, 44*

(29), 9905-9912.

[86] Schaffer, D., Fidelman, N., Dan, N., Lauffenburger, D. (1999). Vector unpacking as a potential barrier for receptor mediated polyplex gene delivery. *Biotechnology an Bioengineering, 67, 5,* 598.

[87] Dailey, L., Kleemann, E., Merdan, T., Peterson, H, Schmehl, T., Gessler, T., Hanze, J., Seeger, W, Kissel, T. (2004). Modified polyethylenimines as non-viral gene delivery systems for aerosol therapy: effects of nebulization on cellular uptake and transfection efficiency. *Journal of Controlled Release. 100,* 425.

[88] Bieber, T., Meissner, W., Kostin, S., Niemann, A., Elsasser, H. (2002). Intracellular route and transcriptional competence of polyethylenimine-DNA complexes. *Journal of Controlled Release. 82,* 441.

[89] Grosse, S., Aron, Y., Thévenot, G., Monsigny, M., Fajac, I. (2007). Cytoskeletal involvement in the cellular trafficking of plasmid/PEI derivative complexes. *Journal of Controlled Release, 122*(1), 111-117.

[90] Akita, H., Ito, R., Khalil, I., Futaki, S., Harashima, H. (2004). Quantitative three-dimensional analysis of the intracellular trafficking of plasmid DNA transfected by a nonviral gene delivery system using confocal laser scanning microscopy. *Molecular Therapy. 9, 3,* 443.

[91] Breunig, M., Lungwitz, U., Liebl, R., Goepferich, A. (2006). Fluorescence resonance energy transfer: Evaluation of the intracellular stability of polyplexes. *European Journal of Pharm and Biopharm. 63,* 156.

[92] Itaka, K., Harada, A., Nakamura, K., Kawaguchi, H, Kataoka, K. (2002). Evaluation by fluorescence resonance energy transfer of the stability of nonviral gene delivery vectors under physiological conditions. *Biomarcomolecules, 3,* 841.

[93] Laddy, D. J., Weiner, D. B. (2006). From plasmids to protection: a review of DNA vaccines against infectious diseases.*Int. Rev. Immunol*. 25, 99−123.

[94] Mellman, I., Steinman, R. M. (2001). Dendritic cells: specialized and regulated antigen processing machines *Cell*, 106, 255−258.

[95] Rock, K. L., Shen, L. (2005). Cross-presentation: underlying mechanisms and role in immune surveillance.*Immunol. Rev*., 207, 166−183.

[96] Mintzer, M. A., Simanek, E. E. (2009). Nonviral vectors for gene delivery. *Chem. Rev*., 109, 259−302

[97] Wong, S. Y., Pelet, J. M., Putnam, D. (2007). Polymer systems for gene delivery-past, present, and future *Prog. Polym. Sci*., 32, 799−837.

[98] Layman, J. M., Ramirez, S. M., Green, M. D., Long, T. E. (2009). Influence of polycation molecular weight on poly(2-dimethylaminoethyl methacrylate)-mediated DNA delivery in vitro. *Biomacromolecules*, 10, 1244−1252.

[99] Srinivasachari, S., Liu, Y. M., Prevette, L. E., Reineke, T. M. (2007). Effects of trehalose click polymer length on pDNA complex stability and delivery efficacy. *Biomaterials*, 28, 2885−2898.

[100] Ren, Y., Jiang, X. A., Pan, D., Mao, H. Q. (2010). Charge density and molecular weight of polyphosphoramidate gene carrier are key parameters influencing its DNA compaction ability and transfection efficiency. *Biomacromolecules*, 11, 3432−3439.

[101] Morimoto, K., Nishikawa, M., Kawakami, S., Nakano, T., Hattori, Y., Fumoto, S., Yamashita, F., Hashida, M. (2003). Molecular weight-dependent gene transfection activity of unmodified and galactosylated polyethyleneimine on hepatoma cells and mouse liver. *Mol. Ther*., 7, 254−261.

[102] Matyjaszewski, K., Xia, J. H. (2001). Atom transfer radical polymerization. *Chem. Rev*., 101, 2921−2990.

[103] Heath, W. H., Senyurt, A. F., Layman, J., Long, T. E. (2007). Charged Polymers via controlled radical polymerization and their implications for gene delivery *Macromol. Chem. Phys*., 208, 1243−1249.

[104] Tang, R. P., Palumbo, R. N., Nagarajan, L., Krogstad, E., Wang C. (2010). Well-defined block copolymers for gene delivery to dendritic cells: probing the effect of polycation chain-length. *J. Controlled Release*, 142, 229−237

[105] Dash, P. R., Read, M. L., Barrett, L. B., Wolfert, M., Seymour, L. W. (1999). Factors affecting blood clearance and in vivo distribution of polyelectrolyte complexes for gene delivery. *Gene Ther.*, 6, 643−650.

[106] Liu, Z., Zhang, Z., Zhou, C., Jiao, Y.. (2010). Hydrophobic modifications of cationic polymers for gene delivery. *Prog. Pol. Sci*. 35, 1144-1162.

[107] Piest, M., Lin, C., Mateos-Timoneda, M.A., Lok, M.C., Hennink, W.E., Feijen, Engbersen, J.F. (2008). Novel poly(amido amine)s with bioreducible disulfide linkages in their diamino-units: structure effects and in vitro gene transfer properties. *J. Control. Release*. 130, 38-45.

[108] Anderson, B.K., Sizovs, A., Cortex, M., Waldron, C., Haddleton, D.M., Reineke, T.M. (2012). Effects of trehalose polycation end-group functionalization on plasmid DNA uptake and transfection. *Biomacromolecules.* 3-32.

[109] Eltoukhy, A. A., Siegwart, D. J., Alabi, C. A., Rajan, J. S., Langer, R., Anderson, D. G. (2012). Effect of molecular weight of amine end-modified poly(beta-amino ester)s on gene delivery efficiency and toxicity. *Biomaterials*, 33 (13), 3594−3603.

[110] Ji, W., Panus, D., Wang, W. (2011). Poly(2-aminoethyl methacrylate) with well-defined chain length for DNA vaccine delivery to dendritic cells. *Biomacromolecules*. 12. 4373-4385.

[111] Lucas, B., Remaut, K., Sanders, N.N., Braeckmans, K., De Smedt, S.C., Demeester, J. (2005). Studying the intracellular dissociation of polymer-oligonucleotide complexes by dual color fluorescence fluctuation spectroscopy and confocal imaging. *Biochemistry*. 44, 9905-9912.

[112] Thibault, M., Nimesh, S., Lavertu, M., Buschmann, M.D. (2010). Intracellular trafficking and decondensation kinetics of chitosan-pDNA polyplexes. *Mol. Ther.* 18, 1787-1795.

[113] Jones, R.A., Poniris, M.H., Wilson, M.R. (2004). pDMAEMA is internalised by endocytosis but does not physically disrupt endosomes. *J. Control. Release*. 96, 379-391.

[114] Matsumoto, Y., Itaka, K., Yamasoba, T., Kataoka, K.. (2009). Intranuclear fluorescence resonance energy transfer analysis of plasmid DNA decondensation from nonviral gene carriers. *J. Gene Med*. 11, 615-623.

[115] Richardson, S.C., Wallom, K.L., Ferguson, E.L., Deacon, S.P., Davies, M.W., Powell, A.J., Piper, R.C., Duncan, R. (2008). The use of fluorescence microscopy to define polymer localisation to the late endocytic compartments in cells that are targets for drug delivery. *J. Control. Release.* 127, 1-11.

[116] Denis-Mize, K.S., Dupuis, M., MacKichan, M.L., Singh, M., Doe, B., O'Hagan, D., Ulmer, J.B., Donnelly, J.J., McDonald, D.M., Ott, G. (2000). Plasmid DNA adsorbed onto cationic microparticles mediates target gene expression and antigen presentation by dendritic cells. *Gene Ther.* 7, 2105-2112.

[117] Chen, H.H., Ho, Y.P., Jiang, X., Mao, H.Q., Wang, T.H, Leong, K.W. (2008). Quantitative comparison of intracellular unpacking kinetics of polyplexes by a model constructed from quantum dot-FRET. *Molecular Therapy*. 16, 324-332.

[118] Luhmann, T., Rimann, M., Bittermann, A.G., Hall, H. (2008). Cellular uptake and intracellular pathways of PLL-g-PEG-DNA nanoparticles. *Bioconjug. Chem*. 19, 1907-1916.

[119] Kuroda, K.,. DeGrado, W.F. (2005). Amphiphilic polymethacrylate derivatives as antimicrobial agents. *J. Am. Chem. Soc*. 127, 4128-4129.

[120] Deng, Z. C., Bouchekif, H., Babooram, K., Housni, A., Choytun, N., Narain, R., (2008). Facile synthesis of controlled-structure primary amine-based methacrylamide polymers via the reversible addition-fragmentation chain transfer process. *Journal of Polymer Science Part a-Polymer Chemistry*, 46, (15), 4984-4996.

[121] Incani, V., Lavasanifar, A., Uludag, H. (2010). Lipid and hydrophobic modification of cationic carriers on route to superior gene vectors. *Soft Matter*. 6, 2124-2138.

[122] Manolova, V., Flace, A., Bauer, M., Schwartz, K., Saudan, P., Bachmann, M.F. (2008). Nanoparticle target distinct dendritic cell populations according to their size, *Eur. J. Immunol.* 38, 1404-1413.

[123] Farrell, L.L., Pepin, J., Kucharski, C., Lin, X., Xu, Z., Uludag, H. (2007). A comparison of the effectiveness of cationic polymers poly-L-lysine (PLL) and polyethylenimine (PEI) for non-viral delivery of plasmid DNA to bone marrow stromal cells (BMSC). *Eur. J. Pharm.* Biopharm. 65, 388-397.

[124] Mann, A., Thakur, G., Shukla, V., Signh, A.K., Khanduri, R., Naik, R., Jiang, Y., Kalra, N., Dwarakanath, B.S., Langel, U., Ganguli, M. (2011). Differences in DNA condensation and release by lysine and arginine homopeptides govern their DNA delivery efficiencies. *Mol. Pharmaceutics*, 8, 1729-1741.

[125] Prevette, L.E., Lynch, M.L., Reineke, T.M. (2010). Amide spacing influences pDNA binding of poly(amidoamine)s. *Biomacromolecules*. 11, 326-332.

[126] Wang, C., Deng, J., Zhao, Y., Zeng, X., Han, L., Pan, S., Wu, C. (2010). Poly(α-glutamic acid) combined with polycation as serum-resistant carriers for gene delivery. *International Journal of Pharmaceutics*. 398, 237-245.

[127] Jaganathan, H., Kinsella, J.M., Ivanisevic, A. (2008). Circular dichroism study of the mechanism of formation of DNA templated nanowires. *Chemphyschem*. 9, 2203-2206.

[128] Tseng, W.C., Haselton, F.R., Giorgio, T.D. (1997). Transfection by cationic liposomes using simultaneous single cell measurements of plasmid delivery and transgene expression. *J. Biol. Chem.* 272, 25641-25647.

[129] van der Aa, M.A., Huth, U.S., Hafele, S.Y., Schubert, R., Oosting, R.S., Mastrobattista, E., Hennink, W.E., Peschka-Suss, R., Koning, G.A., Crommelin, D.J. (2007). Cellular uptake of cationic polymer-DNA complexes via caveolae plays a pivotal role in gene transfection in COS-7 cells. *Pharm. Res*. 24,1590-1598.

[130] Lee, H., Jeong, J.H., Park, T.G. (2002). PEG grafted polylysine with fusogenic peptide for gene delivery: high transfection efficiency with low cytotoxicity. *J. Control. Release*. 79, 283-291.

[131] Cohen, R.N., van der Aa, M.A., Macaraeg, N., Lee, A.P., Szoka, F.C. (2009). Quantification of plasmid DNA copies in the nucleus after lipoplex and polyplex transfection. *J. Control. Release*. 135, 166-174.

[132] Cho, Y.W., Kim, J.D., Park, K. (2003). Polycation gene delivery systems: escape from endosomes to cytosol. *J. Pharm. Pharmacol*. 55, 721-734.

[133] Murthy, N., Robichaud, J.R., Tirrell, D.A., Stayton, P.S., Hoffman, A.S. (1999). The design and synthesis of polymers for eukaryotic membrane disruption. *J. Control. Release*. 61, 137-143.

[134] von Gersdorff, K., Sanders, N.N., Vandenbroucke, R., De Smedt, S.C., Wagner, E., Ogris, M. (2006). The internalization route resulting in successful gene expression depends on both cell line and polyethylenimine polyplex type. *Mol. Ther.* 14, 745-753.

[135] Rejman, J., Bragonzi, A., Conese, M. (2005). Role of clathrin- and caveolae-mediated endocytosis in gene transfer mediated by lipo- and polyplexes. *Mol. Ther*. 12, 468-474.

[136] Rejman, J., Conese, M., Hoekstra, D. (2006). Gene transfer by means of lipo- and polyplexes: role of clathrin and caveolae-mediated endocytosis. *J. Liposome Res.* 16, 237-247.

[137] Gabrielson, N.P., Pack, D.W. (2009). Efficient polyethylenimine-mediated gene delivery proceeds via a caveolar pathway in HeLa cells. *J. Control. Release*. 136, 54-61.

[138] Hufnagel, H., Hakim, P., Lima, A., Hollfelder, F. (2009). Fluid phase endocytosis contributes to transfection of DNA by PEI-25. *Mol. Ther*. 17, 1411-1417.

[139] Kiss, A.L., Botos, E. (2009). Endocytosis via caveolae: alternative pathway with distinct cellular compartments to avoid lysosomal degradation? *J. Cell. Mol. Med*. 13, 1228-1237.

[140] Ziello, J.E., Huang, Y., Jovin, I.S. (2010). Cellular endocytosis and gene delivery. *Mol. Med*. 16, 222-229.

[141] Mayor, S., Pagano, R.E. (2007). Pathways of clathrin-independent endocytosis. *Nat. Rev. Mol. Cell Biol.* 8, 603-612.

[142] Orlandi, P.A., Fishman, P.H. (1998). Filipin-dependent inhibition of cholera toxin: evidence for toxin internalization and activation through caveolae-like domains. *J. Cell Biol*. 141, 905-915.

[143] Lam, J.K., Armes, S.P., Stolnik, S. (2011). The involvement of microtubules and actin filaments in the intracellular transport of non-viral gene delivery system. *J. Drug Target*. 19, 56-66.

[144] Parton, R.G., Simons, K. (2007). The multiple faces of caveolae. *Nat. Rev. Mol. Cell Biol.* 8, 185-194.

[145] Hsu, C., Uludag, H. (2012). Cellular uptake pathways of lipid-modified cationic polymers in gene delivery to primary cells. *Biomaterials*. 33, 7834-7848.

[146] Orgis, M., Steinlein, P., Carotta, S., Brunner, S., Wagner, E. (2001). DNA/polyethylenimine transfection particles influence of ligans, polymer size, and PEGylation on internalization and gene expression. *AAPS Pharm Sci*. 3, E21.

[147] Sharma, G., Valenta, D.T., Altman, Y., Harvey, S., Xie, H., Mitragotri, S., Smith, J.W. (2010). Polymer particle shape independently influences binding and internalization by macrophages. *J. Control. Release*. 147, 408-412.

[148] Shen, Z., Reznikoff, G., Dranoff, G., Rock, K.L. (1997). Cloned dendritic cell can present exogenous antigens on both MHC class I and class II molecules. *J. Immunol*. 158, 2723-2730.

[149] Intra, J., Salem, A. (2008). Characterization oft he transgene expression generated by branched and linear polyethylenimine-plasmid DNA nanoparticles in vitro and after intraperitoneal injection in vivo. *J. Controlled Release*. 130 (2) 129-138.

[150] Sen, D., Deerink, T., Ellsman, M., Parker, I., Cahalan, M. (2008). Quantum dots for tracking dendritic cells and priming an immune response in vitro and in vivo. *PLOS One*, 3,9,1.

[151] Tseng, W.C., Haselton, F.R., Giorgio, T.D. (1997). Transfection by cationic liposomes using simultaneous single cell measurements of plasmid delivery and transgene expression. *J. Biol. Chem.* 272, 25641-25647.

[152] Zhu, J., Zhao, L., Zhao, X., Chen, Z. (2007). Lycium barbarum polysaccharides regulate phenotypic and functional maturation of murine dendritic cells. *Cell Bio. Inter*. 31, 615-619.

[153] Sun, X., Chen, S., Han, J., Zhang, Z. (2012). Mannosylated biodegradable polyethyleneimine for targeted DNA delivery to dendritic cells. *Inter. J. Nanomed*. 7, 2929-2942.

[154] Jin, P., Han, T.H., Ren, J., Saunders, S., Wang, E., Marincola, F.M., Stroncek, D.F. (2010). Molecular signatures of maturing dendritic cells: implications for testing the quality of dendritic cell therapies. *J. Trans. Med*. 8.

[155] Dearman, R.J., Cumberbatch, M., Maxwell, G., Basketter, D.A., Kimber, I. (2008). Toll-like receptor ligand activation of murine bone marrow-derived dendritic cells. *Immunology*. 126, 475-484.

[156] Salazar, L., Aravena, O., Contreras-Levicoy, J., Pesce, B., Catalan, D., Zuniga, R., Iruretagoyena, M., Kalergis, A. M., Aguillon, J.C. (2007). Short-term lipopolysaccharide stimulation induces differentiation of murine bone marrow-derived dendritic cells into a tolergenic phenotype. *Eur. Cytokine Netw*. 18, 78-85.

[157] Rupei, T., Ji, W., Panus, D., Palumbo, R.N., Wang, C. (2011). Block copolymer micelles with acid-labile ortho ester side-chains: Synthesis, characterization, and enhanced drug delivery to human glioma cells. *J. Contr. Rel*.; 151, 18-27.

[158] Hoskin, D.W., Ramamoorthy, A. (2007). Studies on anticancer activities of antimicrobial peptides. *Biochimica et Biophysica Acta*, 1778, 357-375.

[159] Huan, M., Zhang, B., Teng, Z., Cui, H., Wang, J., Liu, X., Xia, H., Zhou, S., Mei, Q. (2012). In vitro and in vivo antitumor activity of a novel pH-activated polymeric drug delivery system for doxorubicin. *PLoS One*; 7, 9.

[160] Sethuraman, V.A., Lee, M.C., Bae, Y.H. (2008). A biodegradable pH-sensitive micelle system for targeting acidic solid tumors. *Pharm. Res.* 25(3) 657-666.

[161] Ahmed, F., Pakunlu, R.I., Brannan, A., Bates, F., Minko, T., Discher, D.E. (2006). Biodegradable polymersomes loaded with both paclitaxel and doxorubicin permeate and shrink tumors, inducing apoptosis in proportion to accumulated drug. *J Control Release* 116(2) 150-158.

[162] Mikhail, A.S., Allen, C. (2009). Block copolymer micelles for delivery of cancer therapy: Transport at the whole body, tissue and cellular levels. *J. Contr. Rel*.; 138, 214-223.

[163] Gaucher, G. (2005). Block copolymer micelles: preparation characterization and application in drug delivery. *J. Controlled Release*, 109 (1−3), 169−188.

[164] Riedl, S., Zweytick, D., Lohner, K. (2011). Membrane-active host defense peptides--challenges and perspectives for the development of novel anticancer drugs. *Chem Phys Lipids* 164(8) 766-781.

[165] Kenawy, E.R., Worley, S.D., Broughton, R. (2007). The chemistry and applications of antimicrobial polymers: A state-of-the-art review. *Biomacromolecules*; 8, 5, 1359-1384.

[166] Friedrich, J., Seidel, C., Ebner, R., Kunz-Schughart, L.A. (2008). Spheroid-based drug screen: considerations and pratical approach. *Nature-Protocol.* 4, 3, 309-324.

[167] Abe, T., Hasegawa, S., Taniguchi K., Yokomizo, A., Kuwano, T., Ono, M., Mori, T., Hori, S., Kohno, K., Kuwano, M. (1994). Possible involvement of multidrug-resistance-associated protein (MRP) gene expression in spontaenous drug resistance to vincristin, etoposide and adriamycin in human glioma cells. *Int. J. Cancer*; 58, 860-864.

[168] Lee, E.S., Na, K., Bae, Y.H. (2005). Doxorubicin loaded pH-sensitive polymeric micelles for reversal of resistant MCF-7 tumor. *J. Cont. Rel.*; 103, 405-418.

[169] Mohajer, G., Lee, E.S., Bae, Y.H. (2007). Enhanced intercellular retention activity of novel pH-sensitive polymeric micelles in wild and multidrug resistant MCF-7 cells. *Pharm. Res.*; 24, 9, 1618-1627.

[170] Tahara, K., Kato, Y., Yamamoto, H., Kreuter, J., Kawashima, Y. (2011). Intracellular drug delivery using polysorbate 80-modified poly(D,L-lactide-co-glycolide) nanospheres to glioblastoma cells. *J. of Microencapsulation*; 28, 1, 29-36.

[171] Hussein Al Ali, S. H., Al-Qubaisi, M., Hussein, M.Z., Ismail, M., Bullo, S. (2013). Hippuric acid nanocomposite enhances doxorubicin and oxalipatin-induced cytotoxicity in MDA-MB231, MCF-7 and Caco2 cell lines. *Drug Design, Development and Therapy*. 7; 25-31.

[172] Shain, K.H., Dalton, W.S. (2001). Cell adhesion is a key determinant in de Novo multidrug resistance (MDR): New targets for the prevention of acquired MDR. *Mol Cancer Ther*; 1, 69-78.

[173] Sun, W., Rajagopalan, R., Lim, C.T. (2011). Development of three-dimensional tumor models for the study of anti-cancer drug effects. *Mechanobiology of cell-cell and cell-matrix ineractions*. 151.

[174] Padamalayam, I., Suto, M.J. (2012). 3D cell cultures: Mimicking in vivo tissues for improved predictability in drug discovery. *Annual Reports in Medicinal Chemistry*, 47, 367-378.

[175] Tredan, O., Galmarini, C.M., Patel, K., Tannock, I.F. (2007). Drug resistance and the solid tumor microenvironment. *J Natl Cancer Inst*; 99: 1441-1454.

[176] Huang, K., Ma, H., Liu, J., Huo, S., Kumar, A., Wei, T., Zhang, X., Jin, S., Gan, Y., Wang, P.C., He, S., Zhang, X., Liang, X.J. (2012). Size-dependent localization and penetration of

ultrasmall godl nanoparticles in cancer cells, multicellular spheroids, and tumors in vivo. *ACS Nano*.; 6, 5, 4483-4493.

[177] Minchinton, A.I., Tannock, I.A. (2006). Drug penetration in solid tumours. *Nature Revies: Cancer*; 6, 583-592.

[178] Kim, T.H., Mount, C.W., Gombotz, W.R., Pun, S.H. (2010). The delivery of doxorubicin to 3-D multicellular spheroids and tumors in a murine xenograft model using tumor-penetrating triblock polymeric micells. *Biomaterials*, 31, 7386-7397.

[179] Tang, L., Gabrielson, N.P., Uckun, F.M., Fan, T.M., Cheng, J. (2013). Size-dependent tumor penetration and in vivo efficacy of monodisperse drug-silica nanoconjugates. *Mol. Pharmaceutics*, 10, 883-892.

[180] Li, Y., Wang, J., Wientjes, M.G., Au, J.L.S. (2012). Delivery of nanomedicines to extracellular and intracellular compartments of a solid tumor. *Advanced Drug Delivery Reviews*. 64; 29-39.

[181] Ma, J., Chen, C.S., Blute, T., Waxman, D.J. (2011). Anti-angiogenesis enhances intratumoral drug retention. *Cancer Res*.; 71, 7, 2675-2685.

[182] Costache, A.D., Sheihet, L., Zaveri, K., Knight, D.D., Kohn, J. (2009). Polymer-drug interaction in tyrosine-derived triblock copolymer nanospheres: a computional modeling approach. *Mol. Pharm*. 6, 5, 1620-1627.

[183] Brown, J.M., Wilson, W.R. (2004). Exploiting tumour hypoxia in cancer treatment. *Nature Reviews: Cancer*; 4, 437-447.

[184] Duan, Q., Liu, Y., Booth, C.J., Rockwell, S. (2012). Use of fenbendazole-containing therapeutic diets for mice in experimental cancer therapy studies. *J. Amer. Assoc. Lab. Animal Science*. 51, 2, 224-230.

[185] Poste, G., Doll, J., Hart, I.R., Fidler, I.J. (1980). In vitro selection of murine B16 melanoma variants with enhanced tissue-invasive properties. *Cancer Res.,* 40, 5, 1636-44.